UNIVERSITÀ degli STUDI di CATANIA | DIPARTIMENTO di FISICA e ASTRONOMIA

CORSO DI DOTTORATO IN FISICA

ANTONIO FIGURA

BINARY NEUTRON STAR MERGERS WITH MICROSCOPIC EOS

TESI DI DOTTORATO

TUTOR SCIENTIFICO:
DOTT.SSA G.F. BURGIO
TUTOR INTERNO:
PROF. VALERIO PIRRONELLO

XXXIII CICLO

ABSTRACT

With the beginning of the gravitational wave astronomy era, increasingly realistic simulations of Binary Neutron Star (BNS) mergers constitute a fundamental aspect in order to successfully investigate gravitational wave signals. The Equation of State (EOS) of stellar matter represents a fundamental input for such simulations: such EOS should accurately describe the wide range of temperatures and densities which are usually reached in merger events, with the requirement of fulfilling the currently known astrophysical and nuclear constraints.

In my research work, whose results are reported in this thesis and the papers I have published, I have studied BNS simulations using a set of state of the art microscopic EOSs, focusing on the investigation of both the hydrodinamic quantities and the gravitational wave signal related properties. A key aspect of the work has regarded the theoretical study of such EOSs, for which, together with my research group, I have investigated macroscopically related quantities and their involvement in "Universal Relations". Part of this work has been related to extending the EOSs I have employed in BNS simulations to Finite Temperature: indeed, very few public finite temperature EOSs are present, with the usual approach being represented by using zero temperature EOSs where finite temperature effects are included in simulations via an ideal fluid approximation. I have investigated the latter aspect through BNS simulations, with results reported in a specific paper.

Finally, part of this thesis discusses a Numerical Relativity project which I carried out, in collaboration with the Relativistic Astrophysics group of the Goethe University (Frankfurt am Main), which has led to the creation of a new code, of which I am the main author and maintainer, that solves the spacetime equations in the fCCZ4 formulation, for arbitrary curvilinear coordinate systems.

DEDICATION

This thesis work is dedicated to my family and many friends who supported and encouraged me during these years.

ACKNOWLEDGMENTS

First and foremost, I want to thank my supervisor, Dr. Burgio, and our main collaborator, Dr. Hans-Josef Schulze, who accepted me as a member of their group and guided me during the years of my PhD. I am grateful not only for the possibilities related to my professional growth, but also for the many opportunities related to both spending part of my PhD abroad and my participations in schools and workshops.

In this regard, I am particularly thankful to Prof. Luciano Rezzolla, who accepted me in his RelAstro group at the Goethe University; the discussions I have had with him and the group members have been extremely important to me and have made a major part of this thesis work possible. I am also thankful for all the resources I have been given access to, including the Goethe and SuperMUC clusters I have actively used.

I take this chance to thank all the colleagues and PhD students I have known during these years and with whom I have often collaborated. In particular, I thank my friend and colleague Jinbiao Wei for all the interesting and useful discussions we have had.

Finally, I wish to thank the University of Catania and INFN for the support which both made my travels and stays possible, but also allowed me to access the computational resources provided by the CINECA's Marconi supercomputer.

Table of Contents

LIST OF FIGURES

LIST OF TABLES

CHAPTER 1

INTRODUCTION

In the past few years, the LIGO-Virgo collaboration has achieved extremely brilliant milestones, marking the beginning of the gravitational wave astronomy era; among all the successful observations, the GW170817 event [1] occupies an important place. Indeed, not only it has represented the first joint detection, involving both the LIGO and Virgo detectors, of gravitational waves emitted by the merger of a Binary Neutron Star (BNS) system but it was also characterized by the detection of its related electromagnetic emission, labeled as GRB 170817A [2] (referring to the gamma emission from the short gamma-ray burst) and AT2017gfo (labelling instead the kilonova counterpart).

Most importantly, the observation has provided new knowledge on the still unknown Equation of State (EOS) ruling matter at the very high densities reached in neutron stars.

In order to correctly interpret the detected signal, whose profile heavily depends on the physical characteristics of the source (in the case of BNS mergers, total mass, EOS, spins etc.), experimental data have to be filtered using a set of signals, the so-called *template bank* of waveforms, theoretically determined considering plausible parameters for the merging objects [3].

As the gravitational wave signal of merging binary systems can't be calculated exactly

(there is no known exact solution of the Einstein field equations for such a regime), currently, the only viable possibility is to calculate it is via approximations or numerical methods. While the part of the signal corresponding to the inspiral phase can be computed in the context of analytical techniques, such as the successful Effective One Body (EOB) model [4], Numerical Relativity (NR) simulations represent the only applicable tool in order to study the merger and post-merger phases, being gravity strongest and general relativistic effects cannot be approximated. In addition to be performed in full General Relativity (GR), such simulations employ state of the art computational techniques and appropriate formulations of the Einstein field equations (such as the advanced CCZ4 [5]) and can also be used in order to calibrate EOB models [6].

As anticipated before, the construction of initial data which are later evolved in time is an important step, since they should be as realistic as possible. Focusing on BNS mergers, a primary ingredient is represented by the EOS used in order to model the two compact objects: indeed, the considered candidate should fulfill a number of constraints, which are of nuclear and astrophysical nature (see e.g. Ref. [7] and references therein), and should be compatible with the GW170817 event (see Ref. [8] for a recent review of the constraints imposed from the event). Currently available choices range from simple polytropic (or piecewise polytropic) EOSs to tabulated ones, which can be, in turn, characterized by either zero-temperature or finite-temperature (a first description of the different choices is given in Sec. 2.5.2).

Improving the current status of numerical simulations represents a very active field of research; possible research directions are related, e.g., to the implementation of magnetic fields in both ideal and resistive MHD [9, 10], the development of new frameworks for simulations [11–13], the implementation of a richer fenomenology through both a greater variety of initial data for simulations [14, 15] and new EOSs fulfilling all the current constraints [16–22].

This thesis work focuses in particular on the investigation of realistic microscopic EOSs and their first implementation in numerical codes in order to simulate binary neutron star

mergers, in order to study the related hydrodynamic properties and gravitational wave features. Results presented in this thesis work are related to the study of such a set of EOSs in order to first investigate their features; the EOSs are then converted into a form compatible with NR codes and employed in order to model and evolve equal-mass BNS.

Part of this work is also related to the development of new NR codes and techniques: in this context, I have developed a new code which solves the Einstein equations in the very recent fCCZ4 [11] formulation for arbitrary coordinate systems. The importance of such a work lies in the fact that most NR codes do currently use cartesian coordinates, which feature many desirable properties but are not suitable to exploit symmetries of often-simulated spherical-like objects (e.g. a single black hole or NS at the origin of the coordinate system, such as in the post-merger phase of NR simulations); spherical (or spherical-like, as described later in this work) coordinates are useful in this regard, and can decrease the computational resources needed to perform simulations of a not-negligible factor.

The thesis is organized as follows: Chapters 1 and 2 feature an introduction on the work and the simulation of NSs; their internal structure and the EOS problem are briefly discussed, together with gravitational wave theory. The methods and the formulations adopted in this work for both solving the Einstein and hydrodynamic equations are also discussed in Ch. 2.

In Chapter 3, the set of microscopic EOSs is presented and their global properties are discussed. The chapter includes results published in Ref. [23] and is mainly devoted to investigate the same set of EOSs in the light of universal relations between the moment of inertia, tidal deformability and spin-induced quadrupole moment.

The extension of the microscopic EOSs to finite temperature is discussed in Chapter 4; in this regard, all the results presented are published in Ref. [21].

Chapter 5 focuses on the implementation of the EOSs in numerical codes. In particular, for a restricted number of EOSs, a comparison is carried out between the usually adopted *hybrid EOS* approach and the fully consistent temperature treatment, focusing on the determination of an optimal adiabatic index $\Gamma_{\rm th}$ to be used in simulations; these results are

published in Ref. [24].

The entire set of finite temperature microscopic EOSs is discussed in Chapter 6, where a systematic study of the gravitational wave and hydrodynamic properties is included. At the time of writing this report, a paper focusing on the discussion of these results is in preparation.

Chapter 7 is devoted to the presentation of my code, where every aspect (from the numerical methods adopted to the results of the tests carried out) is discussed. At the time of writing, these results are unpublished.

Finally, Chapter 8 includes the main conclusions and summarizes the results of this thesis.

In summary, part of the contents of this thesis work has appeared in the following papers:

- *Neutron star universal relations with microscopic equations of state* [23]

J.-B. Wei, AF, G. F. Burgio, H. Chen, and H.-J. Schulze, Journal of Physics G Nuclear Physics **46**, 034001 (2019).

- *Hot neutron stars with microscopic equations of state* [21]

J.-J. Lu, Z.-H. Li, G. F. Burgio, AF, and H. J. Schulze, Physical Review C **100**, 054335 (2019).

- *Hybrid equation of state approach in binary neutron-star merger simulations* [24]

AF, J.-J. Lu, G. F. Burgio, Z.-H. Li, and H.-J. Schulze, Phys. Rev. D 102, 043006 (2020).

Results included in Chapter 6 will be included in the following paper:

- *Binary neutron star merger simulations with hot microscopic equations of state*

AF, J.-J. Lu, L. Fan., G. F. Burgio, Z.-H. Li, and H.-J. Schulze, in preparation.

CHAPTER 2

NEUTRON STARS

2.1 Introduction

The theoretical prediction of a neutron star dates to 1934 and was made by W. Baade and F. Zwicky, who wrote, in particular, "*With all reserve we advance the view that supernovae represent the transitions from ordinary stars to neutron stars, which in their final stages consist of extremely closely packed neutrons*" [25]. Today, we know that a neutron star represents a possible result at the very end of the stellar evolution of a massive star ($M > 8\ M_\odot$, where $M_\odot$ represents the solar mass, $M_\odot \approx 1.989 \times 10^{33}$ g); indeed, after such a star has undergone a supernova explosion, a possible remnant (the other being a black hole) is represented by a hot ($T \approx 10^{11}$ K [26], corresponding to approximately 9 MeV) neutron rich object, the result of the collapse of the iron core of the progenitor star [27]. Such an object represents one of the densest known forms of matter [28], with central densities of order 10^{15} g/cm^3, and is also classified, together with white dwarfs and black holes, as a *compact object*, due to the high compactness, parameter determined by the M/R (mass over radius) ratio of the object. Neutron stars, indeed, have very small radii, with $R \sim 12$ km, and masses above the solar mass, tipically $M \sim 1.5 M_\odot$ (see [29] for a recent review).

In order to study the equilibrium configuration for such an object, in the simplest case of spherical symmetry and no rotation, the equations governing matter are the so-called Tolman-Oppenheimer-Volkoff (TOV) equations:

$$\frac{dp}{dr} = -\frac{(p+e)(m+4\pi r^3 e)}{r(r-2m)}\,, \tag{2.1}$$

$$\frac{dm(r)}{dr} = 4\pi r^2 e\,, \tag{2.2}$$

where p, e and m respectively represent the pressure, energy density and mass as functions of the radial coordinate r. This set of equations is then closed by an EOS, i.e. a relation between thermodynamic quantities of the kind $p = p(e)$. In order to solve such a system of equations, one needs to specify appropriate boundary conditions, i.e. the central density ρ_c and pressure p_c and integrate with respect to r until the surface, characterized by $r = R$ and $p(R) = 0$, is reached. The solution of the TOV equations then allows to determine macroscopical quantities such as the gravitational mass M and the radius R of the star. Such an analysis also allows the determination of the maximum mass $M_{\rm TOV}$ supported by a stable non-rotating star (*TOV limit*); the latter is a very important quantity, which can be used to constrain the EOS. Indeed, a plausible EOS should allow for a $M_{\rm TOV}$ that has to be greater than the current astrophysical constraints on the NS mass [30–32].

Such a simple picture is complicated when taking into account both rotational properties and magnetic fields. As a matter of fact, when a neutron star forms as a result of a collapse, it conserves the angular momentum and the magnetic flux of the progenitor star; tipically, spin periods range from few ms to several s, while magnetic fields are of the order of $10^8 - 10^{12}$ G and are thought to reach more than 10^{14} G in "Magnetars" [33], neutron stars with the highest magnetic field.

It is, indeed, thanks to the dipolar magnetic field, whose axis is in general misaligned with respect to the rotation axis, that, starting with the very first observation in 1967 [34], it has been possible to observe neutron stars as "Pulsars" from Earth. Indeed, a beam of radio waves is continuously emitted along the magnetic axis and if the beam sweeps through

the direction of Earth, such pulses, whose period is the rotational period of the star, can be detected.

This thesis work focuses in particular on *Binary Neutron Stars* (BNSs), i.e. star systems consisting of two neutron stars, orbiting around their common center of mass. After the first observation of such a system in 1974 by R. Hulse and J. Taylor [35] many others have followed (see Ref. [36] for a recent review). While the formation processes are not completely understood, the generally accepted scenario consists of two progenitor main-sequence stars having a mass exceeding 8 $M_\odot$ (but still lower than approximately $25M_\odot$). After the supernova explosion of the more massive star, the newly created neutron star continues to orbit within the system, which is now characterized by the presence of a common envelope, consisting of the outer layers of the less massive star [37]. Eventually, the latter will also undergo a supernova explosion and a BNS system forms only if the binary system is still bound.

The importance of these systems lies in the fact that, together with binary black hole systems, they represent perfect sources of gravitational waves. Indeed, as first confirmed for the Hulse-Taylor BNS [38], the orbits of the two objects shrink in time, due to the energy loss related to the continuously emitted gravitational radiation. The very final phases of such process (which is also called *Inspiral*, see Sec. 2.5 for details) are characterized by the strongest emission of gravitational radiation and lead to the two stars merging together into a single object; indeed, these final phases have already been observed by the LIGO-Virgo detectors [1, 39]. In addition to information provided by the gravitational wave signal, BNS mergers are also sources of electromagnetic radiation in a wide range of bands. Indeed, the GW170817 event has already shown that a multimessenger observation has the capability to provide to further enrich the picture: the first short Gamma Ray Burst (sGRB) was detected by the *Fermi* and *Integral* satellites [40], together with the first kilonova, a transient event, lasting days to weeks, powered by the radioactive decay of heavy neutron-rich elements synthesized in the merger ejecta [41].

2.2 The internal structure

Being one of the main ingredients describing the structure of neutron stars, the equation of state (EOS) is still unknown and represents a great challenge in the investigation of these objects, especially because of the wide range of densities, temperatures and electron fractions they manifest. For cold neutron stars (with a temperature below 1 MeV), the problem becomes simpler since both the zero-temperature approximation and the beta-equilibrium conditions can be adopted, so that the rest-mass density ρ, or, analogously, the baryon number density n_{B} remains the only variable; such conditions, however, are not true in cases such as BNS mergers or core collapse supernovae; in the latter cases, an ideal EOS should cover the ranges $10^{-11} < n_{\mathrm{B}} <$ few fm^{-3}, $0 < T < 150$ MeV, and $0 < Y_{\mathrm{e}} < 0.6$ [42, 43].

Before entering into a detailed discussion about the EOS, it is important to outline the fundamental properties related to the structure of a (cold) neutron star, which a realistic EOS should be able to reproduce. For $\rho < 10^4$ g/cm^3, a thin *atmosphere* composed by partially ionized atoms and electrons envelops the star. The region which follows at higher densities, the *crust*, is characterized by the presence of heavy nuclei [26]; in particular, the outermost layer of such region contains ^{56}Fe ions immersed in a sea of electrons. With increasing density, more massive and neutron rich nuclei, e.g. ^{62}Ni, ^{64}Ni, ^{66}Ni, ^{86}Kr, ^{84}Se, ^{82}Ge [44], are found. Despite the fact that the crust mass constitutes only a few percent of the total NS mass, and its thickness is typically less than 1/10 of the star radius, the role of this part of the star is very important for many reasons: it separates the core part from the photosphere, where X-ray radiation is emitted, and its properties are crucial in order to understand the relation between the detected X-ray flux and the temperature of the NS core [26].

The crust is generally divided into an outer crust, where a population of completely ionized nuclei and a sea of electrons are present, and an inner crust, where also unbound neutrons are present. Interestingly, nuclei are arranged in a body-centered cubic lattice (see,

e.g., Ref. [45] and references therein) with more and more neutron rich ions appearing with increasing density. At a rest-mass density $\rho \approx 4 \times 10^{11}$ g/cm^3 the "neutron drip" density is reached, where neutrons start to drip out of nuclei as the neutron chemical potential becomes too high for them to bind additional neutrons; these unbound neutrons form a superfluid component and are then free to move and can propagate through the lattice [46, 47]. The structure of matter for this region is investigated with the well established solid state physics methods, even if the physical conditions are extreme and far from terrestrial ones [48].

With increasing density, the average distance between the nuclei in the lattice decreases, so that the nuclear interaction of an individual nucleus shows notable effects towards its neighbours; the main consequence is a strong deformation of the nuclear clusters, which can touch and determine a sequence of nuclear "pasta" [49, 50]. In particular, such structures appear at the bottom of the inner crust, at approximately $\rho_{\rm cm} \approx 10^{14}$ g/cm^3. Indeed, simulations (see e.g. Ref. [51] for a recent example) also show that the shapes the clusters can assume greatly change, resembling typical pasta shapes: a first phase, the "spaghetti" phase, where nuclear structures become rod-like, is followed by a "lasagna" phase, where slabs become the preferred shapes, which is in turn followed by an "anti-spaghetti" phase, with rod-like bubbles, and a final "Swiss cheese" phase, where neutrons and protons gather in spherical bubbles [52].

The end of this transition phase, occurring at a density $\rho_0/2$, where $\rho_0 \approx 2.8 \times 10^{14}$ g/cm^3 represents the density of saturated nuclear matter, marks the beginning of the core region, which is also characterized by an outer and an inner region. In the outer core, in particular, nucleons determine a strongly interacting Fermi liquid, while leptons constitute an almost ideal Fermi gas. Therefore, variables in this region are represented by the number densities $n_{\rm j}$ with $j = n, p, e, \mu$ of neutrons, protons, electrons and muons respectively, which fulfill, at every fixed density, the following constraints of fixed baryon number density and charge neutrality:

$$n_{\rm n} + n_{\rm p} - n_{\rm B} = 0\,, \tag{2.3}$$

$$n_{\rm e} + n_{\mu} - n_{\rm p} = 0\,. \tag{2.4}$$

The study of the hydrodynamics of the core is important for understanding collective modes of matter [53], theories of spin-down and glitches [54] and stellar oscillations [55]. Microscopic calculations show that protons are expected to be superconducting, with a less clear situation for neutrons [56].

While for low-masses NSs (with central densities less than approximately $2-3\rho_0$) the outer core constitutes the entire core of the object, heavier NSs, whose central densities reach values up to several times ρ_0, manifest an inner core of several kilometers and densities in the range $\rho \geq 2\rho_0$ that occupies the central region of the star [57]. The composition of this region is not well known: a first possibility is related to the appearance of hyperons, since at densities of about $2-3\rho_0$ the hyperon threshold is expected to be crossed [58]. It has been shown within Brueckner-Bethe-Goldstone calculations [59] that the inclusion of hyperons lowers the NS maximum mass so that, in general, even the typically observed masses of $M \approx 1.4 M_{\odot}$ cannot be reached. This problem is also known in literature as the "hyperon puzzle" [60]. The appearance of quark matter in the core may represent a solution to this puzzle [61]; indeed, Quantum Chromodynamics predicts that, at sufficiently high energy densities, nuclear matter undergoes a phase transition leading to a matter composed of deconfined quarks and gluons [62]. Such quark-gluon plasma has been already produced in laboratory conditions with ultrarelativistic heavy-ion collisions [63], and the innermost regions of massive NSs could be such that the energy densities reached are comparable to those reached in heavy-ion collisions [28, 64]. The actual existence of quarks in the inner core of NSs, however, is still an open question.

2.3 The equation of state problem: an overview

As previously anticipated, in order to construct a static NS solution, the TOV system of Eqs. (2.1) and (2.2) needs to be closed by an EOS, which is representative of the microphysics

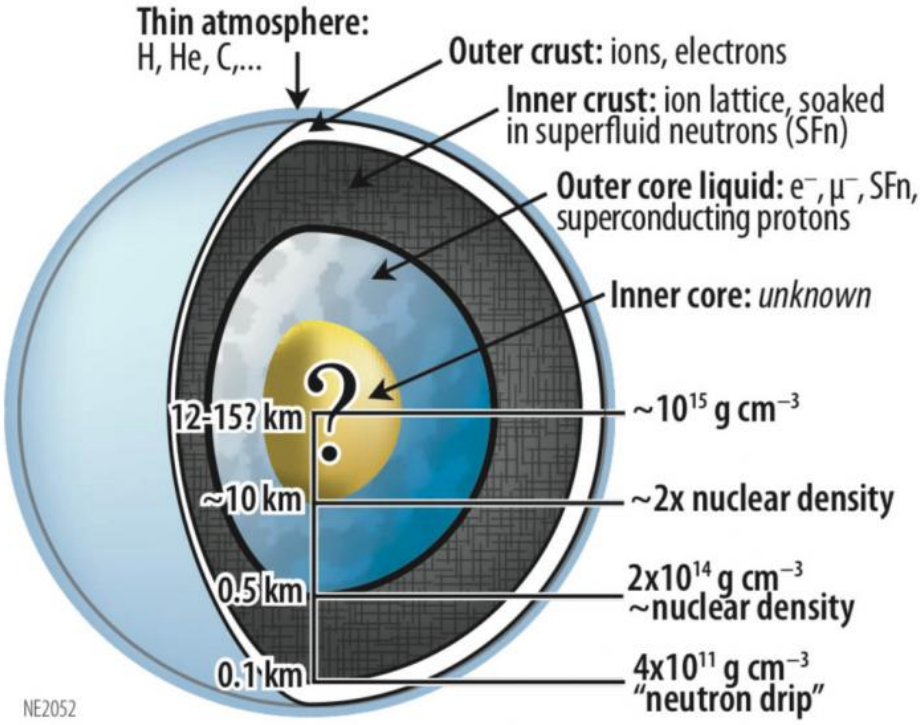

Figure 2.1 Internal structure of a neutron star; image from Ref. [65].

ruling the NS matter. This section will briefly outline the methods and possibilities adopted in the characterization of the EOSs; for a more complete treatment of this subject the reader should refer to specialized texts (see, e.g., Refs. [66–68]).

The simplest EOS is represented by an ideal neutron gas model where no interactions are present, which is essentially treated as a free Fermi gas. This was the idea which Oppenheimer and Volkoff originally investigated [69], and which lasted for almost 50 years; even if such a model is today considered unrealistic, it led to the comprehension of an important feature characterizing the NS EOS, i.e. the presence of a maximum gravitational mass for a non rotating NS, the so-called "TOV mass limit" (see, e.g., Ref. [70] for a detailed discussion), which is of about 0.7 $M_\odot$ for the case they investigated.

With the discovery of pulsars [34] and in particular of the first binary pulsar [35], which made it possible to determine the masses of the two components ($M_1 = 1.441 M_\odot$ and $M_2 = 1.387 M_\odot$), it became clear that a more realistic EOS was needed in order to explain

the measured masses, which exceeded the $0.7M_{\odot}$ limit. As a matter of fact, a real NS does not contain only neutron, but also consists of a small fraction of protons and electrons; also, the free Fermi gas model ignores nuclear interactions, which can't be neglected in realistic neutron star models. The next step with respect to the simple neutron gas model is to assume that the hadronic constituents of the NS matter are constituted by nucleons only; these stars are often referred to as "conventional neutron stars" [66], to distinguish them from stars in which an exotic core is present.

Two main alternatives are viable in order to describe the strong interaction between nucleons: the *microscopic approach* and the *phenomenological approach*. In the former case, the main input is given by the two-body nucleon-nucleon interaction, which is described by realistic models like the Argonne, Bonn, Nijmegen, Paris and Urbana potentials (see e.g. Refs. [66, 71] and references therein). The scheme relies on the meson exchange theory of nuclear forces, with nucleons, nuclear resonances and mesons being incorporated in a potential representation. The parameters appearing in the potential are consequently adjusted in order to reproduce the experimental data for the three-body problem, with the final step consisting in the solution of the many-body problem [72]. Important examples, representatives of this approach, are the APR [73], DBHF [74], VMC [75] and, most importantly in the context of this thesis work, the microscopic EOSs presented in Sec. 3.1 and included in Table 3.1.

The main input of a phenomenological approach is instead represented by a density dependent effective nuclear interaction. In this case, the parameters typical of the interaction are tuned in order to reproduce various properties of the nuclei and the saturation properties of nuclear matter. While this approach involves simpler calculations than the microscopic one, it is obviously less fundamental; also, since the behaviour of nuclear matter is closely related to properties of single particles (like the effective masses, chemical potentials etc.), which are poorly constrained by experimental data, a simple extrapolation to extreme conditions, such as at very high density, can be quite arbitrary [66]. Well known examples of

this approach, widely used in numerical simulations, are represented by the LS [76], Shen [77], HS [78] and SFHo [18] EOSs.

In general, both microscopic and phenomenological EOSs, in order to be accounted as realistic, should be able to satisfy the constraints on the following parameters [66]:

- The empirical saturation point for symmetric nuclear matter (SNM), $n_0 = 0.17 \pm 0.01$ fm^{-3} and $E_0/A = -16 \pm 1$ MeV;

- The simmetry energy at saturation point, $E_{\rm sym}(n_0) = 30 \pm 2$ MeV;

- The incompressibility parameter at the saturation point for SNM, $K_0 = 220 \pm 30$ MeV;

- The speed of sound c_s shoud never exceed the speed of light c (causality condition), in the relevant range of densities.

As already previously mentioned, this thesis work will concentrate on microscopic EOSs developed in the Brueckner-Hartree-Fock (BHF) framework. In this approach, one first determines the reaction matrix G, which replaces the two-body interaction V with the renormalized interaction in the presence of the medium (see, e.g. Ref. [79] for details):

$$G(\rho;\omega) = V + V \sum_{k_a k_b} \frac{|k_a k_b\rangle\, Q\, \langle k_a k_b|}{\omega - e(k_a) - e(k_b)} G(\rho;\omega)\,, \tag{2.5}$$

where k and $e(k;\rho) = \frac{k^2}{2m} + U(k;\rho)$ respectively represent the particle momentum and energy, Q is the Pauli exclusion operator, ρ represents the density of the medium and ω is the starting energy. Calculating the reaction matrix is then equivalent to solving a Schrodinger equation describing the scattering of two particles in the presence of all the others. The G-matrix is well-behaved even for a singular two-body force, since all terms in this new perturbation series are finite and of reasonable size. [80]. Finally, keeping the two-body correlations, one gets the Brueckner-Hartree-Fock approximation for the binding energy.

2.4 Gravitational wave emission

With the first direct detection [81], gravitational waves represent the last confirmation of Einstein's General Relativity, of which they represent a key prediction. In this regard, Einstein's initial calculation [82] was "marred by an error in calculation", and was corrected in 1918 [83]; his final result stands today as the leading-order 'quadrupole formula' for gravitational wave emission [84]. This formula illustrates that gravitational waves (GWs) arise from accelerated masses exactly as electromagnetic waves arise from accelerated charges; it also shows that very large masses moving at relativistic speeds are needed in order for currently detectable GWs to be produced.

The easiest and most natural starting point in order to derive the gravitational radiation formula from the GR field equations[1] is represented by *linearized gravity*. In details, far from compact objects such as black holes or neutron stars, the spacetime metric $g_{\mu\nu}$ can be regarded as the sum of two contributions: the Minkowski metric $\eta_{\mu\nu}$ representative of the flat spacetime background plus a small perturbation $h_{\mu\nu}$, such that $|h_{\mu\nu}| << 1$:

$$g_{\mu\nu} = \eta_{\mu\nu} + h_{\mu\nu} \,. \tag{2.6}$$

As per usual approach, one can now compute the Christoffel coefficients, which, at first order, are given by:

$$\Gamma^{\lambda}_{\mu\nu} = \frac{1}{2}\eta^{\lambda\rho}(\partial_\nu h_{\rho\mu} + \partial_\mu h_{\rho\nu} - \partial_\rho h_{\mu\nu}) \,. \tag{2.7}$$

From these coefficients, one can first construct the Ricci tensor $R_{\mu\nu}$ according to

$$R_{\mu\nu} = \partial_\lambda \Gamma^{\lambda}_{\mu\nu} - \partial_\nu \Gamma^{\lambda}_{\lambda\mu} + \Gamma^{\lambda}_{\mu\rho}\Gamma^{\rho}_{\nu\mu} - \Gamma^{\lambda}_{\nu\rho}\Gamma^{\rho}_{\lambda\mu} \,, \tag{2.8}$$

and then write the following Einstein field equations

$$R_{\mu\nu} - \frac{1}{2}R g_{\mu\nu} = 8\pi T_{\mu\nu} \,, \tag{2.9}$$

[1] This thesis work does not include a discussion on the principles of General Relativity, for which the reader is instead referred to the textbooks of Refs. [85–87].

where $R = g_{\mu\nu}R^{\mu\nu}$ represents the scalar curvature and $T_{\mu\nu}$ is the stress-energy tensor. In the linearized gravity approximation, in particular, it can be shown that the Einstein tensor can be written as follows:

$$G_{\mu\nu} = R_{\mu\nu} - \frac{1}{2}\eta_{\mu\nu}R = \frac{1}{2}(\partial_\lambda\partial_\nu h^\lambda_\mu + \partial^\lambda\partial_\mu h_{\nu\lambda} - \Box h_{\mu\nu} - \partial_\mu\partial_\nu h - \eta_{\mu\nu}\partial_\lambda\partial^\rho h^\lambda_\rho + \eta_{\mu\nu}\Box h)\,, \quad (2.10)$$

where $h = \eta^{\mu\nu}h_{\mu\nu}$ denotes the trace of the perturbation metric. This expression can be simplified if, rather than considering the metric perturbation $h_{\mu\nu}$, one uses the trace-reversed perturbation $\tilde{h}_{\mu\nu} = h_{\mu\nu} - \frac{1}{2}\eta_{\mu\nu}h$; therefore,

$$G_{\mu\nu} = \frac{1}{2}(\partial_\lambda\partial_\nu\tilde{h}^\lambda_\mu + \partial^\lambda\partial_\mu\tilde{h}_{\nu\lambda} - \Box\tilde{h}_{\mu\nu} - \eta_{\mu\nu}\partial_\lambda\partial^\rho\tilde{h}^\lambda_\rho)\,. \quad (2.11)$$

This expression can be simplified even further by choosing an appropriate gauge; a general infinitesimal coordinate transformation can be written as $x^{\mu'} = x^\mu + \xi^\mu$ and it can be shown that the linearised theory is invariant under the gauge transformation

$$h_{\mu\nu} \to h_{\mu\nu} + 2\partial_{(\mu}\xi_{\nu)}\,. \quad (2.12)$$

One can then make the choice of the *Lorentz* gauge:

$$\partial^\mu\tilde{h}_{\mu\nu} = 0\,. \quad (2.13)$$

With this choice, the field equation are written according to

$$\Box\tilde{h}_{\mu\nu} = -16\pi T_{\mu\nu}\,, \quad (2.14)$$

which in vacuum reduce to $\Box\tilde{h}_{\mu\nu} = 0$; interestingly, the Einstein field equations have now the form of wave equations for $\tilde{h}_{\mu\nu}$.

For asymptotically flat spacetimes with global vacuum, where $T_{\mu\nu} = 0$ everywhere and $h_{\mu\nu} \to 0$ as $r \to \infty$, one can further specialize the gauge to be purely spatial, i.e. $h_{t\nu} = 0$, and traceless, i.e. $h = 0$. This, together with the Lorentz gauge, Eq. (2.13), determines that the spatial metric perturbation is also transverse, i.e. $\partial^\mu h_{\mu\nu} = 0$. In this gauge, also called

Transverse-Traceless, or TT gauge, the perturbation $h_{\mu\nu}$ can be written in matrix form as

$$h_{\mu\nu} = \begin{pmatrix} 0 & 0 & 0 & 0 \\ 0 & h_+ & h_\times & 0 \\ 0 & h_\times & h_+ & 0 \\ 0 & 0 & 0 & 0 \end{pmatrix} , \tag{2.15}$$

where h_+ and $h_\times$ represent the two possible polarizations for the gravitational wave propagating in vacuum. The GW acts tidally, squeezing along one axis and stretching along the other; while the + polarization acts on the x and y axes, the effect of the $\times$ polarization is observed along a set of axes which are rotated with respect to the former axes by 45° [84].

If one considers instead the generation of gravitational waves in the linearized approach, then the non-zero right hand side of Eq. (2.14) has to be considered. It is possible to show (see e.g. Ref. [84] for the full derivation) that, for each component of the metric perturbation, the following equality holds:

$$\tilde{h}_{\mu\nu}(t, \mathbf{x}) = 4 \int d^3x' \frac{T_{\mu\nu}(t - |\mathbf{x} - \mathbf{x}'|, \mathbf{x}')}{|\mathbf{x} - \mathbf{x}'|} , \tag{2.16}$$

where the term $t - |\mathbf{x} - \mathbf{x}'|$ is representative of the retarded time. In the simplified case of the metric perturbation being evaluated in a very far position from the source, the denominator can be substituted as $|\mathbf{x} - \mathbf{x}'| \approx r$, with r being much greater than the source typical size. With these replacements, Eq. (2.16) can be written as

$$\tilde{h}_{\mu\nu}(t, \mathbf{x}) = \frac{4}{r} \int d^3x' T_{\mu\nu}(t - r, \mathbf{x}') . \tag{2.17}$$

This last equation can be written differently if one imposes the conservation of the stress-energy tensor, i.e. $\partial_\mu T^{\mu\nu}$; in particular, considering the time component of the conservation equation ($\partial_0 T^{00} = -\partial_i T^{i0}$) and differentiating with respect to time holds

$$\partial_0^2 T^{00} = -\partial_0 \partial_i T^{i0} = \partial_i \partial_j T^{ij} , \tag{2.18}$$

where the conservation equation has been used again in the last equality. If both sides of this equation are multiplied by $x^i x^j$, the integration over the total volume can be written as

$$\int d^3x' T^{ij}(\mathbf{x}) = \frac{1}{2}\partial_0^2 \int d^3x' x'^i x'^j T^{00}\,, \tag{2.19}$$

where Gauss's theorem has been used in order to recast volume integrals as surface integrals, whose contribution is zero when the surface is taken outside the source. Introducing the second mass moment I_{ij} defined as

$$I_{ij} \equiv \int d^3x' \rho(t, \mathbf{x}') x'^i x'^j\,, \tag{2.20}$$

Eq. (2.17) can be written as

$$\tilde{h}_{\mu\nu}(t, \mathbf{x}) = \frac{2}{r}\frac{d^2 I_{ij}(t-r)}{dt^2}\,. \tag{2.21}$$

Defining the quadrupole moment tensor Q_{ij} according to

$$Q_{ij} \equiv I_{ij} - \frac{1}{3}\eta_{ij} I\,, \tag{2.22}$$

with I being the trace of tensor I_{ij}, and projecting Eq. (2.21) in the TT gauge, one obtains the final quadrupole formula

$$h_{ij}^{TT}(t, \mathrm{x})\frac{2}{r}\frac{d^2 Q_{ij}(t-\mathbf{r})}{dt^2}[P_{ik}P_{jl} - \frac{1}{2}P_{kl}P_{ij}]\,, \tag{2.23}$$

where the projection tensor $P_{ij} = \eta_{ij} - n_i n_j$ is defined in terms of the local direction of propagation $\mathbf{n} = \frac{\mathbf{x}}{\mathbf{r}}$.

Linearized theory well describes the propagation of GWs through universe; however, many sources have very strong self gravity and the linearized treatment becomes inadequate. In such cases, three main approaches are suitable [84]:

- *Post-Newtonian (PN) theory*, where an iterated expansion in two variables is considered, namely the gravitational potential $\phi \sim M/r$, where r is the distance from the source and M represents a mass scale for the system, and the characteristic velocity v. The PN expansion converges rather poorly in the latest phases of the inspiral, which involve the highest

velocities; among the possible methods used to overcome this issue, the Effective One Body (EOB) model [4, 88] has proven particularly successful. The analytical EOB model contains an effective Hamiltonian which resums the PN series in a suitable way to better embody the effects of the strong-field regime [89]; the latter can be further supplemented by input from numerical relativity simulations, thus extending its validity through the merger and following stages (see, e.g., Ref. [90] and references therein for a recent discussion).

- *Numerical Relativity (NR)*, where Einstein's equations are numerically solved on a computer. This technique does not rely on any approximation and thus is well suited to describe the very last phases of the inspiral, the merger and the post-merger phases of a binary compact object merger, where general relativistic effects are strongest.

- *Perturbation theory*, where the spacetime $g_{\mu\nu}$ is treated according to some exact background $g^B_{\mu\nu}$ (depending on the investigated case) plus a perturbation $h_{\mu\nu}$ which needs to be small, i.e. $||h_{\mu\nu}/g^B_{\mu\nu}|| << 1$. This approach proves to be effective, for example, when modeling the post-merger remnant of a binary black hole merger, i.e. a Kerr black hole plus some distortion quickly radiated away.

2.5 Numerical relativity simulations of BNS mergers

The qualitative evolution of BNS mergers can be divided into three main phases. A first *inspiral* phase, in which the two stars orbit around their common center of mass, with orbits shrinking in time due to the emission of gravitational waves, starts immediately after the NS-NS system is born and lasts for the entire lifetime of the system, except for the last few milliseconds. Once the binary separation becomes of a few tens of kilometers, the system rapidly becomes unstable; after these final orbits, the stars plunge together in a phase known as the *merger* phase. This phase is followed by a *post-merger* phase, where the final object can either immediately collapse to a black hole if massive enough, or remain stable for a certain amount of time. In details, if the remnant mass does not exceed the TOV limit of

an isolated, non-rotating NS, the newly formed NS will remain stable; a remnant can be *supramassive* if its mass exceeds the TOV limit but does not exceed the mass limit for an uniformly rotating star, while it's referred to as *hypermassive* if its mass exceeds the latter limit but does not exceed the mass limit for a differentially rotating NS (see, e.g., Ref. [91] for further details on this classification).

In order to accurately characterize these last phases of the evolution of a binary system, the spacetime equations, together with the relativistic hydrodynamic equations, have to be solved numerically on a computer. In particular, Einstein's equations can't be solved in their standard formalism, and have to be cast in a specific form, which allows one to perform time evolutions of appropriate initial data by decoupling space and time; a discussion of this approach, also known as the *3+1 decomposition*, as well as common formalisms like the BSSN or CCZ4 used in numerical simulations is described in detail in paragraph 2.5.1.

Differently from simulations of black holes, the simulation of neutron stars involves a certain care with respect to the solution of the hydrodynamics equations; a brief overview, in this respect, is given in paragraph 2.5.2, although the reader should refer to more detailed references, such as [92].

The framework and the techniques used also deserve great importance, and paragraph 2.5.3 is indeed dedicated to the codes and the relevant methods used for the simulations presented in this thesis work.

2.5.1 3+1 decomposition of Einstein's equations

In 1962, Richard Arnowitt, Stanley Deser and Charles Misner determined, by applying an Hamiltonian approach to General Relativity, a new formulation of the same theory, today referred to as ADM formulation [93]. An important feature of such a formulation is represented by the fact that space and time are decoupled, a feature referred to as 3+1 decomposition of the spacetime; this is not only a perspective closer to everyday life, since the most intuitive

concept is not, in fact, the one of a spacetime geometry, but that of a temporal succession of spatial geometries, but is also more suitable to computational implementations.

In order to perform a 3+1 decomposition of the spacetime equations, one first needs to *foliate* the spacetime: given a n-dimensional manifold M, one can define a hypersurface Σ of M, being a *n-1*-submanifold of M, image of the embedding[2] $\Phi : \hat{\Sigma} \to M$[94]. A foliation or slicing of M means that there exists a regular scalar function t such that every hypersurface Σ is a level surface of this scalar field; in the context of spacetime, t can be chosen to be the coordinate time. With this choice, the normal vector to every hypersurface is defined in terms of $\nabla_\mu t$, and, in details, the normal unit vector to $\Sigma(t)$ is written as

$$n_\mu = -\alpha \nabla_\mu t \,, \tag{2.24}$$

where α is the lapse function.

In general, chosen a point of coordinates x^μ on a hypersurface Σ_t, one can describe its evolution in time as a sum of two contributions, i.e. a timelike vector of the kind $\alpha \mathbf{n}$ and a spacelike vector $\boldsymbol{\beta}$, such that $\boldsymbol{\partial}_t = \alpha \boldsymbol{n} + \boldsymbol{\beta}$. Furthermore, once the normal unit vector to each hypersurface has been defined, one can define the induced 3-metric on each surface, $\gamma_{\mu\nu}$, as the projection of the 4-metric $g_{\mu\nu}$ according to

$$\gamma_{\mu\nu} = g_{\mu\nu} + n_\mu n_\nu \,. \tag{2.25}$$

The normal vector is expressible in terms of α and β (see, e.g., Ref. [94] for a complete derivation), being in particular

$$n^\mu = \left(\frac{1}{\alpha}, \frac{\beta^i}{\alpha} \right) , \tag{2.26}$$

with the related co-vector being represented instead by

$$n_\mu = (-\alpha, 0) \,. \tag{2.27}$$

The description of this notation is complemented by writing the line element explicitly

$$ds^2 = -\alpha^2 dt^2 + \gamma_{ij} (dx^i + \beta^i dt)(dx^j + \beta^j dt) \,, \tag{2.28}$$

[2]The embedding $\Phi : \hat{\Sigma} \to \Sigma$ is a homeomorphism, i.e. a bijection such that Φ and Φ^{-1} are continuous.

and introducing the following extrinsic curvature tensor

$$\boldsymbol{K} = -\boldsymbol{P}\nabla\boldsymbol{n}\,, \tag{2.29}$$

with $P_{\mu\nu} = \gamma_{\mu\nu} + n_\mu n_\nu$ representing the spatial projection operator.

Starting from these results, one can set Einstein's equations in the new form; the decomposition of the right hand side is immediate and consists in the projection of the stress-energy tensor into the following *energy density*, *momentum density* and *stress tensor*:

$$\rho \equiv T^{\mu\nu} n_\mu n_\nu\,, \tag{2.30}$$

$$j^\alpha = S^\alpha \equiv -P^{\alpha\mu} n^\nu T_{\mu\nu}\,, \tag{2.31}$$

$$S_{\mu\nu} \equiv P^\alpha_\mu P^\beta_\nu T_{\alpha\beta}\,. \tag{2.32}$$

The decomposition of the left hand side involves expressing the four-dimensional Riemann tensor in terms of the three-dimensional Riemann tensor of the hypersurface Σ and the extrinsic curvature tensor [95]; the complete derivation of these relations is rather long, and only the final results will be presented here (the interested reader can see e.g. Ref. [96]). The full projection of the Riemann tensor on the spatial hypersurfaces is given by the *Gauss-Codazzi* equations[3]

$$P^\delta_\alpha P^\kappa_\beta P^\lambda_\mu P^\sigma_\nu R_{\delta\kappa\lambda\sigma} = {}^{(3)}R_{\alpha\beta\mu\nu} + K_{\alpha\mu}K_{\beta\nu} - K_{\alpha\nu}K_{\beta\mu}\,, \tag{2.33}$$

where the the three-dimensional Riemann tensor ${}^{(3)}R_{\alpha\beta\mu\nu}$ has been introduced. The projection of the same tensor on the hypersurfaces with one contraction with respect to the normal vector characterizes the *Codazzi-Mainardi* equations instead:

$$P^\delta_\alpha P^\kappa_\beta P^\lambda_\mu n^\nu R_{\delta\kappa\lambda\sigma} = D_\beta K_{\alpha\mu} - D_\alpha K_{\beta\mu}\,, \tag{2.34}$$

where the projected covariant derivative $D_\alpha = P^\mu_\alpha \nabla_\mu$ has been used. In order to rewrite the Einstein equations in the 3+1 form, one first uses that

$$P^{\alpha\mu}P^{\beta\nu}R_{\alpha\beta\mu\nu} = (g^{\alpha\mu} + n^\alpha n^\mu)(g^{\beta\nu} + n^\beta n^\nu)R_{\alpha\beta\mu\nu} = 2n^\mu n^\nu G_{\mu\nu}\,, \tag{2.35}$$

[3]The notation used hereon closely follows the one used in Ref. [95].

and, by using the Gauss-Codazzi equation, one obtains

$$2n^\mu n^\nu G_{\mu\nu} = {}^{(3)}R + K^2 - K^{\mu\nu}K_{\mu\nu}\,, \tag{2.36}$$

which, in turn, through the Einstein equations becomes

$${}^{(3)}R + K^2 - K_{\mu\nu}K^{\mu\nu} = 16\pi\rho\,, \tag{2.37}$$

One can immediately notice that this equation does not contain any time derivatives, so it is not an evolution equation but rather a constraint which has to be verified at each time; such an equation is indeed known as the *Hamiltonian constraint*.

From the mixed contraction of the Einstein tensor, one finds instead that

$$P^{\alpha\mu}n^\nu G_{\mu\nu} = P^{\alpha\mu}n^\nu R_{\mu\nu}\,, \tag{2.38}$$

which can be rewritten using the Codazzi-Mainardi equations, reading

$$\gamma^{\alpha\mu}n^\nu G_{\mu\nu} = D^\alpha K - D_\mu K^{\alpha\mu}\,, \tag{2.39}$$

where D_i represents the covariant derivative with respect to γ_{ij}. Lastly, using the Einstein equations, one finds

$$D_\mu(K^{\alpha\mu} - \gamma^{\alpha\mu}K) = 8\pi j^\alpha\,. \tag{2.40}$$

The three non trivial equations are again purely spatial and do not involve any time evolution; they are known as the *momentum constraints*.

The evolution equations for the metric and the extrinsic curvature can be also determined with no particular difficulty. In particular, it follows directly from the definition of the extrinsic curvature tensor that

$$K_{\mu\nu} = -\frac{1}{2}\pounds_{\boldsymbol{n}}\gamma_{\mu\nu}\,, \tag{2.41}$$

where the Lie derivative symbol $\pounds$ has been used; this equation can be rewritten, with some algebra involving the complete expression of the Lie derivative of the three-metric, as

$$\partial_t\gamma_{ij} = -2\alpha K_{ij} + D_i\beta_j + D_j\beta_i\,. \tag{2.42}$$

The evolution equation for the extrinsic curvature can be instead derived by considering first the following contraction of the Riemann tensor

$$P^{\delta}_{\mu}P^{\kappa}_{\nu}n^{\lambda}n^{\sigma}R_{\delta\kappa\lambda\sigma} = \pounds_{\boldsymbol{n}}K_{\mu\nu} + K_{\mu\lambda}K^{\lambda}_{\nu} + \frac{1}{\alpha}D_{\mu}D_{\nu}\alpha\,. \tag{2.43}$$

Using then the Gauss-Codazzi equations with the previous one, implies

$$\pounds_{\boldsymbol{t}}K_{\mu\nu} - \pounds_{\boldsymbol{\beta}}K_{\mu\nu} = -D_{\mu}D_{\nu}\alpha + \alpha(-P^{\delta}_{\mu}P^{\kappa}_{\nu}R_{\delta\kappa} + {}^{(3)}R_{\mu\nu} + KK_{\mu\nu} - 2K_{\mu\lambda}K^{\lambda}_{\nu})\,, \tag{2.44}$$

which can in turn be written as

$$\partial_t K_{\mu\nu} = \pounds_{\boldsymbol{\beta}}K_{\mu\nu} - D_{\mu}D_{\nu}\alpha + \alpha[{}^{(3)}R_{\mu\nu} + KK_{\mu\nu} - 2K_{\mu\lambda}K^{\lambda}_{\nu}] + 4\pi\alpha[\gamma_{\mu\nu}(S-\rho) - 2S_{\mu\nu}]\,, \tag{2.45}$$

where the Einstein field equations have been substituted. Equations (2.42), (2.45), (2.37) and (2.40) characterize the full set of the ADM equations, where, after specifying appropriate initial data (which should be fulfilling Eqs. (2.45), (2.37), namely, the constraint equations), Eqs. (2.42), (2.45) determine the time evolution. The lapse function α and the shift vector $\boldsymbol{\beta}$ are gauge variables whose governing equations can be chosen according to the considered problem (widely used prescriptions are represented by the Bona-Massò slicing condition [97] for the lapse and the Gamma-driver shift condition [98] for the shift vector); interestingly, the constraint equations do not depend on these gauge variables, since these equations are to be solved at every hypersurface, while the gauge variables relate quantities on adjacent hypersurfaces.

The ADM equations are however affected by an important problem, which limits their application in long-term simulations: stable evolutions are difficult to obtain since these equations are weakly hyperbolic [99]. It is nevertheless possible to reformulate the ADM equations in order to obtain a strongly hyperbolic set of equations. In this regard, the most commonly used formulation is the Baumgarte-Shapiro-Shibata-Nakamura (BSSN) [100, 101], which is based on a conformal rescaling of the three-dimensional metric. In particular, a conformal factor ψ is introduced such that

$$\tilde{\gamma}_{ij} \equiv \psi^{-4}\gamma_{ij}\,, \tag{2.46}$$

where $\tilde{\gamma}_{ij}$ is an auxiliary metric on Σ_t. The BSSN formulation also introduces a trace-free extrinsic curvature A_{ij}, defined as follows:

$$A_{ij} \equiv K_{ij} - \frac{1}{3}\gamma_{ij}K\,, \tag{2.47}$$

which, in turn, is rescaled according to

$$\tilde{A}_{ij} = \psi^2 A_{ij}\,. \tag{2.48}$$

Finally, the conformal connection functions

$$\tilde{\Gamma}^i = \tilde{\gamma}^{jk}\tilde{\Gamma}^i{}_{jk} = -\partial_j\tilde{\gamma}^{ij}, \tag{2.49}$$

are introduced. In practice, one usually works with $\phi = \log\psi$, such that $\tilde{\gamma}_{ij} \equiv e^{-4\phi}\gamma_{ij}$; therefore, the final set of evolution variables is now represented by ϕ, K, $\tilde{\gamma}_{ij}$, $\tilde{A}_{ij}$ and $\tilde{\Gamma}^i$.

The evolution equations for all the BSSN variables are

$$\partial_t\tilde{\gamma}_{ij} = \beta^k\partial_k\tilde{\gamma}_{ij} + \partial_i\beta^k\tilde{\gamma}_{kj} + \partial_j\beta^k\tilde{\gamma}_{ik} - \frac{2}{3}\tilde{\gamma}_{ij}\partial_k\beta^k - 2\alpha\tilde{A}_{ij}, \tag{2.50}$$

$$\partial_t\phi = -\frac{1}{6}\alpha K + \beta^k\partial_k\phi + \frac{1}{6}\partial_k\beta^k, \tag{2.51}$$

$$\begin{aligned}\partial_t\tilde{A}_{ij} = {} & e^{-4\phi}[-D_iD_j\alpha + \alpha({}^{(3)}R_{ij} - 8\pi S_{ij})]^{TF} \\ & + \alpha(K\tilde{A}_{ij} - 2\tilde{A}_{ik}\tilde{A}^k{}_j) + \beta^k\partial_k\tilde{A}_{ij} + \partial_i\beta^k\tilde{A}_{kj} + \partial_j\beta^k\tilde{A}_{ik} - \frac{2}{3}\tilde{A}_{ij}\partial_k\beta^k,\end{aligned} \tag{2.52}$$

$$\partial_tK = -D^iD_i\alpha + \alpha(\tilde{A}_{ij}\tilde{A}^{ij} + \frac{1}{3}K^2) + \beta^k\partial_kK + 4\pi\alpha(\rho + S), \tag{2.53}$$

$$\begin{aligned}\partial_t\tilde{\Gamma}^i = {} & \tilde{\gamma}^{jk}\partial_j\partial_k\beta^i + \frac{1}{3}\tilde{\gamma}^{ij}\partial_j\partial_k\beta^k + \beta^j\partial_j\tilde{\Gamma}^i - \tilde{\Gamma}^j\partial_j\beta^i + \frac{2}{3}\tilde{\Gamma}^i\partial_j\beta^j \\ & - 2\tilde{A}^{ij}\partial_j\alpha + 2\alpha(\tilde{\Gamma}^i{}_{jk}\tilde{A}^{jk} + 6\tilde{A}^{ij}\partial_j\phi - \frac{2}{3}\tilde{\gamma}^{ij}\partial_jK - 8\pi\tilde{\gamma}^{ij}S_j),\end{aligned} \tag{2.54}$$

where the index "TF" denotes the trace-free part of the bracketed tensorial quantity. This new system turns out to be far more stable than ADM in all cases studied until now [95] and is widely employed in numerical simulations. Among the characteristics of the BSSN formulation, one is actually a drawback and is represented by the fact that the constraint subsystem has a zero-speed characteristic for the Hamiltonian constraint [102]. In other

words, violations of the constraints do not propagate and, if during the evolution the violation of the constraints increases, it will continue for the rest of the evolution, spoiling the accuracy of the solution [92]. It is indeed possible to introduce a further formulation of the Einstein equations which has the desirable feature of *constraint damping* during the time evolution. A possible starting point, in this sense, is represented by modifying the original Einstein equations with the implementation of a new 4-vector of constraints Z^μ [92] according to

$$R_{\mu\nu} + 2\nabla_{(\mu}Z_{\nu)} + k_1[2n_{(\mu}Z_{\nu)} - (1+k_2)g_{\mu\nu}n_\sigma Z^\sigma] = 8\pi(T_{\mu\nu} - \frac{1}{2}Tg_{\mu\nu})\,, \tag{2.55}$$

where k_1 and k_2 are two free parameters representatives of the constraint damping; in particular, it has been shown that optimal choices for these parameters, in order to ensure an effective constraint damping, are $k_1 > 0$ and $k_2 > -1$ [103]. The formulation adopted in this thesis work, the CCZ4, is indeed based on this idea. One introduces first new evolution variables, i.e.

$$\Theta \equiv -n_\mu Z^\mu = \alpha Z^0\,, \tag{2.56}$$

and the modified conformal connection functions, which are related to the BSSN defined ones according to

$$\hat{\Gamma}^i \equiv \tilde{\Gamma}^i + 2\tilde{\gamma}^{ij}Z_j\,. \tag{2.57}$$

In the formulation presented here, a further coefficient k_3 is introduced to improve the stability properties of the system [104], which is generally chosen to be $k_3 = 1$.

In this case, the evolution equations read:

$$\partial_t \tilde{\gamma}_{ij} = \beta^k \partial_k \tilde{\gamma}_{ij} + \partial_i \beta^k \tilde{\gamma}_{kj} + \partial_j \beta^k \tilde{\gamma}_{ik} - \frac{2}{3}\tilde{\gamma}_{ij}\partial_k \beta^k - 2\alpha \tilde{A}_{ij}, \tag{2.58}$$

$$\partial_t \phi = \frac{1}{6}\alpha K + \beta^k \partial_k \phi + \frac{1}{6}\partial_k \beta^k, \tag{2.59}$$

$$\begin{aligned}\partial_t \tilde{A}_{ij} = {} & e^{-4\phi}[-D_i D_j \alpha + \alpha({}^{(3)}R_{ij} + D_i Z_j + D_j Z_i - 8\pi S_{ij})]^{TF} - 2\alpha \tilde{A}_{ik}\tilde{A}^k{}_j \\ & + \alpha \tilde{A}_{ij}(K - 2\Theta) + \beta^k \partial_k \tilde{A}_{ij} + \partial_i \beta^k \tilde{A}_{kj} + \partial_j \beta^k \tilde{A}_{ik} - \frac{2}{3}\tilde{A}_{ij}\partial_k \beta^k,\end{aligned} \tag{2.60}$$

$$\begin{aligned}\partial_t K = {} & - D^i D_i \alpha + \alpha({}^{(3)}R + 2D_j Z^j + K^2 - 2\Theta K) + \beta^i \partial_i K \\ & - 3\alpha k_1(1 + k_2)\Theta + 4\pi\alpha(S - 3\rho),\end{aligned} \tag{2.61}$$

$$\begin{aligned}\partial_t \hat{\Gamma}^i = {} & \tilde{\gamma}^{jk}\partial_j \partial_k \beta^i + \frac{1}{3}\tilde{\gamma}^{ij}\partial_j \partial_k \beta^k + \beta^j \partial_j \hat{\Gamma}^i - \tilde{\Gamma}^j \partial_j \beta^i + \frac{2}{3}\tilde{\Gamma}^i \partial_j \beta^j \\ & + 2\alpha(\tilde{\Gamma}^i{}_{jk}\tilde{A}^{jk} + 6\tilde{A}^{ij}\partial_j \phi - \frac{2}{3}\tilde{\gamma}^{ij}\partial_j K - 8\pi\tilde{\gamma}^{ij}S_j) \\ & + 2\tilde{\gamma}^{ij}(\alpha\partial_j \Theta - \Theta\partial_j \alpha - \frac{2}{3}\alpha K Z_j) + 2k_3(\frac{2}{3}\tilde{\gamma}^{ij}Z_j \partial_k \beta^k - \tilde{\gamma}^{jk}Z_j \partial_k \beta^i) \\ & - 2\tilde{A}^{ij}\partial_j \alpha - 2\alpha k_1 \tilde{\gamma}^{ij}Z_j,\end{aligned} \tag{2.62}$$

$$\begin{aligned}\partial_t \Theta = {} & \frac{1}{2}\alpha({}^{(3)}R + 2D_j Z^j - \tilde{A}_{ij}\tilde{A}^{ij} + \frac{2}{3}K^2 - 2\Theta K) - Z^j \partial_j \alpha \\ & + \beta^j \partial_j \Theta - \alpha k_1(2 + k_2)\Theta - 8\pi\alpha\rho.\end{aligned} \tag{2.63}$$

These new equations reduce to the BSSN ones in the limit $Z_i = 0 = \Theta$; the evolution equation for K, however, does not reduce to the corresponding BSSN one, since it does not make use of the Hamiltonian constraint to remove the Ricci scalar from the right-hand side [92]. It is also important to notice that the K used here is related to the BSSN one according to

$$K_{\mathrm{BSSN}} = K - 2\Theta \tag{2.64}$$

and so, in general, the two variables do not coincide [104]. In the context of the BNS merger simulations presented in thesis work, where no specified otherwise, $k_1 = 0.06$ and $k_2 = 0.00$ are assumed; part of this thesis work also focuses on an alternative CCZ4 formulation, named *fCCZ4*, which is discussed in detail in Sec. 7.2.

2.5.2 Hydrodynamic equations

In order to determine the equations governing matter, one starts with the conservation equations for the fluid considered; in the context of the simulations presented in this thesis work, a perfect fluid is always assumed. In particular, the starting point is usually represented by the energy-momentum conservation law

$$\nabla_\nu T^{\mu\nu} = 0\,, \tag{2.65}$$

which results in the (relativistic) Euler equation and the conservation of total energy, and the following conservation of the baryon number of the fluid:

$$\nabla_\nu (\rho u^\nu) = 0\,, \tag{2.66}$$

which results in the continuity equation. Here, $T^{\mu\nu} = \rho h u^\mu u^\nu + p g^{\mu\nu}$ is the stress-energy tensor of a perfect fluid, with ρ, h, $\boldsymbol{u}$ and p being the energy density, specific enthalpy, 4-velocity and pressure of the fluid respectively. Eqs. (2.65) and (2.66) alone still do not completely describe the fluid motion, and they are to be complemented by prescribing an EOS for the considered fluid. In this regard, important examples of widely used EOSs are:

- the *ideal-gas* EOS, $p = (\Gamma - 1)\rho\epsilon$, where the density ρ and the specific internal energy ϵ are related to the pressure p via the adiabatic index of the gas Γ;

- the *polytropic* EOS, $p = K\rho^\Gamma$, where K and Γ are the polytropic constant and exponent respectively. This case represents a restriction of the previous one to isentropic flows;

- the *piecewise-polytropic* EOS, $p = K_i\rho^{\Gamma_i}$, where n values of K and Γ are defined relatively to different density ranges;

- the *hybrid* EOS, where a cold polytrope, or a zero-temperature EOS in tabulated form, is supplied by an ideal gas contribution in order to mimic finite temperature effects. This kind of EOS is discussed in further detail in Sec. 5.1.

In order to work with a hyperbolic system of equations (which is preferable for a number of reasons, see e.g. Ref. [92] for a detailed discussion), the "Valencia" formulation [105] is

generally employed in numerical codes. In this formulation, the following *conserved variables* are introduced

$$D \equiv \rho\alpha u^t = \rho W, \tag{2.67}$$

$$S^{\mu\nu} = \rho h W^2 v^\mu v^\nu + p\gamma^{\mu\nu}, \tag{2.68}$$

$$S^\mu = \rho h W^2 v^\mu, \tag{2.69}$$

$$E = \rho h W^2 - p\,, \tag{2.70}$$

where the fluid velocity measured by a normal observer $\boldsymbol{v}$ is a purely spatial vector whose components are related to the 4-velocity through $v^i = u^i/W + \beta^i/\alpha$.

The relativistic-hydrodynamic equations are then cast in the compact form

$$\partial_t(\sqrt{\gamma}\boldsymbol{U}) + \partial_i(\sqrt{\gamma}\boldsymbol{F}^i) = \boldsymbol{S}\,, \tag{2.71}$$

where, in addition to the 3-metric determinant γ, the following vectors appear: the vector of conserved variables $\boldsymbol{U}$,

$$\boldsymbol{U} \equiv \begin{pmatrix} D \\ S_j \\ E \end{pmatrix} = \begin{pmatrix} \rho W \\ \rho h W^2 v_j \\ \rho h W^2 - p \end{pmatrix}, \tag{2.72}$$

the *flux vector* in the i-th direction,

$$\boldsymbol{F}^i \equiv \begin{pmatrix} \alpha v^i D - \beta^i D \\ \alpha S^i_j - \beta^i S_j \\ \alpha S^i - \beta^i E \end{pmatrix}, \tag{2.73}$$

and the *source vector* $\boldsymbol{S}$,

$$\boldsymbol{S} \equiv \sqrt{\gamma}\begin{pmatrix} 0 \\ \frac{1}{2}\alpha S^{ik}\partial_j\gamma_{ik} + S_i\partial_j\beta^i - E\partial_j\alpha \\ \alpha S^{ij}K_{ij} - S^j\partial_j\alpha \end{pmatrix}. \tag{2.74}$$

While the variables involved in the numerical solution of the hydrodynamic equations are of course the conserved ones, the fluxes and source terms are, in numerical codes, computed

also in terms of the *primitive* variables, i.e. ρ, v^i, p. While the conversion of the variables from primitive to conserved is analytical via Eqs. (2.67), (2.68), (2.69) and (2.70), the conversion from conserved to primitive is not possible analytically and a numerical procedure is necessary[4].

2.5.3 General information on the numerical setup

In order to perform a BNS merger simulation, one needs first to create suitable initial data which can be later evolved in time. In this regard, for the simulations presented in this thesis work, initial data for irrotational binary neutron stars computed using the multi-domain spectral-method code `LORENE` [106, 107] are considered. Given a tabulated EOS and the initial separation between the stars with the chosen mass as input, the code solves the conformal thin sandwich equations [108] in order to determine a quasi-circular configuration for the two irrotational components of the system; indeed, in the final stages of the inspiral phase, the eccentricity of these systems is believed to be almost absent, since the gravitational radiation reaction circularizes most of the binaries before they enter the sensitive bands of gravitational-wave detectors [109, 110]. The irrotational configuration is justified instead by the fact that the orbital period of BNSs in the small time window simulated before the merger is much smaller than typical rotational periods of observed neutron stars [111]; furthermore, spins shouldn't significantly increase due to tidal effects, as the viscosity of neutron-star matter is expected to be too low for this process to be efficient [112, 113].

The binary neutron star simulations presented in this thesis work are performed in full General Relativity using the fourth-order finite-differencing code McLachlan [114], which is part of the publicly available Einstein Toolkit [115] framework. The code solves the CCZ4 formulation of the Einstein equations [5, 104, 116], with a "1+log" slicing condition and a "Gamma driver" shift condition [98, 117]. The general-relativistic hydrodynamics equations

[4] An exhaustive and recent treatment is included in Appendix D of Ref.[92].

are solved using the `WhiskyTHC` code [118–120], which uses either finite-volume or high-order finite-differencing high-resolution shock-capturing methods. The time integration of the coupled set of hydrodynamic and Einstein equations is performed using the method of lines with an explicit third-order Runge-Kutta method, with a Courant-Friedrichs-Lewy (CFL) number of 0.15 to compute the timestep. The Riemann problem is solved using either the LLF [121, 122] (employed in the simulations presented in Ch. 5) or the HLLE solver [123, 124] (adopted instead in Ch. 6).

Although matter compression and shocks increase the temperature of the remnant to several tens of MeV [125], neutrino emission acts as cooling mechanism and is implemented in the simulations employing finite temperature EOSs, as only in the latter the electron fraction is consistently evolved in time. In these cases, the effects on matter due to weak reactions are treated using the gray (energy-averaged) neutrino-leakage scheme described in Refs. [126, 127], and free-streaming neutrinos are evolved according to the M0 heating scheme introduced in Refs. [127, 128].

To ensure the non-linear stability of the spacetime evolution, a fifth-order Kreiss-Oliger-type artificial dissipation [129] is added. All the simulations are performed with an Adaptive Mesh Refinement (AMR) approach, where the grid hierarchy is handled by the Carpet driver [130]. Such a hierarchy consists of six refinement levels with a grid resolution varying from $h_5 = 0.16 M_\odot$ (i.e., $\sim 236\,\mathrm{m}$) for the finest level, to $h_0 = 5.12 M_\odot$ (i.e., $\sim 7.5\,\mathrm{km}$) for the coarsest level, whose outer boundary is at $1024 M_\odot$ (i.e., $\sim 1515\,\mathrm{km}$). To reduce computational costs, a reflection symmetry across the $z = 0$ plane is always adopted.

CHAPTER 3

THE MICROSCOPIC EOS SET

3.1 Equations of state in the BHF framework

In this section, I will introduce the EOSs used in the numerical simulations and the studies presented in this thesis work; in particular, the complete set has been considered in Ref. [23], while only a part of the complete set has been considered in Refs. [21, 24]. The set is constituted by microscopic EOSs based on many-body calculations; in particular, the Brueckner-Hartree-Fock (BHF) many-body theory with realistic two-body and three-body nucleonic forces [66, 68, 131] is used (see Sec. 2.3 for a brief introduction on the method). In particular, the EOSs considered are based on different nucleon-nucleon potentials: the Argonne V_{18} [132], the Nijmegen 93 N93 [133, 134] and the Bonn B (BOB) [135, 136]. The BOB and N93 potentials are supplemented with three-body forces as described in Refs. [137, 138]; V_{18} is instead combined either with a microscopic or phenomenological three-body force [139, 140], being respectively labelled as V18 or UIX. It is important to remark that three-body forces have to be taken into account within the BHF approach as they not only provide provide an important contribution to the nuclear EOS at high density, but also ensure a realistic saturation point of nuclear matter.

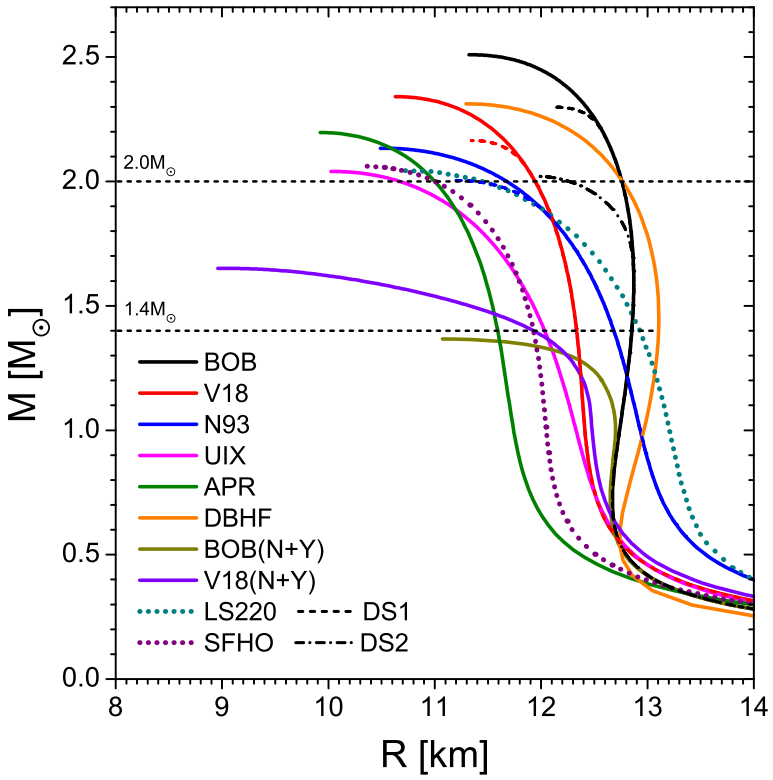

Figure 3.1 Mass-radius diagrams for different microscopic (phenomenological) EOSs, represented as solid (dotted) lines; dashed and dot-dashed lines indicate hybrid stars in the DS approach.

It is also possible, within the BHF theory, to account for the presence of hyperons, which may appear in the core region; the main consequence of this inclusion is characterized by very small NS maximum masses [141–143] with $M_{\rm TOV} < 1.7 M_{\odot}$. The two-families scenario [144–146], however, could represent the way these EOSs are realized: in this picture, indeed, stars with the lightest masses are interpreted as hadronic stars, while the most massive stars are represented by quark stars.

Hybrid stars have also been considered within this work; however, given the difficulty related to performing first-principle calculations of quark matter EOSs at the high densities and zero-temperature regimes present in the NS core, the latter is still poorly known. The

only possibility for describing the quark matter EOS is then represented by phenomenological models such the Nambu-Jona-Lasinio model [147, 148] or the MIT bag model [149]. The Dyson-Schwinger model (DSM) developed in Refs. [150–155] for deconfined quark matter, together with a BHF approach for the hadronic phase, has been used in order to model hybrid stars in Ref. [23] and discussed in this chapter. An interaction parameter α can be varied, such that increasing α leads to more stable quark matter in the DSM, and a Gibbs phase transition to the nucleonic models is constructed.

Fig. 3.1 shows the mass-radius diagrams of the previously discussed EOSs; in particular, the EOSs with the inclusion of hyperons are labeled as (N+Y), while hybrid stars in the DSM approach are identified as DS1 and DS2, where of the α parameter is chosen to be 1 and 2 respectively. The often used APR EOS [73] and the results obtained within the Dirac-BHF method (DBHF) [156, 157] are also included for completeness, together with two phenomenological EOSs, LS220 [76] and SFHo [18], widely employed in simulations. It follows immediately that all the EOSs apart from the N+Y models determine a maximum mass $M_{\rm TOV}$ beyond 2 $M_\odot$; however, hyperonic EOSs will not be excluded from the analysis of the global properties included in this chapter, since it's important to check which other irregularities they manifest with respect to other EOSs.

It also follows from Fig. 3.1 that the NS radii corresponding to $M = 1.4M_\odot$ span a range $11.6 < R_{1.4} < 13.2$ km; these results are in agreement with the ones reported in Ref. [158], where an analysis of the results of GW170817 was performed by using a general polytropic parametrization of the EOS compatible with perturbative QCD at very high density. It has been also shown that the tidal deformability limit of a $1.4M_\odot$ NS, $\Lambda_{1.4} < 800$, as found in GW170817, implies a radius $R_{1.4} < 13.6$ km [158], with similar upper limits also obtained in [159].

It is important to remark that entire set of EOSs considered here, which will be more extensively discussed in the next section, is constituted by zero-temperature EOSs (or zero-temperature, beta-equilibrated cuts of finite-temperature EOSs, as in the case of LS220 and

SFHo), in their tabulated format, suitable for use in numerical codes such as LORENE [106] or RNS [160]. A piecewise polytropic representation of the BOB, V18, N93, UIX and DBHF EOSs has also been determined (see Appendix B for a discussion on the different EOS formats).

3.2 Global properties and universal relations

The set of EOSs presented in Sec. 3.1 has been employed in order to model both non-rotating and uniformly rotating NSs; in addition to mass and radius, a number of other global properties has been calculated and the relations between the calculated variables have been investigated.

The *tidal deformability* [161, 162] $\lambda \equiv Q_{\rm ij}/E_{\rm ij}$, which describes the variation of the quadrupole moment $Q_{\rm ij}$ linearly induced when a weak external gravitational field $E_{\rm ij}$ is applied, is a very important quantity which has already been proven to be constrained by GW observations [163, 164]. The tidal deformability, which can also be expressed in terms of the Love number k_2 [161, 165] can be calculated according to

$$k_2 = \frac{3}{2}\frac{\lambda}{R^5} = \frac{3}{2}\beta^5\Lambda = \\ = \frac{8}{5}\frac{\beta^5 z}{6\beta(2-y_R)+6\beta^2(5y_R-8)+4\beta^3(13-11y_R)+4\beta^4(3y_R-2)+8\beta^5(1+y_R)+3z\ln(1-2\beta)}\,, \tag{3.1}$$

where geometrized units, $G = c = 1$, have been used; moreover, in the notation used, $\beta = M/R$ is the compactness parameter, the parameter z is defined according to

$$z \equiv (1-2\beta^2)[2-y_R+2\beta(y_R-1)]\,, \tag{3.2}$$

and the parameter y, appearing in the previous equations as evaluated at the star radius R and labeled as $y_{\rm R}$, depends on the radius r and is determined by solving, together with the TOV Eqs. (2.1),(2.2), the following differential equation [165]

$$\frac{dy}{dr} = -\frac{y^2}{r} - \frac{y-6}{r-2m} - rA\,, \tag{3.3}$$

with

$$A \equiv 4\pi \frac{(5-y)\rho + (9+y)p + (\rho+p)/c_s^2}{1-2m/r} - \left[\frac{2(m+4\pi r^3 p)}{r(r-2m)}\right]^2 , \tag{3.4}$$

and c_s^2 representative of the squared sound speed. In general, for a binary system with masses M_1 and M_2 and mass ratio $q = M_1/M_2$, the chirp mass can be calculated according to [166]

$$M_c = (M_1 M_2)^{3/5}/(M_1+M_2)^{1/5} , \tag{3.5}$$

together with an effective tidal deformability given by

$$\bar{\Lambda} = \frac{16}{13}\frac{(1+12q)\Lambda_1 + (q+12)\Lambda_2}{(1+q)^5} . \tag{3.6}$$

Both these parameters have been constrained by the GW170817 event [163], resulting in $M_c = 1.188^{+0.004}_{-0.002} M_\odot$, corresponding to $M = 1.365 M_\odot$ in the case of a symmetric event and $M_1 = 1.64 M_\odot, M_2 = 1.15 M_\odot$ in the case of maximum asymmetry $q = 0.7$, and $\bar{\Lambda} < 800$, later updated to $70 < \bar{\Lambda} < 720$ in Ref. [167].

The set of equations can be further extended in order to compute another NS global quantity, namely the moment of inertia $I = J/\Omega$, where J and Ω respectively represent the angular momentum and the angular frequency. In particular, the dimensionless quantity

$$\frac{I}{MR^2} = \frac{1}{2\beta}\frac{w_R}{3+w_R} , \tag{3.7}$$

is calculated, where, analogously to Eq. (3.3), the parameter w is determined by solving the following differential equation

$$\frac{dw}{dr} = \frac{4\pi r(\epsilon+p)(4+w)}{1-2m/r} - \frac{w(3+w)}{r} , \tag{3.8}$$

with w_R being the value of w evaluated at the star radius R.

The solution of the TOV equations, together with Eqs. (3.3) and (3.7), makes it possible to determine the global NS properties. Since our set of EOSs accounts only for the core part, a crust is properly attached to each EOS; in particular, Refs. [170, 171] are considered in order to model the outer crust, while the EOS of Ref. [172] is adopted for the inner crust.

Table 3.1 Properties of NSs listed according to the considered EOSs: maximum mass $M_{\rm TOV}$ and related radius $R_{\rm M_{TOV}}$, radius $R_{1.4}$ and tidal deformability $\Lambda_{1.4}$ of the $M = 1.4\ M_\odot$ configuration, and type of EOS.

EOS	$M_{\rm TOV}$	$R_{\rm M_{TOV}}$ [km]	$R_{1.4}$ [km]	$\Lambda_{1.4}$	Type	Ref.
BOB	2.51	11.32	12.85	584	nucleonic	[168]
BOB+DS1	2.30	12.13	12.85	584	hybrid	[150]
BOB+DS2	2.02	11.95	12.85	584	hybrid	[150]
BOB+DS3	1.79	11.72	12.75	539	hybrid	[150]
BOB+DS4	1.60	11.38	12.12	346	hybrid	[150]
V18	2.34	10.63	12.33	419	nucleonic	[168]
V18+DS1	2.16	11.34	12.33	419	hybrid	[150]
V18+DS2	1.93	11.15	12.33	419	hybrid	[150]
V18+DS3	1.75	10.95	11.96	320	hybrid	[150]
V18+DS4	1.61	10.74	11.36	215	hybrid	[150]
N93	2.13	10.49	12.68	474	nucleonic	[168]
N93+DS1	2.00	11.17	12.68	474	hybrid	[150]
N93+DS2	1.80	10.76	12.64	459	hybrid	[150]
N93+DS3	1.67	10.48	11.76	250	hybrid	[150]
N93+DS4	1.58	10.31	11.05	162	hybrid	[150]
UIX	2.04	10.02	12.03	340	nucleonic	[168]
UIX+DS1	1.98	10.59	12.03	340	hybrid	[150]
UIX+DS2	1.82	10.63	12.03	340	hybrid	[150]
UIX+DS3	1.69	10.44	11.81	10	hybrid	[150]
UIX+DS4	1.59	10.30	11.22	6	hybrid	[150]
APR	2.20	9.92	11.59	274	nucleonic	[73]
DBHF	2.31	11.29	13.10	681	nucleonic	[169]
LS220	2.04	10.67	12.94	542	nucleonic	[76]
SFHO	2.06	10.31	11.93	334	nucleonic	[18]
V18(N+Y)	1.65	9.00	11.92	302	hyperonic	[143]
BOB(N+Y)	1.37	11.07	–	–	hyperonic	[150]

Tab. 3.1 includes important NS properties for the set of EOSs discussed in Sec. 3.1; in particular, the maximum mass $M_{\rm TOV}$ and the related radius $R_{\rm M_{TOV}}$ are reported, as well as the radius and the tidal deformability of the $M = 1.4\ M_\odot$ configuration, respectively labeled as $R_{1.4}$ and $\Lambda_{1.4}$. The EOSs used for hybrid stars are reported in the table with the nomenclature DSα, where α ranges from 1 to 4; increasing the value of α leads to higher quark matter fractions which, in turn, lead to decreasing maximum masses and related radii. Therefore, for the following studies, only configurations with maximum masses higher than $2.0 M_\odot$ will be considered, namely BOB+DS1, BOB+DS2, V18+DS1, N93+DS1.

These equations of state have been considered in order to investigate a number of universal relations which link the global properties and can be used in order to constrain parameters otherwise difficult to detect; hence, in the following paragraphs, the discussion on global properties will be further extended and the universal relations between them will be described in detail.

3.2.1 The moment of inertia I

The importance of a universal relation involving the NS moment of inertia, mass and radius lies in the fact that, if the mass and the moment of inertia are known, the radius can be also constrained [173, 174]. Indeed, since the moment of inertia is proportional to the squared radius, a measurement of the former variable with a certain accuracy determines approximately twice such accuracy for the radius.

When normalized with respect to M^3, the following fit relation is determined [23]:

$$\frac{I}{M^3} \equiv 1.0334\, M^{-1} + 30.7271\, M^{-2} - 12.8839\, M^{-3} + 2.8841\, M^{-4}\,, \tag{3.9}$$

which can be compared with the following fit relation shown in [175]:

$$\frac{I}{M^3} \equiv 0.8134\, \beta^{-1} + 0.2101\, \beta^{-2} + 0.003175\, \beta^{-3} - 0.0002717\, \beta^{-4}\,. \tag{3.10}$$

The differently normalized moment of inertia I/MR^2, is instead related to the mass according to the following simple linear relation:

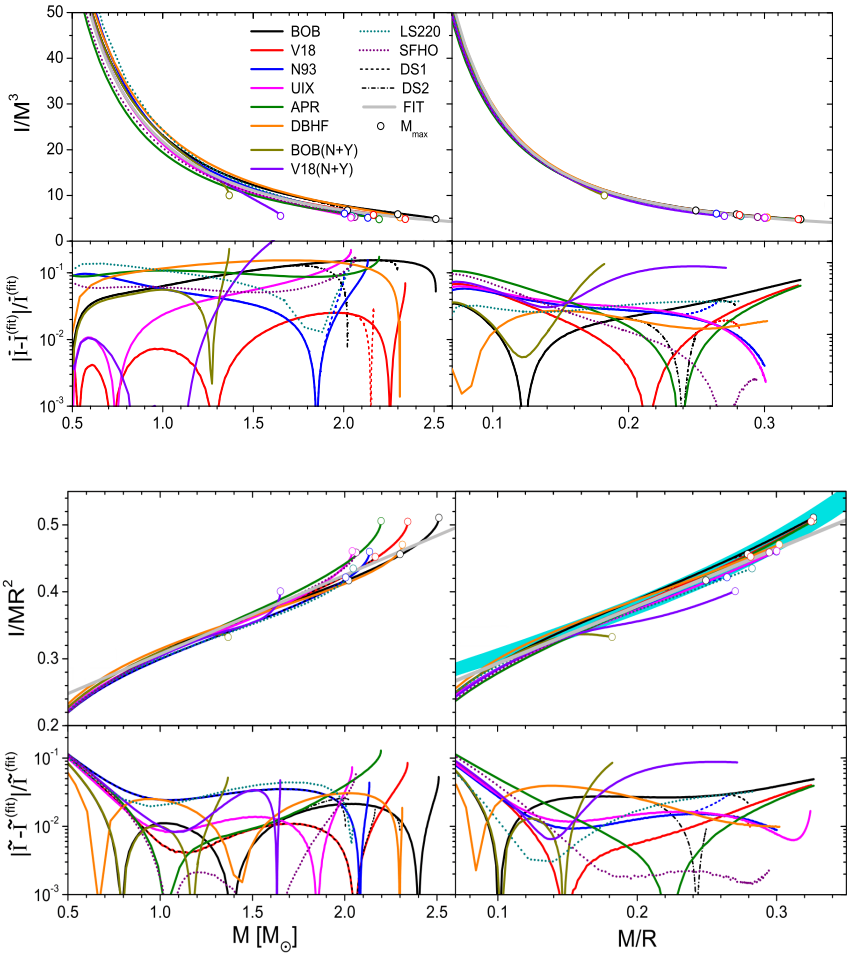

Figure 3.2 I/M^3 (upper panels) and I/MR^2 (lower panels) vs. M (left panels) and M/R (right panels) for the set of EOSs included in Fig. 3.1. The fit relations (3.9), (3.10), (3.11), (3.12) are represented as grey lines in the plots, and the absolute fractional errors with respect to the latter relations are included below every panel. The fit relation (3.13) is displayed as a blue band, and the maximum mass configurations, labeled as $M_{\rm max}$, are reported with a marker.

$$\frac{I}{MR^2} \approx 0.189 + 0.118\frac{M}{M_\odot} \pm 0.016\,, \tag{3.11}$$

while the equivalent fit for I/MR^2 vs. M/R reads

$$\frac{I}{MR^2} \equiv 0.207 + 0.857\beta \pm 0.011\,, \tag{3.12}$$

and can be compared with the following fit relation included in Refs. [176, 177], shown in

Fig. 3.2 as a blue band

$$\frac{I}{MR^2} \approx (0.237 \pm 0.008)(1 + 2.844\beta + 18.91\beta^4)\,. \tag{3.13}$$

As already mentioned before, the measurement of M and I allows to constrain R with good accuracy; indeed, it follows from Eq. (3.11) that

$$\delta(f \equiv \frac{I}{MR^2}) = -\frac{2I}{MR^3}\delta R = -2f\frac{\delta R}{R}\,. \tag{3.14}$$

which, in turn, leads to

$$\frac{\delta R}{R} = \frac{1}{2}\frac{\delta f}{f} \approx \frac{0.016}{0.4} < 4\%\,. \tag{3.15}$$

The fractional errors shown in Fig. 3.2 indicate that the examined EOSs are in good agreement with the universal relations, with maximum deviations of the order of a few percent, being largest in the case I/M^3 vs. M and for hyperonic EOSs. It is also interesting to notice that the fit I/MR^2 vs. M fails mainly for large masses $M > 2M_\odot$, and the fit vs. β fails for hyperonic stars with low maximum masses. The latter feature may be explained in terms of the small radius of the maximum mass configuration for the hyperonic EOSs which leads to large values of $\beta = M/R$ close to the maximum mass configuration. The deviation of hyperonic EOSs from universality can be potentially used in order to infer the hyperonic presence in NSs, which would be possible with a future simultaneous measurement of M, R, I, at least close to the maximum mass configuration.

3.2.2 The tidal deformability Λ

The tidal deformability parameter Λ of a single NS is the second global observable deserving particular attention. The correlations between Λ, M and R are represented, for the entire set of EOSs, in Fig. 3.3; in particular, the information on the radius R is encoded in the differently colored segments of the curves. The shaded area, $400 < \Lambda < 800$, represents the region constrained by the interpretation of the GW170817 event as a symmetric event[163,

164][1], where the deduction follows from a multimessenger analysis of the former event, considering tidal effects during the binary inspiral and combining with an analysis of the electromagnetic counterpart with kilonova models. Vertical dashed lines are present in the figure, corresponding to $M = 1.365M_{\odot}$ and $M = 1.5M_{\odot}$, respectively indicating the NS mass in the symmetric case for GW170817, and the constraint derived in [158].

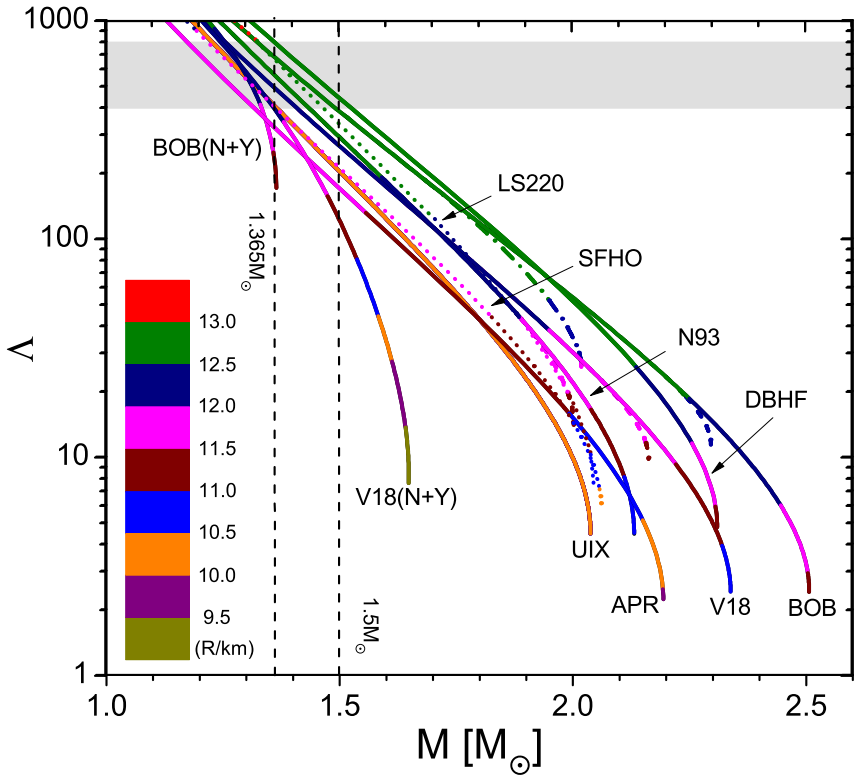

Figure 3.3 Λ vs M curves for the different EOSs; a colorscale is included in order to characterize different radii for the considered configurations. Dashed and dot-dashed curves display DS1 and DS2 hybrid stars, respectively. The shaded area is constrained by the interpretation of the GW170817 event as a symmetric event, according to Ref. [163, 164].

It follows from Fig. 3.3 that , for $M = 1.365M_{\odot}$ and within the Λ constrained region, a radius interval 12 km $<$ R $<$ 13 km is found for the compatible EOSs V18, N93, UIX, BOB,

[1]It is important to remark that these constrains have been later updated (see e.g. Ref. [167]); in the work presented here, however, the original upper and lower limits have been considered.

DBHF, V18(N+Y) and the phenomenological LS220. All the EOSs constructed with the DS approach also fulfill the constraint, since for the considered mass $M = 1.365 M_{\odot}$ there still is no quark matter part; APR, BOB(N+Y) and LS220, instead, do not fulfill the $\Lambda > 400$ constraint.

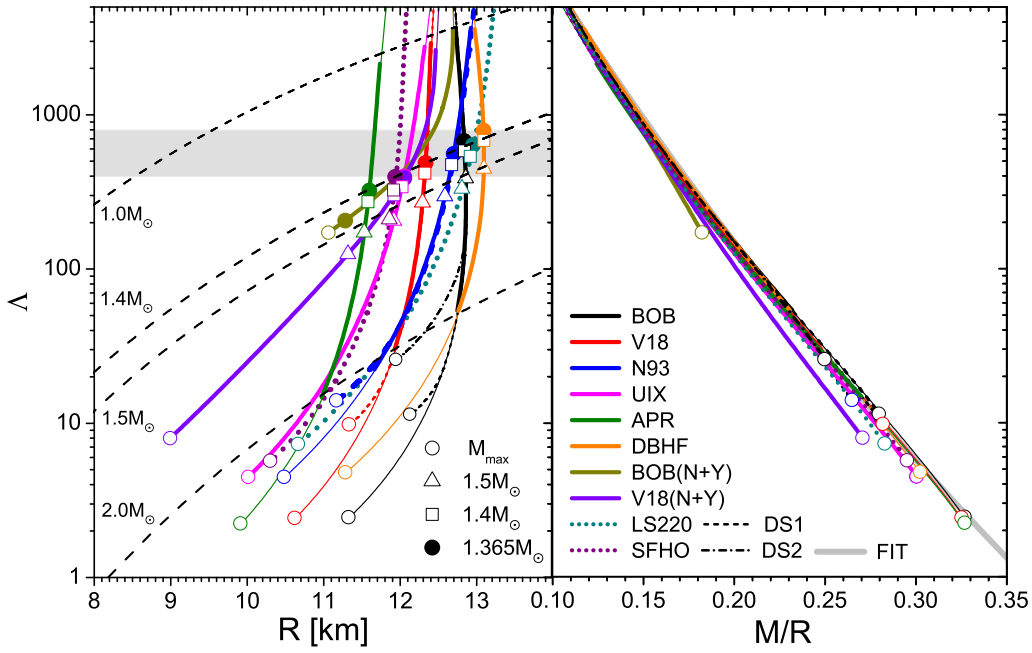

Figure 3.4 Left panel: Λ vs R curves for the different EOSs; the mass information of notable configurations is encoded in the open symbols for each EOS. The shaded area is constrained by the interpretation of the GW170817 event as a symmetric event. Right panel: Λ vs M/R; the grey curve is representative of the fitting equation 3.16.

Fig. 3.4 (left panel) further specifies this by displaying the Λ curves with respect to R; in such a plot, full circles, squares and triangles respectively represent $M = 1.365,\ 1.4,\ 1.5\ M_{\odot}$, while open circles are instead representative of the maximum mass (here labeled $M_{\max}$) for every EOS. It is once again possible to investigate the universal relations that involve Λ: in this context, Fig. 3.4 shows the correlation between Λ and the compactness parameter β (right panel). In particular, the grey curve represents the following fit proposed in Ref. [178]

and shown to hold within 6.5% for a large set of NS EOSs:

$$\beta = 0.36 - 0.0355 \ln \Lambda + 0.000705 (\ln \Lambda)^2 \,. \tag{3.16}$$

The set of EOSs is in good agreement with the fitting relation, with maximum deviations of the order of a few percent, being highest for the hyperonic EOSs.

A second universal relation involves both the tidal deformability and the moment of inertia according to the following equation [178]:

$$\ln\left(I/M^3\right) = 1.496 + 0.05951 \ln \Lambda + 0.02238 (\ln \Lambda)^2 - 6.953 \times 10^{-4} (\ln \Lambda)^3 + 8.345 \times 10^{-6} (\ln \Lambda)^4 \,. \tag{3.17}$$

The former, represented in Fig. 3.5 and extensively discussed in the next paragraph, identifies the first of the relations involving the *I-Love-Q* trio, namely the moment of inertia I, the tidal love number, represented by Λ in the equations, and the quadrupole moment Q.

3.2.3 The quadrupole moment Q

The moment of inertia I is also involved in an EOS-independent relation with a further quantity, namely the spin-induced quadrupole moment Q, as shown in Refs. [178, 179]. The validity has been first suggested in the limit of slow rotation, but has been later extended (see, e.g., Ref. [180]) to high rotational frequencies.

In order to calculate Q and test the universal relation with the set of EOSs presented here, the RNS code [160] has been used. RNS is able to calculate axisymmetric rigidly rotating NS models, with the space-time metric being expressed as (see, e.g., Ref. [181])

$$ds^2 = -e^{\gamma+\rho} dt^2 + e^{2\beta}(dr^2 + r^2 d\theta^2) + e^{\gamma-\rho} r^2 \sin^2\theta (d\phi - \omega dt)^2 \,, \tag{3.18}$$

where γ, ρ, β and ω are functions of the radial coordinate$r$ and the polar angle θ.

It has been shown [182] that the quadrupole moment calculated by RNS does not correspond to the quadrupole moment of the rotating source according to the Geroch-Hansen

multipole moments [183–186]. Therefore, the quadrupole moment $Q^{\rm RNS}$ calculated by RNS, is corrected according to [183]:

$$Q = Q^{\rm RNS} - \frac{4}{3}\left(\frac{1}{4} + b_0\right) M^3 \,, \tag{3.19}$$

with M being the mass of the star; the parameter b_0 is calculated according to

$$b_0 - \frac{16\sqrt{2\pi} r_{\rm eq}^4}{M^2} \int_0^{\frac{1}{2}} \frac{s^3 ds}{(1-s)^5} \int_0^1 d\mu \sqrt{1-\mu^2}\, P(s,\mu) e^{\gamma+2\beta} T_0^{\frac{1}{2}}(\mu) \,, \tag{3.20}$$

where $r_{\rm eq}$ identifies the value of the coordinate radius at the equator, $s = r/(r+r_{\rm eq})$ represents a compacted radial coordinate, $\mu = \cos(\theta)$, $P(s,\mu)$ is the pressure, and $T_0^{\frac{1}{2}}(\mu) = \sqrt{2/\pi} C_0(\mu)$ with C_0 being the 0th-order Gegenbauer polynomial.

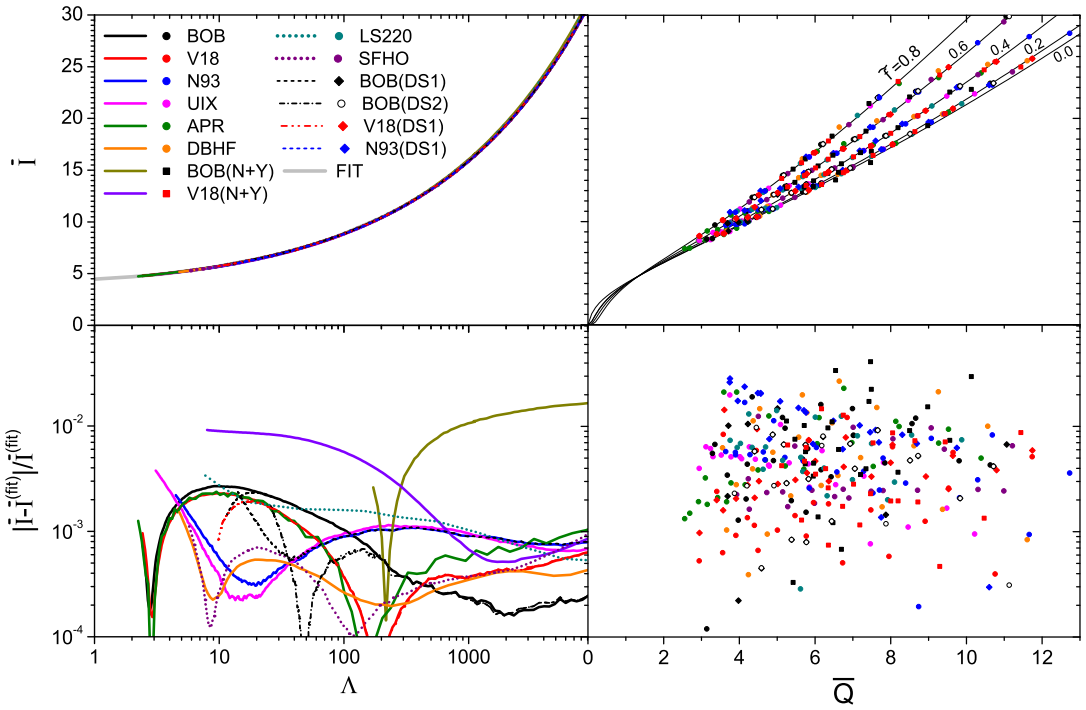

Figure 3.5 Left panel: $\bar{I} = I/M^3$ vs Λ for the different EOSs; the grey line represents eq. 3.17. Right panel: $\bar{I}$ vs $\bar{Q} = -QM/(I\Omega)^2$ for different values of the normalized frequency $\tilde{f} \equiv 20Rf = 0.0, 0.2, 0.4, 0.6, 0.8$. Absolute fractional errors are represented in the lower panels.

The normalized quadrupole moment $\bar{Q}$ and moment of inertia $\bar{I}$, respectively defined as

$$\bar{Q} \equiv -\frac{QM}{(I\Omega)^2} \,, \quad \bar{I} \equiv \frac{I}{M^3} \,, \tag{3.21}$$

are correlated via [180]

$$\ln \bar{I} \approx \sum_{i,j=0,4} \mathcal{A}_{ij} a^i (\ln \bar{Q})^j \approx \sum_{i,j=0,4} \mathcal{B}_{ij} \tilde{f}^i (\ln \bar{Q})^j \,, \tag{3.22}$$

where the constants $\mathcal{A}_{ij}$ and $\mathcal{B}_{ij}$ are included in Ref. [180]. The fitting equation can be expressed both in terms of the parameter $a \equiv I\Omega/M^2$ and the normalized frequency $\tilde{f} \equiv 20Rf$[2]; in particular, the second expression is chosen in order to represent the universal relation for the set of EOSs analyzed here. It is important to point out that the relation initially reported in [178, 179], namely

$$\ln \bar{I} = 1.393 + 0.5471 \ln \bar{Q} + 0.03028 (\ln \bar{Q})^2 + 0.01926 (\ln \bar{Q})^3 + 4.434 \times 10^{-4} (\ln \bar{Q})^4 \,, \tag{3.23}$$

is referred to the slow rotation case, i.e. the limit $\tilde{f} \approx 0.0$.

It can be concluded that the set of EOSs presented here agrees very well with the universal relations represented in Fig. 3.5, with maximum fractional errors of the order of 3% and reached, as usual, in the case of hyperonic EOSs.

Overall, the study presented in this Chapter confirms then that the EOSs derived in the context of the BHF framework, in particular V18, N93, BOB and UIX effectively fulfill a number of universal relations and do not violate the constraints imposed by the GW170817 event; these equations of state will be further investigated in the next chapters, focusing in particular on their application in numerical simulations.

[2]The normalization is such that $f = 1kHz$ corresponds to $\tilde{f} \approx 1$ for $R = 15$ km.

CHAPTER 4

FINITE TEMPERATURE MICROSCOPIC EOSS

4.1 Extension to finite temperature in the BHF framework

The EOS set presented and discussed in Chapter 3 and studied in Ref. [23] is characterized by the fact that all the EOSs are constructed (or sampled, as in the case of LS220 and SFHo) at zero temperature. The latter is a condition which well approximates the condition of a single long-lived neutron star, but fails for the cases where temperature effects are important, such as binary neutron star mergers or the modeling of protoneutron stars [187] and supernovae [188]. Finite temperature EOSs are then necessary in order to correctly account for temperature effects in numerical codes, but such currently available EOSs are effectively restricted to a handful [16–20, 22].

An important part of this work is devoted to the extension at finite temperature of the EOSs derived in the context of the BHF framework, in particular V18, N93, BOB and UIX; this operation is made possible by employing the BHF approach for asymmetric nuclear matter at finite temperature [66, 189–196], whose essential aspects will be discussed below.

The primary ingredient of the approach is represented by the interaction matrix K, which satisfies the self-consistent equations:

$$K(n_B, x_p; E) = V + V \ \mathrm{Re} \sum_{1,2} \frac{|12\rangle \, (1-n_1)(1-n_2) \, \langle 12|}{E - e_1 - e_2 + i0} K(n_B, x_p; E), \tag{4.1}$$

and

$$U_1(n_B, x_p) = \mathrm{Re} \sum_{2} n_2 \, \langle 12|K(n_B, x_p; e_1 + e_2)|12\rangle_a \ , \tag{4.2}$$

where n_B represents the baryon number density and x_p identifies the proton fraction, i.e. $x_p = \rho_p/\rho$ with ρ_p and ρ representing the proton and the total baryon density respectively. The parameter E identifies the starting energy and $e(k) \equiv k^2/2m + U(k)$ is the single-particle energy. The multi-indices $1, 2$ denote in general momentum, isospin, and spin.

The extension at finite temperature of the considered EOSs is carried out using the so-called *frozen correlations* approximation [189–191, 193, 194], where the single-particle potentials $U_{n,p}(k)$ are approximated by the ones calculated at $T = 0$. Within this approximation, the nucleonic free energy density has the following simplified expression,

$$f_N = \sum_{i=n,p} \left[2 \sum_k n_i(k) \left(\frac{k^2}{2m_i} + \frac{1}{2} U_i(k) \right) - T s_i \right], \tag{4.3}$$

where $n_i(k)$ is a Fermi distribution, and the entropy density s_i for the component i is represented by

$$s_i = -2 \sum_k \{ n_i(k) \ln n_i(k) + [1 - n_i(k)] \ln [1 - n_i(k)] \} \, . \tag{4.4}$$

The total free energy $f = f_\mathrm{N} + f_\mathrm{L}$, which also includes the leptonic contribution f_L, represents the starting point in order to calculate all the relevant observables in a thermodynamically consistent way. As a first step, the chemical potentials are defined as

$$\mu_i = \frac{\partial f}{\partial n_i} \, , \tag{4.5}$$

which, in turn, allow to calculate the pressure and the specific internal energy according to

$$p = n_B^2 \frac{\partial (f/n_B)}{\partial n_B} = \sum_i \mu_i n_i - f \, , \tag{4.6}$$

$$\epsilon = \frac{f + Ts}{\rho} \, , \quad s = -\frac{\partial f}{\partial T} \, , \tag{4.7}$$

so that the total energy density $e \equiv \rho(1+\epsilon)$.

Numerical parametrizations for the free energy density of symmetric nuclear matter (SNM) and pure neutron matter (PNM) have been determined in Ref. [21] and have the following expression

$$\frac{F}{A}(\rho, T) = a\rho + b\rho^c + d\tilde{a}t^2\rho + \tilde{b}t^2 ln(\rho) + (\tilde{c}t^2 + \tilde{d}t^{\tilde{e}})/\rho\,, \tag{4.8}$$

where the complete table of the coefficients is reported in Ref. [21] and the parametrization $t = T/(100\text{ MeV})$ has been used.

The asymmetric nuclear matter case can be described in terms of a parabolic approximation for x_p [192, 197–199],

$$f(n_B, T, x_p) \approx f_{\rm SNM}(n_B, T) + (1-2x_p)^2[f_{\rm PNM}(n_B, T) - f_{\rm SNM}(n_B, T)], \tag{4.9}$$

so that it is possible to determine the complete EOS tables in the parameter space of temperature, density and proton fraction with the only need of the SNM and PNM parametrizations. Such tables are a necessary input in order to perform binary neutron star merger simulations with a fully consistent temperature treatment, although it is also possible to just determine a zero temperature beta-equilibrated cut in order to perform simulations in the *hybrid EOS* regime (see Chapter 5).

4.2 Features and results

In order to fully understand the merger simulations, the determination and discussion of the features characterizing the finite temperature EOSs is of great importance. The first step is of course represented by the solution of the TOV equations in order to construct stable neutron star models; in this context, the EOSs are supplied with a part accounting for the low density region constituting the crust, and in particular the EOSs of Refs. [170, 171] are considered for the outer crust and the EOS of Ref. [172] for the inner crust.

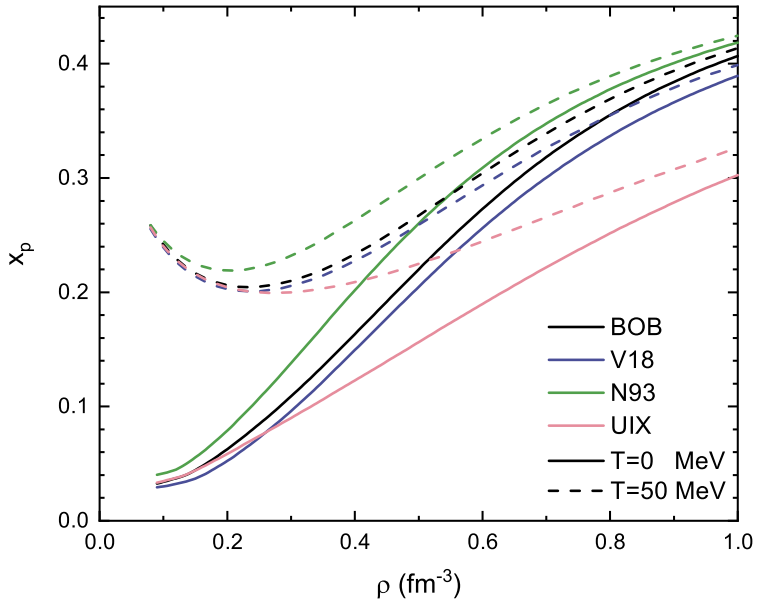

Figure 4.1 Proton fractions in beta-equilibrated matter for the different EOSs at the temperatures T = 0 and 50 MeV and at different baryon number densities ρ, represented with solid and dashed lines respectively.

The characteristics of such modeled neutron stars can be now investigated focusing on different temperatures; in particular, it is important to focus first on the structure and the composition of the stellar matter; in this regard, Fig. 4.1 displays the composition of matter, in terms of the proton fraction $x_{\rm p}$ at different baryon number densities and temperatures for the considered EOSs, under the assumption of beta-equilibrium. Interestingly, the temperature increase mainly affects the proton fraction in the low density region, where leptons become numerous as a result of Fermi distributions at finite temperature. As a consequence of the charge-neutrality condition, this leads to an increase of the proton fraction and the isospin symmetry of nuclear matter, counteracting the stiffening of the EOS due to the individual thermal pressures of the nucleons. The increase of the lepton densities with temperature enhances the thermal lepton pressure, which acts against the effect of increasing isospin symmetry.

In the discussion of temperature effects in the NS global properties, the characterization

of the behaviour of the total mass as a function of temperature is particularly important. Fig. 4.2 represents, for the different EOSs, the gravitational mass $M_{\rm G}$ as a function of the central baryon number density $\rho_{\rm c}$ for different temperatures.

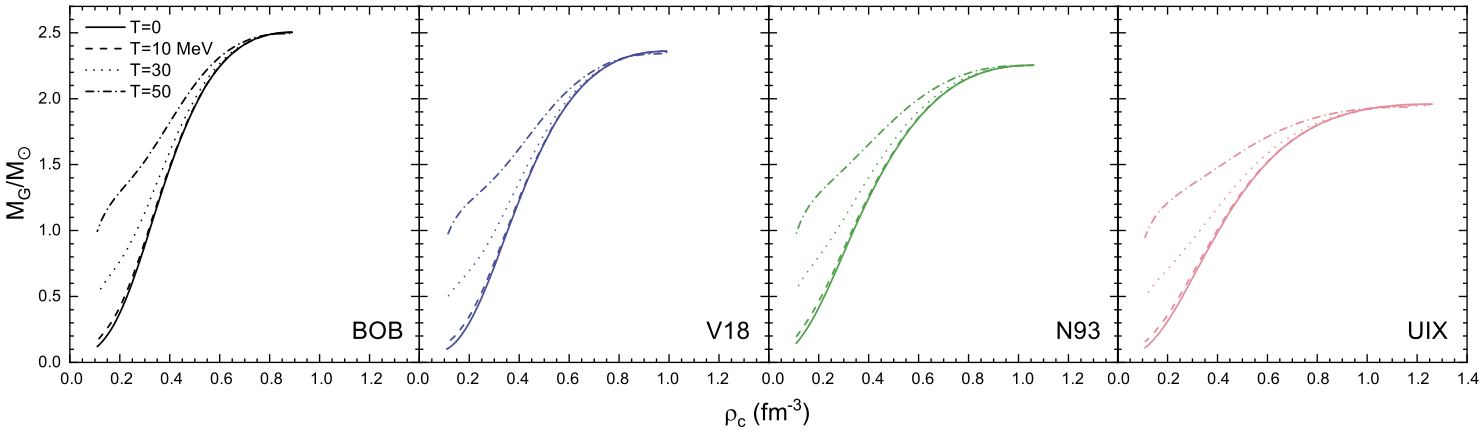

Figure 4.2 Gravitational masses vs. central baryon number densities for the different EOSs. Isothermal, beta-stable models are considered with $T = 0, 10, 30, 50$ MeV.

The maximum masses for the EOSs analyzed here, i.e. $2.50, 2.36, 2.25$ and $1.96 M_{\odot}$ for BOB, V18, N93 and UIX respectively, do not greatly change with increasing temperature, decreasing of a maximum of 1% at $T = 50$ MeV for UIX; the temperature increase has instead a greater impact for lower central densities i.e. about $\rho < 0.8$ fm^{-3}, leading to a systematic enhancement of the gravitational mass. The decrease of the maximum mass can be also investigated by considering the maximum baryon mass as a function of temperature; in this regard, Fig. 4.3 reports the variation of the maximum gravitational and baryon masses with respect to temperature. The comparison clearly shows a more pronounced decrease for the maximum baryon mass, which reaches a maximum of 6% for the UIX EOS. This analysis is similar to the one reported in Ref. [200], where the maximum baryon mass decrease has been reported also for a number of other finite temperature EOSs; on the other hand, in the same reference, the maximum gravitational mass was reported to increase with temperature, thus underlining a different behaviour for the EOSs presented here. An explanation for this difference could be related to the fact that, for the EOSs presented here, thermal effects are

contained in the whole interaction part through the single-particle potentials, while in Ref. [200] interactions are mostly local with a non-local correction, and therefore thermal effects are included only in the kinetic energy.

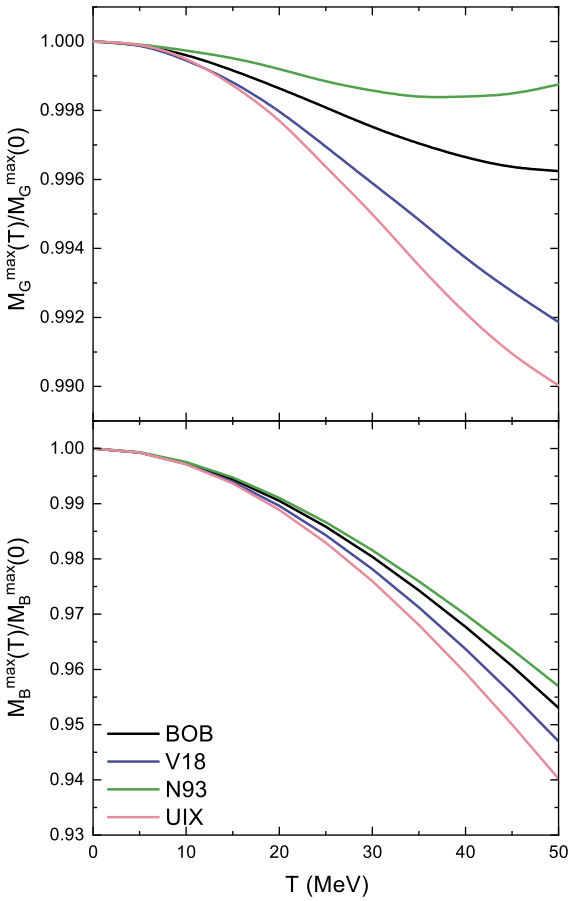

Figure 4.3 Maximum gravitational masses (upper panel) and maximum baryon masses (lower panel) vs. temperatures for the different EOSs.

In order to better understand the thermal properties of the set of EOSs, a necessary assessment involves characterizing the thermal pressure $p_{\rm th}(T,\rho) \equiv p(T,\rho) - p(0,\rho)$ and internal energy density $\epsilon_{\rm th}(T,\rho) \equiv \epsilon(T,\rho) - \epsilon(0,\rho)$ for each case. Such an investigation is reported in Fig. 4.4, where p and ϵ are reported for all the considered EOSs at $T = 0$ (upper panel), together with their changes at $T = 50$ MeV (lower panel).

Interestingly, the thermal pressure behavior is the result of the delicate interplay of three

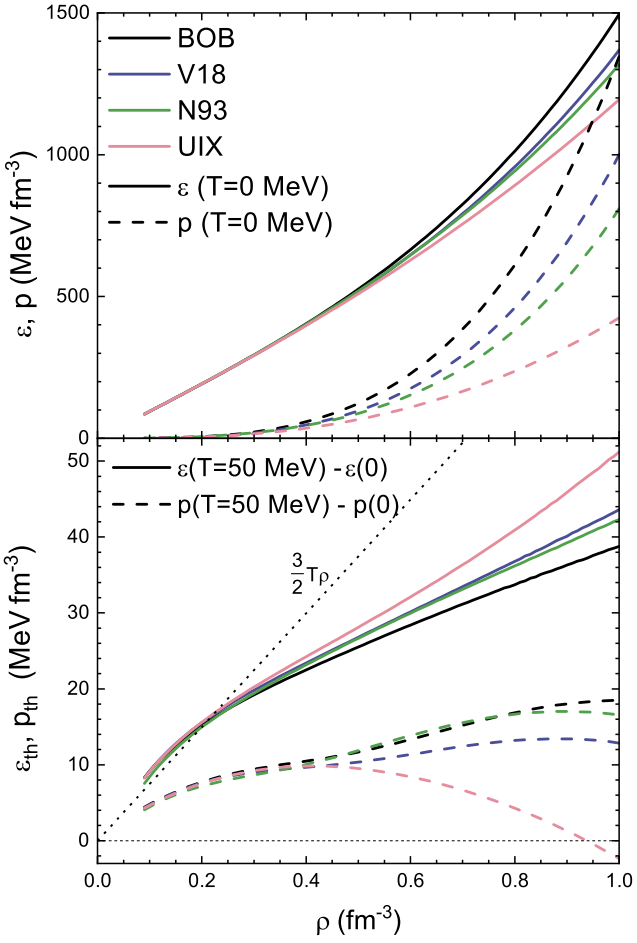

Figure 4.4 Internal energy density ϵ and pressure p of beta-stable matter vs. baryon number density at $T = 0$ (upper panel) and differences of the same quantities at $T = 50$ MeV, with respect to $T = 0$, for the different EOSs (lower panel).

competing effects: the individual thermal pressures of protons and neutrons at fixed densities increase with temperature, while the isospin asymmetry decreases, thus reducing the total baryonic pressure. Finally, the lepton thermal pressure also contributes, increasing with both density and temperature. As shown in the lower panel of Fig. 4.4, the overall thermal effects, for the EOSs here considered, are small and a simple nonrelativistic ideal-gas approximation for nucleons, i.e. $\epsilon_{\rm th} = \frac{3}{2}T\rho$, displayed in the lower panel of Fig. 4.4 as a dotted line, overestimates the thermal effects; this result was shown to be independent with respect to the frozen correlations approximation in Ref. [192].

The evaluation of $p_{\rm th}$ and $\epsilon_{\rm th}$ is particularly important, since the combination of these factors yields the adiabatic index $\Gamma_{\rm th}$ in the ideal fluid approximation:

$$\Gamma_{\rm th} = 1 + \frac{p_{\rm th}}{\epsilon_{\rm th}} \tag{4.10}$$

Such a quantity is of great importance in binary neutron star merger simulations, see Sec. 5.2, and of course can be directly evaluated only in finite temperature EOSs. Therefore, following Ref. [201], where $\Gamma_{\rm th}$ has been evaluated for 2 EOSs, namely the models presented in Refs. [76, 77] under the assumption of beta-equilibrium, the same operation is carried out for the set of finite temperature EOSs presented here.

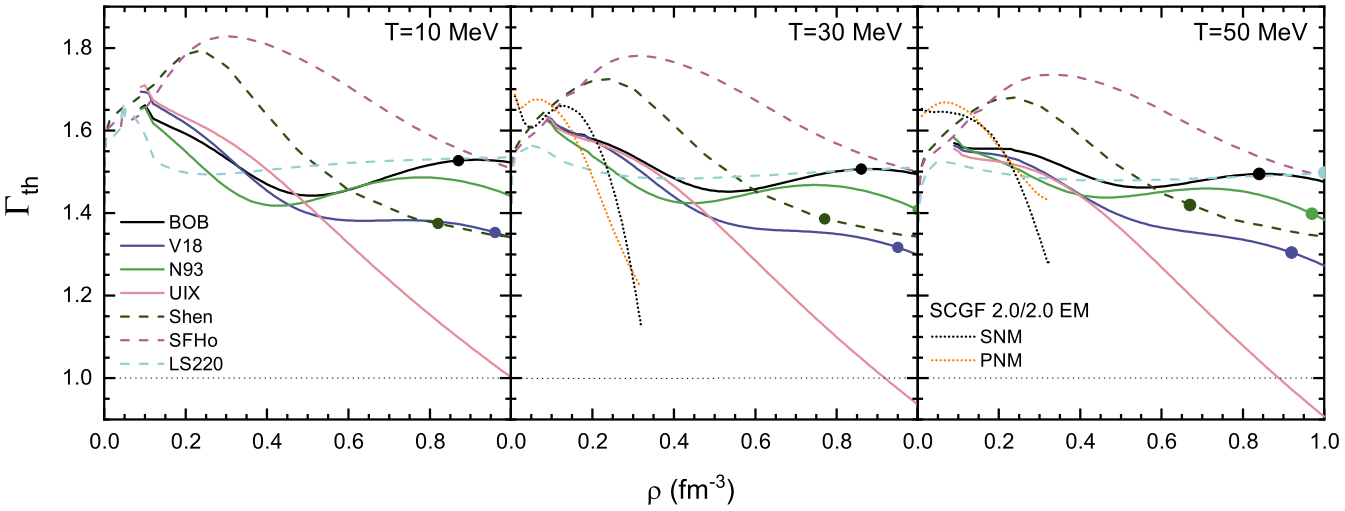

Figure 4.5 $\Gamma_{\rm th}$ vs. baryon number density for beta-stable matter at $T = 10, 30, 50$ MeV. The SNM and PNM results (no leptons) of Ref. [202] are also displayed, with dotted curves, for comparison.

Fig. 4.5 represents $\Gamma_{\rm th}$ as a function of the baryon number density ρ, for the BOB, N93, V18 and UIX EOSs, together with the LS220 [76] , Shen [77] and SFHo [18] EOSs, which represent some of the most common choices adopted in merger simulations; results of Ref. [202] for SNM and PNM (no lepton contributions), shown as dotted curves in the figure, are limited to $\rho < 0.3$ fm $^{-3}$, at which point the accuracy estimates of that approach become prohibitively large. While the temperature dependence is not greatly pronounced,

the density dependence turns out to be very important. In particular, the figure shows that the Shen and SFHo EOS predict higher values than the other EOSs in the medium-density regime.

Since the $\Gamma_{\rm th}$ parameter determined here is evaluated in the beta-stable situation only and at fixed temperatures, the calculations previously reported have only limited validity. A possible way to investigate the values in $\Gamma_{\rm th}$, and also determine a representative value to use in simulations, is made possible by measuring the parameter in simulations carried out using finite temperature tabulated EOSs; the next chapter will address this issue in detail.

CHAPTER 5

HYBRID EOS APPROACH IN BINARY NEUTRON STAR MERGER SIMULATIONS

5.1 Introduction

The majority of the available EOSs derived at zero temperature in the different approaches, both microscopic and phenomenological, together with polytropic and piecewise polytropic models, are suitable for simulations of single, isolated stars, but, as already anticipated in Chapter 4, a different approach has to be considered in binary neutron star merger simulations as finite temperature effects have to be taken into account. Indeed, during and after the merger event, shocks will locally increase the temperature of the object (see e.g. Ref. [203] for a recent discussion); in particular, from measurements in simulations employing finite-temperature EOSs, temperature is reported to grow to over 100 MeV using certain EOSs [204].

It is currently possible to account for finite temperature effects in simulations by employing one of the following two approaches:

- *Finite temperature EOS*: the use of a fully tabulated, finite temperature EOS, represents

the most consistent way to study systems featuring local temperature increases. As already mentioned before, such tables usually cover a parameter range $10^{-11} < n_{\rm B} <$ few fm^{-3}, $0 < T < 150$ MeV, and $0 < Y_{\rm e} < 0.6$ for baryon number densities, temperatures and electron fractions respectively [42, 43]. The main drawback of this method is represented by the scarcity of available constraint fulfilling EOSs, which, at the present time, do not effectively constitute a large set [16–20, 22]. During the simulation, a local temperature is obtained by inverting the $\epsilon(\rho, x_p, T)$ entries in the EOS table, using the values of the specific internal energy ϵ, restmass density ρ, and proton fraction x_p obtained through the solution of the hydrodynamics equations at a given timestep. This temperature is then used to obtain the total pressure $p(\rho, x_p, T)$ from the same EOS table.

- *Hybrid EOS approach*: often employed in neutron-star mergers simulations [9, 128, 201, 205–217], it is valid for physical systems for which the pressure and the specific internal energy can be expressed as the sum of a "cold" contribution, described by a polytropic or a tabulated EOS and of a "thermal" contribution obeying the ideal fluid EOS [92]. In this approach, the resulting pressure p and specific internal energy ϵ are respectively determined according to

$$p = p_c + \rho\epsilon_{\rm th}(\Gamma_{\rm th} - 1)\,, \tag{5.1}$$

$$\epsilon = \epsilon_c + \epsilon_{\rm th}\,, \tag{5.2}$$

where p_c and ϵ_c respectively identify the cold pressure and specific internal energy, both functions of the rest-mass density ρ. This approach was first used in order to study the collapse of a stellar core [205] and later applied to simulations of binary neutron stars [218].

The total specific internal energy ϵ is an evolved variable in numerical simulations, so it is possible to reconstruct $\epsilon_{\rm th}$ from Eq. (5.2) and substitute the latter in Eq. (5.1) in order to determine the total pressure. Given the great availability of zero-temperature EOSs, both in tabulated and polytropic formats, the main advantage of this method is represented by the possibility to easily employ any of these EOSs in numerical simulations. Of course, however,

this treatment lacks of accuracy and consistence: $\Gamma_{\rm th}$ is usually implemented in numerical codes as a constant, but the parameter non trivially depends on density, temperature, and proton fraction as already discussed in Section 4.2[1].

A first comparison between the two approaches has been carried out in Ref. [201], where two different finite temperature EOSs (LS and Shen), in the particular condition of beta equilibrium, have been considered. In conclusion, no particular value of $\Gamma_{\rm th}$, which is mathematically constrained to be $1.0 \leq \Gamma_{\rm th} \leq 2.0$, has been suggested, although values like 1.75 or 2.0 seemed to reproduce some of the features in finite temperature simulations accurately enough.

This chapter will cover an important step forward, i.e. the direct measurement of $\Gamma_{\rm th}$ in simulations with finite temperature EOSs which fulfill the current constraints on stellar matter, together with the comparison of both hydrodynamic and gravitational wave parameters with respect to simulations in the hybrid EOS approach in order to determine which $\Gamma_{\rm th}$ represents a suitable choice for the latter kind of simulations.

5.2 Physical models and numerical setup

In order to carry out meaningful comparisons between the two possible approaches, starting from the same initial conditions constitutes a necessary requirement for the study. For this purpose, after selecting a suitable EOS, the usual approach consists in creating a beta-stable and cold (zero-temperature) binary system with fixed separation between the two components, which can be then evolved with the two possible approaches.

The finite temperature EOSs employed for this study are represented by two public and constraint fulfilling EOSs: the recently derived V18 (see Chapter 4) and the commonly used SFHo EOS [18].

[1]Such results have limited validity as the investigation has been carried out under the assumption of beta equilibrated matter, and thus the proton fraction dependence hasn't been explored.

In order to be employed in numerical simulations, V18[2] is first converted in a format compatible with WhiskyTHC: this operation is performed by using the publicly available EOSmaker routines [220], which create a HDF5 version of the tabulated EOS also including the lepton contribution, which is added according to the Timmes EOS [221, 222]. Since the EOS derived in Ref. [21] only accounts for the range of densities of the core, a suitable crust (for $\rho < 10^{14}$ g/cm^3) is properly attached, at every temperature and proton fraction (see Appendix B for a complete description of the procedure); the H. Shen EOS [223] is used for the purpose[3].

The SFHo EOS [18] is based on the model of Hempel & Schaffner-Bielich (HS) [224] and Hempel et al. [19], which goes beyond the single-nucleus approximation used in phenomenological EOSs such as the LS[76] and Shen EOSs[77], and takes into account a statistical ensemble of nuclei and interacting nucleons. Nuclei are described as classical Maxwell-Boltzmann particles, and nucleons are treated within the relativistic mean field RMF model employing different parameterizations. In details, the SFHo EOS is implemented with a new RMF parameterization fitted to some neutron-star radius determinations, and the RMF parameters are varied to ensure that saturation properties of nuclear matter are correctly reproduced. In particular, the nuclear incompressibility $K = 245\,\mathrm{MeV}$ is compatible with the currently acceptable range of $240 \pm 20\,\mathrm{MeV}$ [225], which agrees with that predicted from the giant monopole resonances; the new parameterization also ensures that the symmetry energy at saturation density $J = 32.8\,\mathrm{MeV}$ is within the empirical range $28.5 - 34.9\,\mathrm{MeV}$ [42], and that the NS maximum mass $M_{\mathrm{TOV}} = 2.06 M_\odot$ is compatible with the currently strongest observational constraint $M > 2.14^{+0.10}_{-0.09} M_\odot$ [32].

A comparison of the properties of the considered EOS is included in Fig. 5.1: in particular, the left panel represents the pressure p and energy density e of betastable matter at $T = 0$

[2]The EOS, together with BOB, N93 and UIX is available for download [219].

[3]Furthermore, an artificial low-density background atmosphere, $\rho < 10^3$g/cm^3, evolved as discussed in [119], is used in all our simulations.

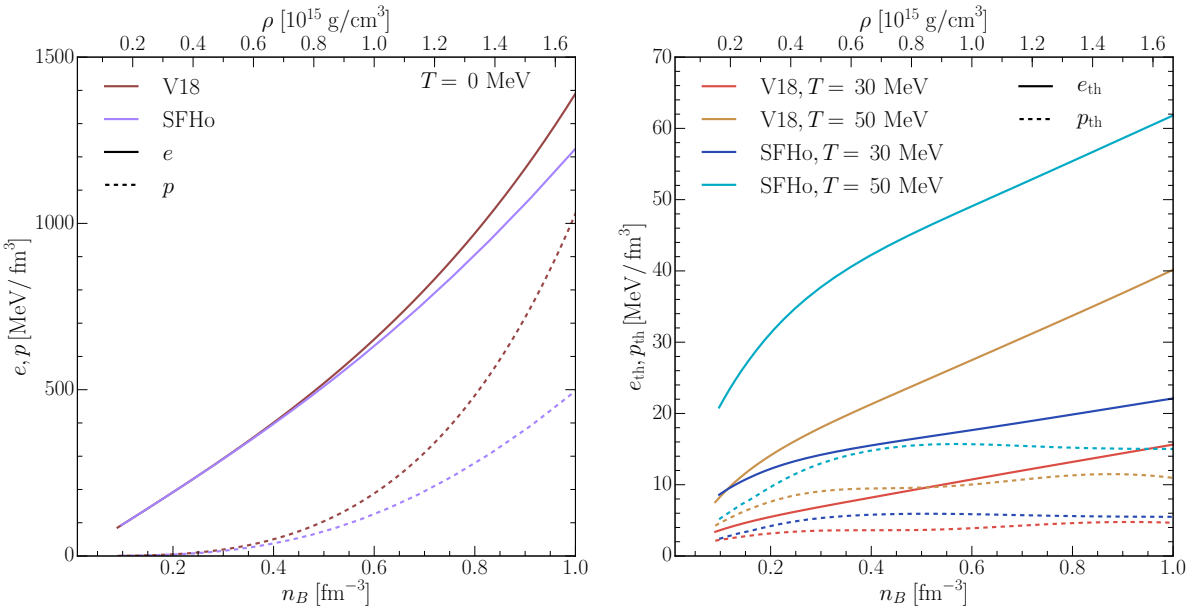

Figure 5.1 Comparison of the pressure p and energy density e of betastable matter at $T = 0$ as a function of the baryon number density for the V18 and SFHo EOSs (left panel). For both EOSs, the thermal pressure and internal energy density, Eqs. (5.3), (5.4) are also displayed at different temperatures (right panel).

MeV as a function of the baryon number density, while the right panel compares the thermal pressure and energy of the betastable EOSs, respectively defined as[4]:

$$p_{\rm th}(\rho, T) \equiv p(\rho, T) - p(\rho, 0) \tag{5.3}$$

$$e_{\rm th}(\rho, T) \equiv \rho(\epsilon(\rho, T) - \epsilon(\rho, 0)) \tag{5.4}$$

for different temperatures ($T = 30, 50\,\text{MeV}$). The figure shows that the V18 EOS is stiffer than SFHo, a feature to be considered in the interpretation of the simulation results. Interestingly in the V18 case the overall thermal effects are smaller than in SFHo, of the order of a few percent at high density, even at the fairly high temperature $T = 50\,\text{MeV}$ considered here (see [226] for a study on uncertainties of finite-temperature properties of neutron matter). This feature is not surprising, and has been already presented in Chapter 4 for the V18 case as a consequence of the interplay between the equally important nucleonic and leptonic contributions to the betastable EOS.

[4]The definition is identical to the one given in Chapter 4; notice, however, that the energy density is here labeled as $e_{\rm th}$ for consistency with the usual notation used in numerical relativity.

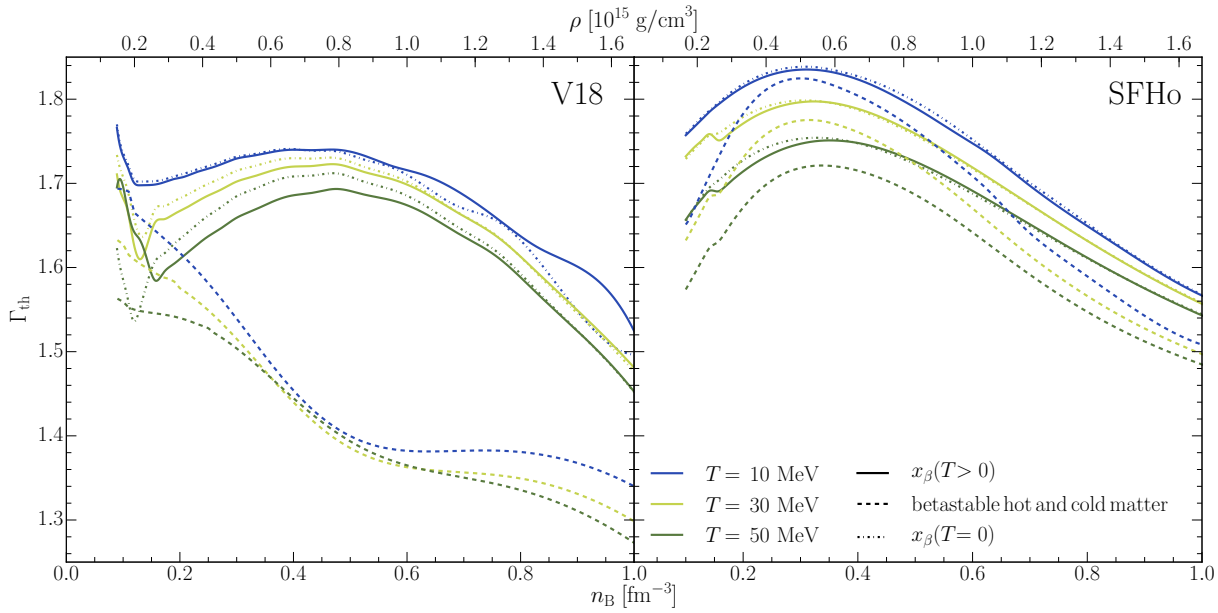

Figure 5.2 Adiabatic index of betastable matter, Eq. (5.5) computed at different temperatures, as a function of baryon number density. Results are obtained from betastable hot and cold matter (dashed curves), and by fixing the proton fraction to the one of betastable hot (cold) matter, represented with solid (dash-dotted) curves (a full description of the different methods is included in the text).

It is possible, for a given temperature-dependent EOSs, to compute $\Gamma_{\rm th}$ in the beta-stable prescription, according to

$$\Gamma_{\rm th}(\rho, T) \equiv 1 + \frac{p(\rho, x_\beta, T) - p(\rho, x_\beta, 0)}{\rho[\epsilon(\rho, x_\beta, T) - \epsilon(\rho, x_\beta, 0)]}\,, \tag{5.5}$$

where x_β is the betastable proton fraction at either $(\rho, T > 0)$ or $(\rho, T = 0)$. The resulting calculated values of $\Gamma_{\rm th}$ are reported in Fig. 5.2, where the solid (dash-dotted) curves display results with x_β taken at $T > 0\,(T = 0)$ for the V18 (left panel) and the SFHo EOS (right panel), respectively. The values determined according to this method lie in the range $1.5 \lesssim \Gamma_{\rm th} \lesssim 1.7$ for the V18 EOS, and $1.6 \lesssim \Gamma_{\rm th} \lesssim 1.8$ for the SFHo EOS, with the average value for the betastable matter being smaller in both cases. Interestingly, as will be followingly described in great detail, the merger simulations feature matter in the early remnant usually not in beta equilibrium and therefore all the values shown in Fig. 5.2 can only give qualitative indications of effective $\Gamma_{\rm th}$ values. Nevertheless, $\Gamma_{\rm th}$ can be calculated even out of beta-

equilibrium, using again Eq. (5.5), where, instead of considering the beta-equilibrium values x_β for the proton fraction, one just uses the proton fraction value corresponding to the considered point of the numerical domain.

As first investigated in Ref. [201], a constant-$\Gamma_{\rm th}$ may not represent a realistic choice for simulations in the hybrid-EOS approach (originally chosen as $\Gamma_{\rm th} \approx 1.5$ [205]), especially in the postmerger phase, where thermal effects are most relevant. Strong variations were found, indeed, in both the characteristic frequencies of the rotating remnant and the delay time between the merger and black-hole formation, with respect to the simulations with a fully consistent treatment of the temperature. It is then important to both quantify such differences, and at the same time determine a suitable value for $\Gamma_{\rm th}$ to be used in hybrid EOS simulations. In this regard, one can first study how different values of $\Gamma_{\rm th}$ affect the single NS properties, and in particular the gravitational mass M with respect to the central baryon number density n_c. Such a study is reported in Fig. 5.3, where sequences of nonrotating equilibrium models are shown as a function of the central baryon number density (or rest mass density) for the V18 EOS (left panel) and the SFHo EOS (right panel). Two curves refer to different temperatures ($T = 0$ and $T = 50$ MeV) where the exact temperature dependence is considered, and three further cases refer to choices of constant $\Gamma_{\rm th} = 1.1, 1.5, 1.75$. In other words, Eq. (5.4) is used at $T = 50$ MeV and the estimate of the thermal adiabatic index is then employed to compute the thermal contribution to the pressure, Eq. (5.1)[5].

For the V18 EOS, $M_{\rm TOV}(T = 0) = 2.387 M_\odot$ at a central rest-mass density $\rho_c = 1.58 \times 10^{15}$ g/cm^3 (corresponding to a baryon number density $n_c = 0.96$ fm^{-3}), while $M_{\rm TOV}(T = 50$ MeV$) = 2.372 M_\odot$ at $\rho_c = 1.53 \times 10^{15}$ g/cm^3 ($n_c = 0.93$ fm^{-3}). As already discussed in Sec. 4.2, these results are related to the competition of three different effects for fixed density and increasing temperature, namely:

- The thermal pressures of neutrons and protons, which increase with temperature;

[5]For this study, a cold crust is attached to the isothermal core at $n_B = 0.08$ fm^{-3}, corresponding to $\rho \approx 1.32 \times 10^{14}$ g/cm^{-3}.

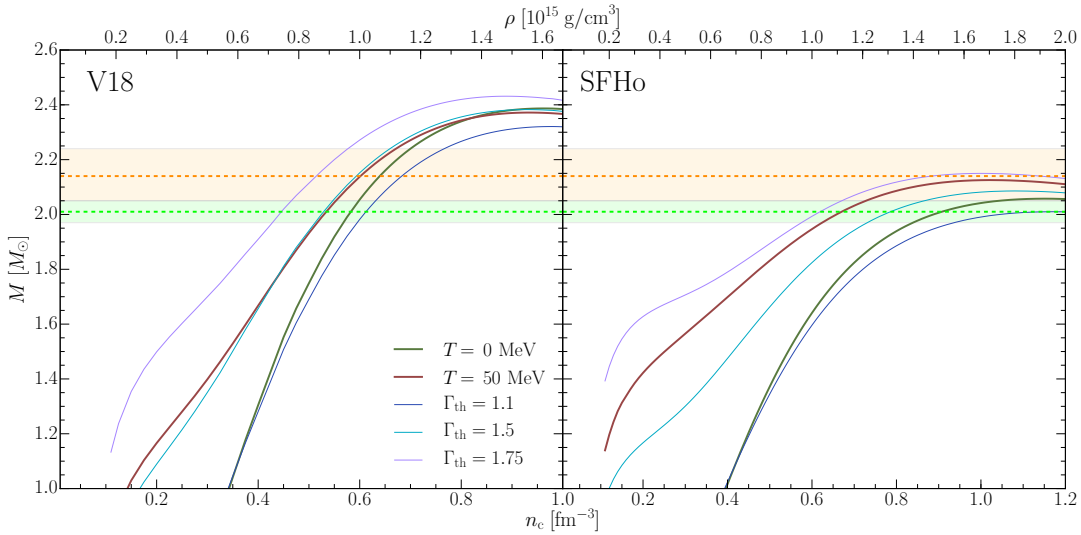

Figure 5.3 Gravitational mass as a function of the central baryon number density; the two cases for $T = 0$ and $T = 50$ MeV with full temperature treatment are shown, together with different choices of constant $\Gamma_{\rm th} = 1.1, 1.5, 1.75$ at $T = 50$ MeV. The observational constraints of Refs. [31, 32] are also included with dashed orange and green lines respectively, together with the shaded regions of the same color.

- The lepton thermal pressure, also increasing with temperature;

- The reduction of baryonic pressure due to the increase, with temperature, of the isospin symmetry, in turn due to beta-stability.

Due to the strongly repulsive character of the microscopic three-body forces employed, the V18 EOS is characterized by large values of the symmetry energy, which increases with temperature and density; this, in turn, implies a strong increase of the isospin symmetry with temperature and density [21].

Fig. 5.3 shows that, for the V18 EOS, the $\Gamma_{\rm th} = 1.5$ approximation at $T = 50$ MeV determines a mass profile which greatly resembles the full calculation one; hence, such a value of $\Gamma_{\rm th}$ represents the best approximation for betastable matter at finite temperature as it is the one that best mimics the effects of a full temperature dependence. In turn, and as shown in Fig. 5.2, this corresponds to about $\Gamma_{\rm th} = 1.7$ for the fixed-x_p definition of $\Gamma_{\rm th}$ that is used later in the actual numerical simulations.

The two values $\Gamma_{\rm th} = 1.1$ and 1.75 respectively predict lower and higher $M_{\rm TOV}$, according to the lower and higher thermal pressure they provide. One can also characterize the opposite

Table 5.1 Gravitational and baryonic masses M and M_B, and the equatorial radius R for the V18 and SFHo EOSs, for both static and maximally rotating stars with Kepler frequency at temperatures $T = 0$ and 50 MeV.

EOS	f [Hz]	T [MeV]	M [$M_\odot$]	M_B [$M_\odot$]	R [km]
V18	0	0	2.387	2.913	10.86
	0	50	2.372	2.785	11.40
	1770	0	2.845	3.385	14.17
	1590	50	2.724	3.102	15.00
SFHo	0	0	2.058	2.448	10.30
	0	50	2.126	2.450	11.81
	1741	0	2.472	2.911	13.73
	1376	50	2.413	2.726	15.98

effects of $p_{\rm th}$ and $e_{\rm th}$ on the maximum mass: the $\Gamma_{\rm th} = 1.1$ curves feature very small $p_{\rm th}$, so, in this case, the inclusion of $e_{\rm th}$ determines that $M_{\rm TOV}$ decreases with respect to the cold $M_{\rm TOV}(T = 0)$, whereas if also $p_{\rm th}$ is included (the $\Gamma_{\rm th}$=1.5, 1.75 curves, as well as the FT case) $M_{\rm TOV}$ increases again.

The SFHo case, whose results are shown in the right panel of Fig. 5.3, features a higher thermal pressure and adiabatic index, which leads to a larger temperature dependence of the maximum TOV mass when compared to the V18 case. The full calculation at $T = 50$ MeV, in this case, seems to be better reproduced by the $\Gamma_{\rm th} \simeq 1.7$ approximation.

The values of the TOV masses at $T = 0$ and $T = 50$ MeV, together with other useful information such as the rotation frequencies at the mass-shedding limit, are summarized in Table 5.1.

The differentially rotating merger remnant supports a mass which is upper bounded only

by the threshold mass to prompt collapse to a black hole, that can be estimated to be [227]

$$M_{\rm th} = M_{\rm TOV}\left(3.06 - \frac{1.01}{1 - 1.34\, M_{\rm TOV}/R_{\rm TOV}}\right). \tag{5.6}$$

For the V18 EOS, a threshold mass according to Eq. (5.6) is determined to be $M_{\rm th} = 3.04 M_\odot$ with $M_{\rm TOV}/R_{\rm TOV} = 0.324$, while in the SFHo case $M_{\rm th} = 2.86 M_\odot$, being $M_{\rm TOV}/R_{\rm TOV} = 0.295$ (in geometrized units with $c = G = M_\odot = 1$).

Since a major objective of this study is represented by the comparison of results obtained with simulations including the full temperature treatment (from hereon labeled as FT) with respect to simulations carried out in the hybrid EOS approach, the numerical setup (discussed in great detail in Ref. [24] and references therein), presented in Sec. 2.5.3, is identical for both types. For both EOSs, initial data are characterized by two stars with gravitational masses at infinite separation $M = 1.35 M_\odot$ in quasi-circular orbits and with an initial separation of 45 km. Time evolutions are then performed with the full temperature treatment (two simulations, with the V18 and SFHo EOSs respectively) and in the hybrid EOS approach; in the latter case, the different values $\Gamma_{\rm th} = 1.1, 1.5, 1.75$ are considered for the V18 EOS, whereas $\Gamma_{\rm th} = 1.5, 1.75$ are examined for the SFHo EOS. Clearly, the simulations with the consistent temperature treatment are regarded as the most realistic ones and the values of $\Gamma_{\rm th}$ are iterated in simulations in the hybrid EOS approach to find the closest match in the bulk behaviour of the matter. It is also important to remark that the hybrid-EOS simulations are carried out using the betastable tables at $T = 0$, so that the simulation is "forced" to treat betastable matter (corrected with the already described finite-temperature effects). The FT simulations, on the other hand, are free to drive away from the betastable condition, and indeed this is what happens starting from the very beginning, which will be presented followingly into more detail.

5.3 Numerical results

5.3.1 Bulk hydrodynamics

The merger simulations follow the stars for about 4 orbits before merging into a single, centered, differentially rotating object; such a metastable HMNS is then evolved up to the largest time $t \approx 20\,\mathrm{ms}$ reached in the simulations. At that time, for the simulations performed with the V18 EOS, the remnant is still stabilized by differential rotation and finite temperature contributions to the pressure, a feature that seems to be compatible with the multimessenger analysis of the GW170817 event [228]. The simulations performed with the SFHo EOS result, instead, in a rather rapid collapse into a black hole, which seems to be in contrast with the expected amount of mass ejected in the GW170817 event.

Figure 5.4 shows, in the two uppermost panels and as a first tracker of the hydrodynamic properties, the time evolution of the maximum rest-mass density, $\rho_{\max}$, for the different cases analyzed here, whereas the third and fourth panel report the evolution of both the maximum and the density-weighted average temperature, defined as

$$\langle T \rangle \equiv \frac{\int dV \rho T}{\int dV \rho}\,, \tag{5.7}$$

where the average is performed on the $z = 0$ plane, after applying a low-density threshold of 10^{13} g/cm^3 to avoid contamination from the very light but very hot matter ejected; the threshold is set to 10^{10} g/cm^3 in order to also calculate the averaged quantities even after the collapse in the SFHo models. In this plot, as well as the following ones, the time coordinate is normalized such that $t = t_{\mathrm{merg}} = 0$, where t_{merg} is the time of the merger and corresponds to the maximum of the gravitational-wave amplitude, for all the cases we study. The behavior presented here is in good agreement with what has been found also for other temperature-dependent EOSs, e.g., Refs. [204, 229, 230]. In the lowest panel, for both FT EOSs, the density-weighted average relative deviation from beta stability

$$\left\langle \frac{\Delta Y_{e\beta}}{Y_e} \right\rangle \equiv \frac{\int dV \rho \, \frac{|Y_{e\beta} - Y_e|}{Y_{e\beta}}}{\int dV \rho}\,, \tag{5.8}$$

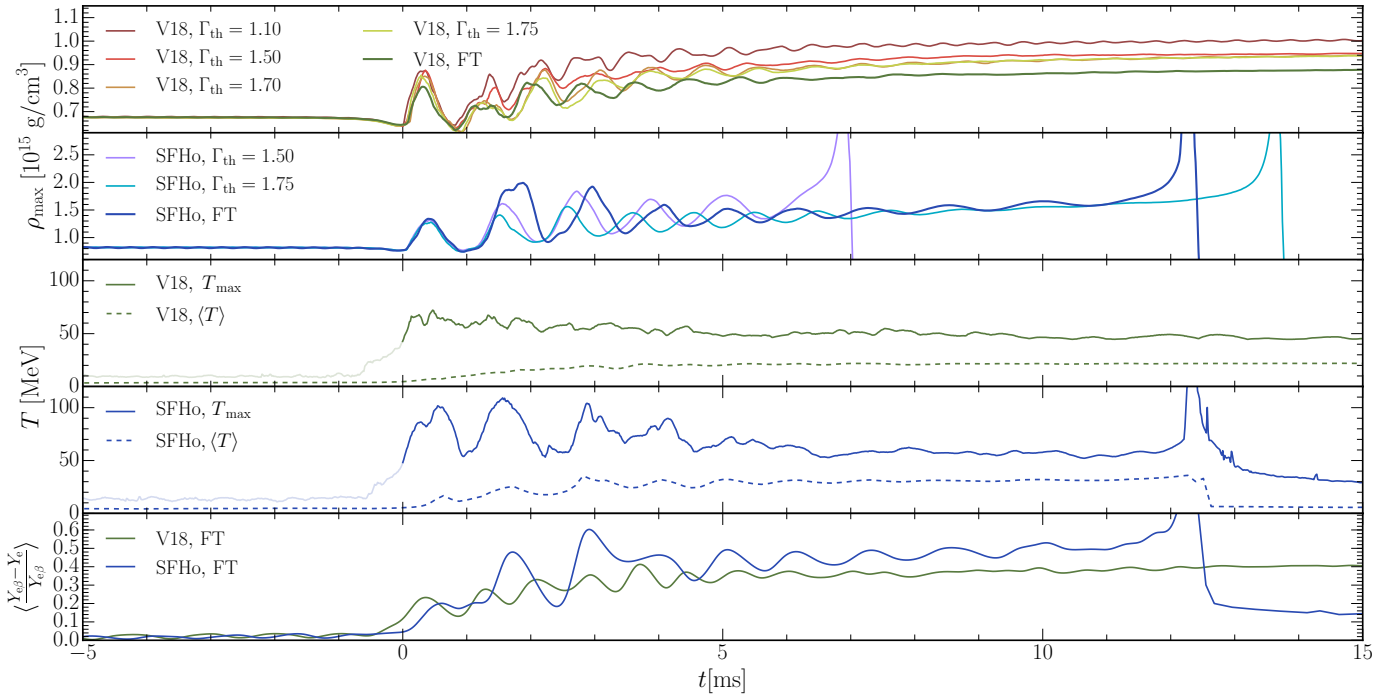

Figure 5.4 Time evolution, for the complete set of simulations, of the maximum values of rest-mass density (upper panels) and temperature (third and fourth panels from the top, only for the simulations using the FT EOSs). The evolution of the average temperature $\langle T \rangle$, calculated according to Eq. (5.7), is also displayed; for the inspiral phase, characterized by a lighter color, such temperatures are meant as representative only and do not reflect an accurate description of the thermodynamics of the matter. The average deviation from beta-stability, Eq. (5.8), is also represented for both FT EOSs (lowermost panel).

is shown, where $Y_{e\beta}(\rho, T)$ represents the electron fraction calculated pointwise on the $z = 0$ plane assuming beta equilibrium at the density ρ and temperature T of each point. For both EOSs, differences of over 40% are found, with the V18 remnant stabilizing about that value.

In the analysis of the simulations carried out with the V18 EOS, the $\Gamma_{\rm th} = 1.1$ case is found to produce, unsurprisingly, the remnant with the highest maximum rest-mass density ($\rho_{\rm max} \approx 10^{15}$ g/cm^3), which decreases to about 0.94×10^{15}g/cm^3 with increasing $\Gamma_{\rm th}$. This feature is indeed the consequence of the fact that increasing the thermal support against gravity leads to a less dense remnant. The plot shows also that the temperature-dependent EOS leads to a remnant with an even smaller maximum rest-mass density ($\rho_{\rm max} \approx 0.88 \times 10^{15}$ g/cm^3) than the hybrid-EOS cases. This feature is most interesting, since it points to a

systematic difference between the two types of simulations: while the hybrid method is by construction based on an EOS of cold betastable matter with thermal corrections, the full simulation produces matter strongly out of beta equilibrium, see the lowest panel of Fig. 5.4, as will be analyzed later.

The simulations carried out with the SFHo EOS show that the remnant collapses into a black hole after a time which strongly depends on the chosen thermodynamical treatment; indeed, the collapse is registered at $t \approx 7\,\mathrm{ms}$ or $t \approx 14\,\mathrm{ms}$ for the cases in which $\Gamma_{\mathrm{th}} = 1.50$ or $\Gamma_{\mathrm{th}} = 1.75$, respectively, and at $t \approx 13\,\mathrm{ms}$ for the FT EOS. Furthermore, before collapse, the fluctuations of the rest-mass density and temperature are more violent than for the V18 EOS during this metastable phase.

The maximum temperature for the FT simulations shows peaks of about 70 MeV and 110 MeV for the V18 and SFHo EOS respectively, which are reached locally and only in small zones of the computational domain; the information is thus completed by reporting the density-weighted average temperature. For both EOSs, even during the inspiral, the latter quantity is much smaller than the maximum temperature; during the inspiral, indeed, maximum temperatures are mostly related to numerical artifacts and are reached in the outermost regions of the stars, whereas the postmerger average temperature finds its explanation in the fact that the densest part of the remnant is also the coldest, and higher temperatures are found in the lower density regions around the core.

As a final confirmation, during the inspiral phase there is no great deviation from beta-stability, with average values mostly below 5%; the post-merger remnant manifests instead important differences with respect to the latter, with average deviations of about 40% and 50% for V18 and SFHo respectively.

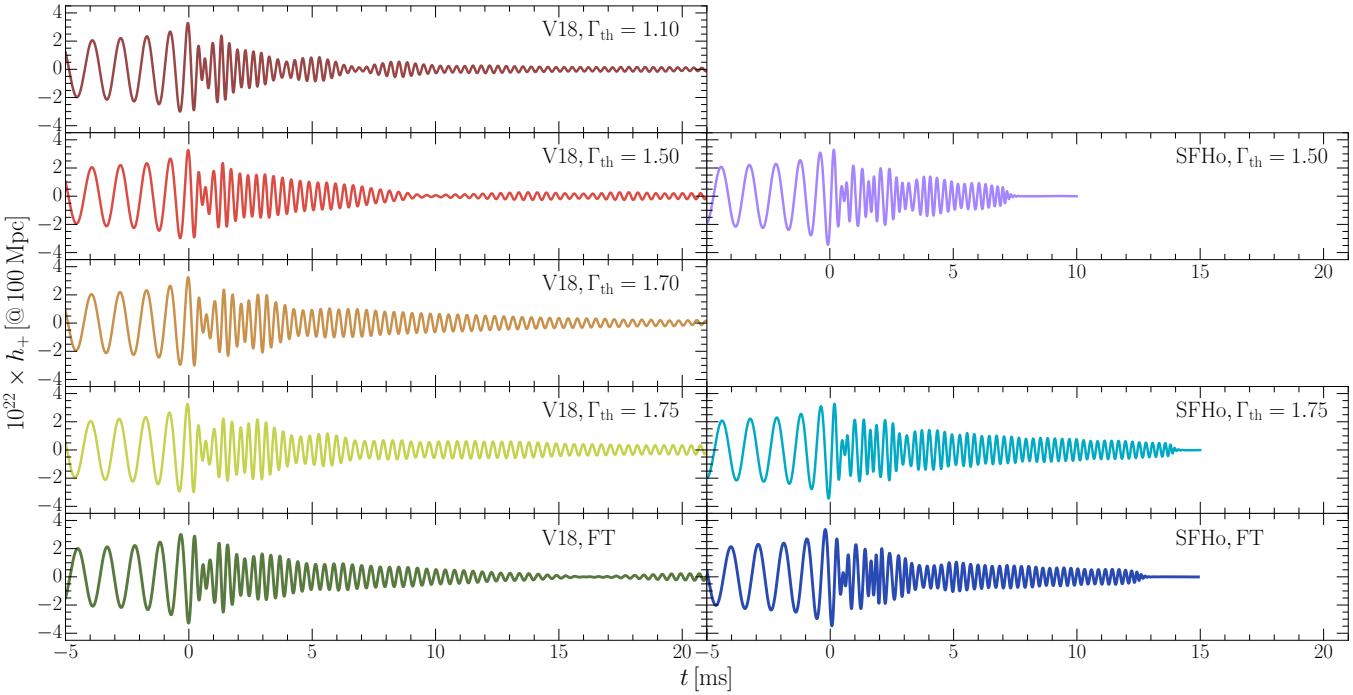

Figure 5.5 Gravitational-wave strain over a time scale of about 20 ms after the merger for the V18 and SFHo EOSs obtained for the standard equal-masses setup $2 \times 1.35 M_\odot$; the different cases $\Gamma_{\rm th} = 1.1, 1.5, 1.7, 1.75$ and FT are reported.

5.3.2 Gravitational-wave properties

The plus polarization of the $l = m = 2$ component of the gravitational-wave strains, labeled as h_+, is reported in Fig. 5.5 for all the considered simulations. As expected, no significant differences are found in the inspiral part of the signal, the only notable feature being that the time of merger, which, following a common convention, is considered as the time corresponding to the maximum of the strain amplitude, varies slightly when varying $\Gamma_{\rm th}$ in the hybrid EOS approach (with maximum variations of about 0.05 ms with respect to the average times calculated for both EOSs in the hybrid EOS approach). The time of merger measured in the FT runs for both the V18 and the SFHo EOS differs instead of ≈ 0.6 ms with respect to the average time calculated in the hybrid-EOS approach. On the other hand, as clearly shown in Fig. 5.5, different thermodynamic treatments for the same EOS result in very different postmerger profiles.

The power spectral density (PSD) plots of all simulations are presented in Fig. 5.6,

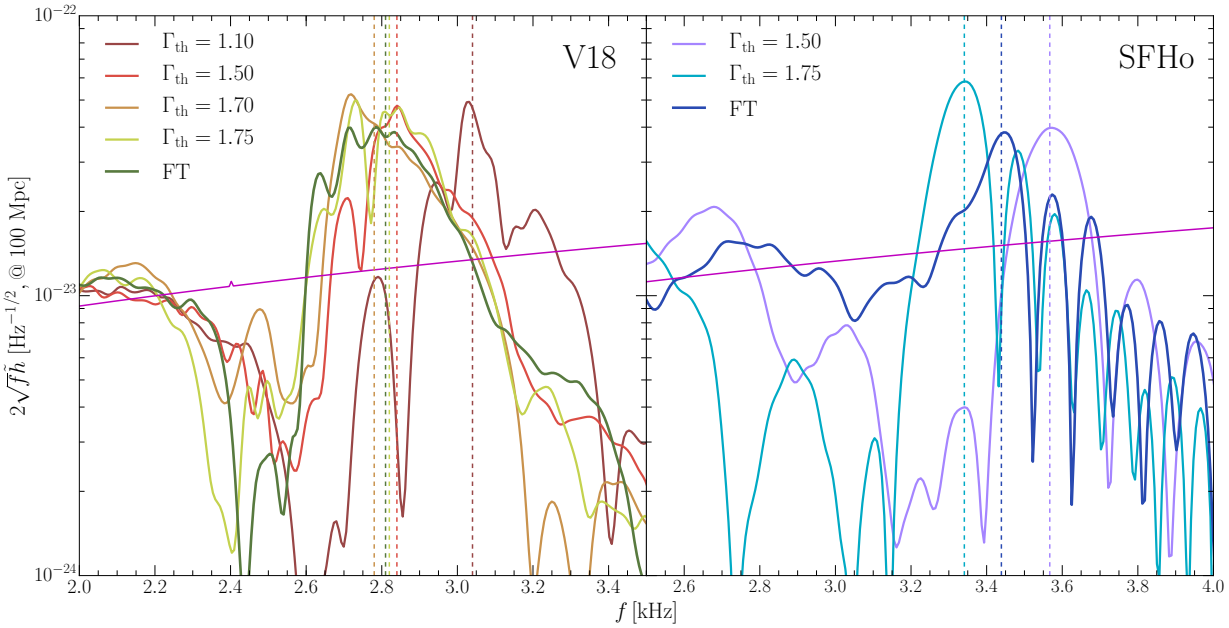

Figure 5.6 Power spectral density (PSD) plots of the simulations with the V18 and SFHo EOSs, at a distance of 100 Mpc. The frequency f_2 evaluated for each simulation is represented as a vertical dashed line of the same color of the curve it is referring to. The sensitivity curve (magenta color) of Advanced LIGO is shown for reference.

determined as detailed in Appendix A. In particular, in order to characterize the different behaviors, the dominant $l = m = 2$ mode is considered, and the position of the related f_2 peak in the spectrum (where the same nomenclature of Ref. [231] is adopted) is identified as a tracker. Since especially for the V18-EOS cases with higher $\Gamma_{\rm th}$ it is difficult to distinguish the dominant f_2 peaks, a fitting procedure represents the only way to accurately determine the f_2 positions (see Appendix A for a discussion on the fitting procedure and its related errors). Table 5.2 reports these values for each simulation, together with their indetermination, as well as the $f_{\rm max}$ values, and the emitted gravitational-wave energy $E_{\rm GW}$ for the $l = m = 2$ mode, measured as discussed in the Appendix A. As a general trend, one can recognize that f_2 decreases and $E_{\rm GW}$ increases with increasing $\Gamma_{\rm th}$, while $f_{\rm max}$ depends very weakly on $\Gamma_{\rm th}$ and makes it impossible to find any specific dependence. Apart from understanding that $\Gamma_{\rm th}$ lies in the range between 1.5 and 1.75, however, it is not possible to determine a specific, ideal

value of $\Gamma_{\rm th}$ from the information contained in Table 5.2, also as a result of the uncertainties associated to the fitting procedure involving the study of the f_2 peak. Other methods will then be used in order to measure $\Gamma_{\rm th}$ directly from the simulations.

Table 5.2 GW properties for all the investigated simulations: instantaneous frequency at amplitude maximum $f_{\rm max}$, frequency associated to the f_2 peak, and total emitted energy $E_{\rm GW}$.

Simulation	$f_{\rm max}$ [kHz]	f_2 [kHz]	$E_{\rm GW}$ [10^{52} erg]
V18 - FT	1.77	2.81±0.02	5.28
V18 - $\Gamma_{\rm th} = 1.75$	1.79	2.82±0.08	5.84
V18 - $\Gamma_{\rm th} = 1.7$	1.77	2.78±0.07	5.68
V18 - $\Gamma_{\rm th} = 1.5$	1.79	2.84±0.01	4.97
V18 - $\Gamma_{\rm th} = 1.1$	1.81	3.04±0.01	4.46
SFHo - FT	1.95	3.44±0.01	6.89
SFHo - $\Gamma_{\rm th} = 1.75$	1.92	3.34±0.01	7.80
SFHo - $\Gamma_{\rm th} = 1.5$	1.93	3.57±0.01	6.38

Interestingly, the f_2 frequencies reported in Table 5.2 agree reasonably well with both the universal relation between f_2 and the tidal deformability parameter k_2^T [231] and the radius of a $1.6 M_\odot$ NS, $R_{1.6}$ [232], which are included here for completeness:

$$f_2 \approx 5.832 - 1.118 \left(k_2^T\right)^{1/5} \approx 2.95 \qquad \text{[kHz]} \tag{5.9}$$

$$f_2 \approx 8.713 - 0.4667\, R_{1.6} \approx 2.86 \qquad \text{[kHz]} \tag{5.10}$$

where $k_2^T = 113.08$, $R_{1.6} = 12.54\,$km for the V18 EOS, and $k_2^T = 78.75$, $R_{1.6} = 11.77\,$km for the SFHo EOS.

As a further important remark, the simulation employing the V18 EOS with $\Gamma_{\rm th} = 1.1$ determines the highest frequency of the f_2 peak ($\sim 230\,$Hz above the FT value). Such a

finding is a further confirmation of the behavior of the rest-mass density found in Fig. 5.4; indeed, as the frequency of the mode scales with the square root of the average density (see, e.g., Ref. [233]), the value of the f_2 peak frequency represents spectroscopical confirmation of the fact that the considered remnant not only has the largest central density, but it also is the most compact one and is therefore characterized by the fastest oscillations among all the cases considered.

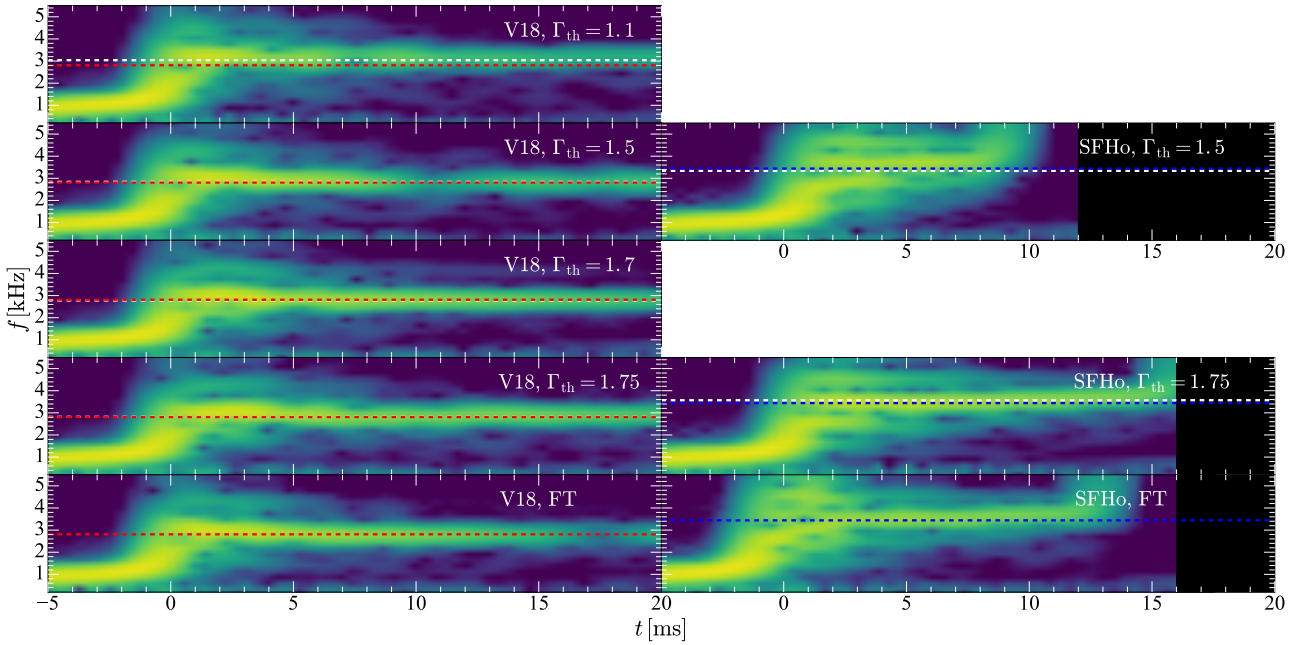

Figure 5.7 The spectrograms for all the considered cases. White dashed lines indicate the position of the f_2 peak for the hybrid-EOS cases, while red (blue) dashed lines represent the position of the f_2 peak for the fully tabulated V18 (SFHo) simulation.

In order to better visualize the characteristic frequencies as a function of time, the spectrograms for all the models here investigated are included in Fig. 5.7. The prominent f_2 peaks appear immediately after the merger and are clearly visible for the entire duration of all simulations; the positions of the peaks are labeled with white dashed lines for each case and compared with red (blue) lines representing the position of the same peak for the fully tabulated V18 (SFHo) simulation. It clearly emerges that the feature is very robust: it is distinguishable in all cases and is the only frequency which survives up to the end of

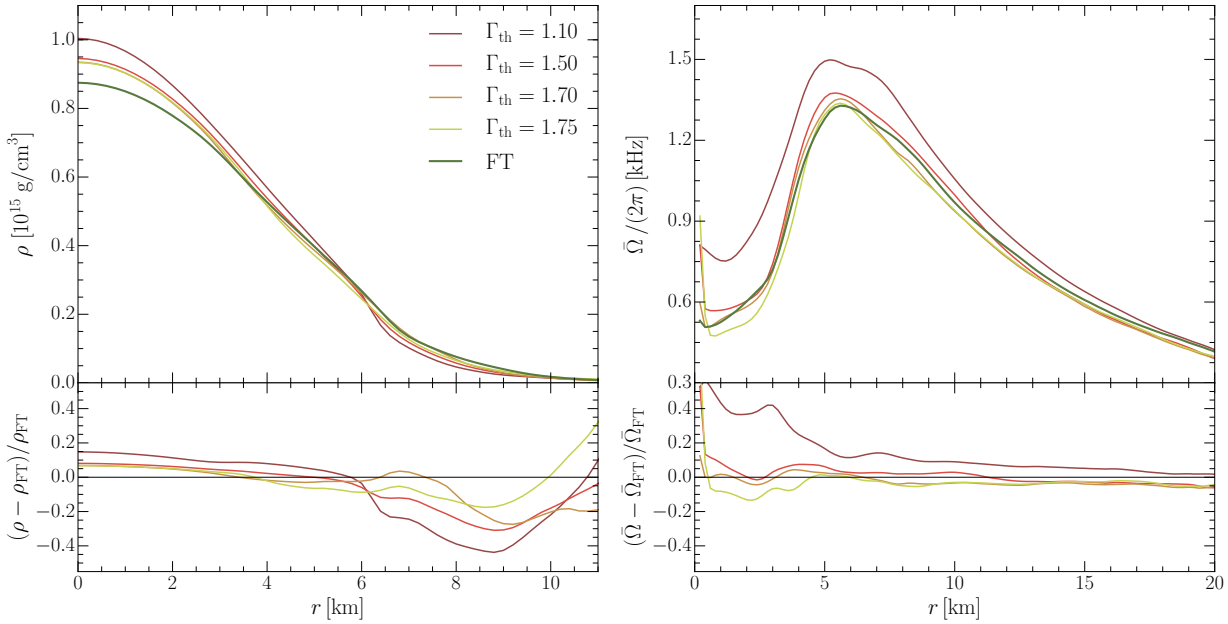

Figure 5.8 Azimuthal and time averages (see description in the text) rest-mass density and angular velocity for the different V18-based EOSs as a function of the radial coordinate r ($z = 0$) at $t = 14$ ms. Fractional differences with respect to the FT results are included in the lower panels.

the simulation (or the collapse, as in the case of the SFHo simulations). Other typical frequencies can be observed immediately after the merger, among which the f_1 and f_3 peaks, which disappear in the first few ms of the post-merger phase; their investigation, however, is beyond the scope of this work.

5.3.3 Determination of an effective thermal adiabatic index

In order to quantitatively investigate the density and frequency features for the different simulations, the one-dimensional profiles of the averaged rest-mass density and of the angular velocity are computed at a representative time $t \approx 14$ ms after the merger and shown in Fig. 5.8 (upper left and right panels respectively). Such profiles are obtained from the values of the corresponding quantities on the equatorial plane ($z = 0$), by averaging first on the azimuthal direction and then over a time window of 1 ms, so that the resulting function only depends on the cylindrical radius, r, from the center of the grid.

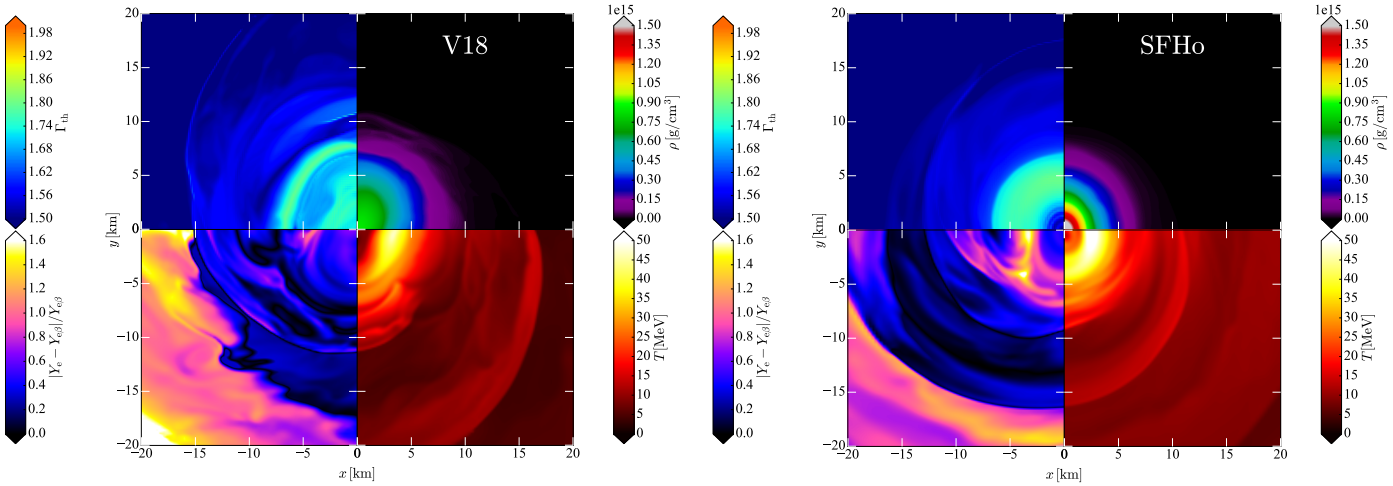

Figure 5.9 Distributions of $\Gamma_{\rm th}$, calculated as described in the text (upper left panels of the figures), rest-mass density (upper right), temperature (lower right), and deviation from beta stability (lower left), in the $z = 0$ plane at $t \approx 9\,$ms after the merger.

In order to better quantify the deviation with respect to the FT simulation, the fractional differences of the hybrid-EOS profiles with respect to the fiducial FT ones are reported in the bottom panels. Such results indicate that differences in density remain below 10% in the core of the remnant (i.e., $r \lesssim 6\,$km) for the cases $\Gamma_{\rm th} = 1.5, 1.7, 1.75$, and increase for densities below $\rho \approx 2 \times 10^{14}$g/cm^{-3}. Interestingly, one notices that in the core area, which is dynamically the most important one, the case $\Gamma_{\rm th} = 1.1$ is always representative of the largest differences, whereas the case $\Gamma_{\rm th} = 1.7$ yields the smallest fractional differences.

As a major objective of this study is to determine which value of $\Gamma_{\rm th}$ best represents the FT features, one can compute such values pointwise according to Eq. (5.5), thus using the values, at each point, of ρ, Y_e, p, ϵ and T obtained in the FT simulations and the FT tables to compute p and ϵ at $T = 0$. This way of computing $\Gamma_{\rm th}$ ignores the betastability condition of cold matter, since Y_e is not the proton fraction of cold betastable matter, but allows one to perform a complete study on the parameter space of ρ, Y_e and T explored during the numerical simulation. The method is then very similar to the fixed-x_p prescription used in Fig. 5.1 with $x_\beta(T > 0)$, with the difference that the proton fraction of matter at $T > 0$ is not the one imposed by beta-stability but the one evaluated locally in the numerical domain.

The distributions of $\Gamma_{\rm th}$ calculated pointwise on the $z = 0$ plane at time $t = 9\,$ms, for both the V18 and the SFHo simulations, are included in Fig. 5.9 (upper left panels). The same figure also reports the distributions of the rest-mass density ρ (upper right quadrants), the temperature T (lower right quadrants), and the deviation of the electron fraction from its betastable value, $(Y_{e\beta} - Y_e)/Y_{e\beta}$ (lower left quadrants). It is possible to recognize that, for the V18 EOS (right panel), it is generally $\Gamma_{\rm th} \lesssim 1.6$ for $\rho \lesssim 5 \times 10^{13}$g/cm^3, and very close to $\Gamma_{\rm th} \simeq 1.7$ for higher densities and hence in the core of the HMNS.

The FT simulation carried out with the SFHo EOS (right panel) is characterized instead by $\Gamma_{\rm th} \gtrsim 1.7$ in the density region $10^{14} \lesssim \rho/\ {\rm g/cm^3} \lesssim 10^{15}$, whereas $\Gamma_{\rm th} \lesssim 1.65$ dominates the highest-density region. The figure thus confirms the thermal adiabatic index behavior deduced from Fig. 5.6, namely, that a value $\Gamma_{\rm th} \approx 1.7$ is in good agreement with the post-merger spectroscopic properties observed in the two FT EOSs.

For both FT simulations reported in Fig. 5.9, the typical appearance of two hot spots with $T > 50$ MeV [210, 234] is noticed; their temperature evolution was shown in Fig. 5.4 with their presence generally related to the conservation of the Bernoulli constant (see Ref. [210] for a detailed discussion). At about $t \simeq 22\,$ms, these hotspots merge into a ring-shaped structure, which remains evident until the end of the time evolution. Fig. 5.9 also clearly shows that the remnant matter, especially in the low-density layers of the HMNS, is out of beta equilibrium (in this regard, density-weighted averaged values were plotted in Fig. 5.4) As discussed above, this deviation limits the validity of the comparison of the dynamical and thermodynamical properties of the matter between simulations carried out with the FT EOSs and with hybrid EOSs.

Fig. 5.9 also shows that $\Gamma_{\rm th}$ is far from being constant in the numerical domain, as instead it depends strongly on density, temperature, and electron fraction at each point of the computational domain. One can however identify a reference value of $\Gamma_{\rm th}$ by performing a density-weighted average, as done for the temperature and the deviation from beta-stability, and inspecting how much this average varies with time; such an average is then calculated

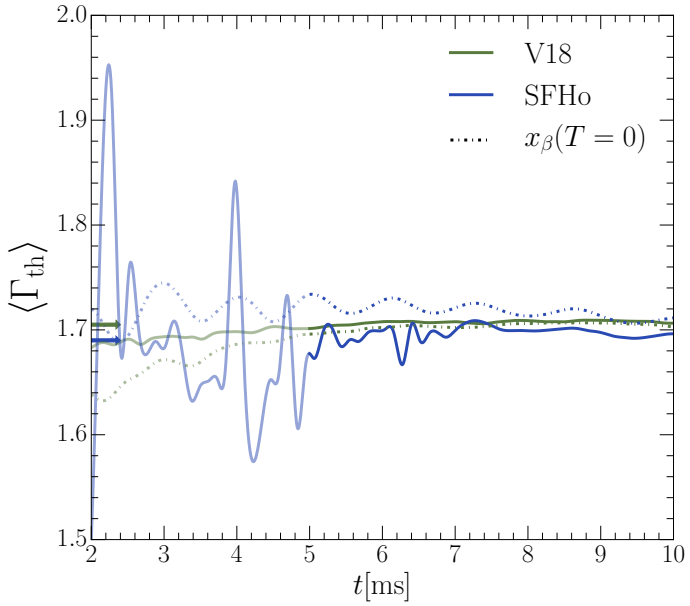

Figure 5.10 Density-weighted $\Gamma_{\rm th}$, Eq. (5.11), as a function of time for the FT simulations with the V18 and SFHo EOSs. Time averages related to the total time interval considered here are represented as arrows in the plot. As a comparion, dotdashed curves represent the average values of $\Gamma_{\rm th}$ calculated using Eq. (5.5) with $x_p = x_\beta(\rho, T = 0)$, as described in the text.

according to

$$\langle\Gamma_{\rm th}\rangle \equiv \frac{\int dV \rho \Gamma_{\rm th}}{\int dV \rho} \,, \tag{5.11}$$

where, also in this case, the average is performed after applying a low-density threshold of 10^{13} g/cm^3 [6].

Figure 5.10 reports the evolution of the average thermal adiabatic index, in a time window between 5 and 10 ms after merger; such a time interval is chosen as the fluctuations of $\Gamma_{\rm th}$ for the SFHo EOS are minimal so that it is possible to determine a representative time average. As a result, for both EOSs, $\langle\Gamma_{\rm th}\rangle \simeq 1.7$, with the corresponding time and spatial averages for the V18 and the SFHo EOS are $\langle\bar{\Gamma}_{\rm th}\rangle = 1.705$ and $\langle\bar{\Gamma}_{\rm th}\rangle = 1.690$, respectively (indicated by arrows). These averages also include the initial time interval, $2 \lesssim t/\text{ms} \lesssim 5$, when the HMNS has just been formed and the dynamics are still very far from being quasi-stationary

[6] Results have been verified to be insensitive to changes of this limit threshold, with deviations of $\Gamma_{\rm th}$ of the order 3×10^{-3} when 10^{12} g/cm^3 is chosen instead.

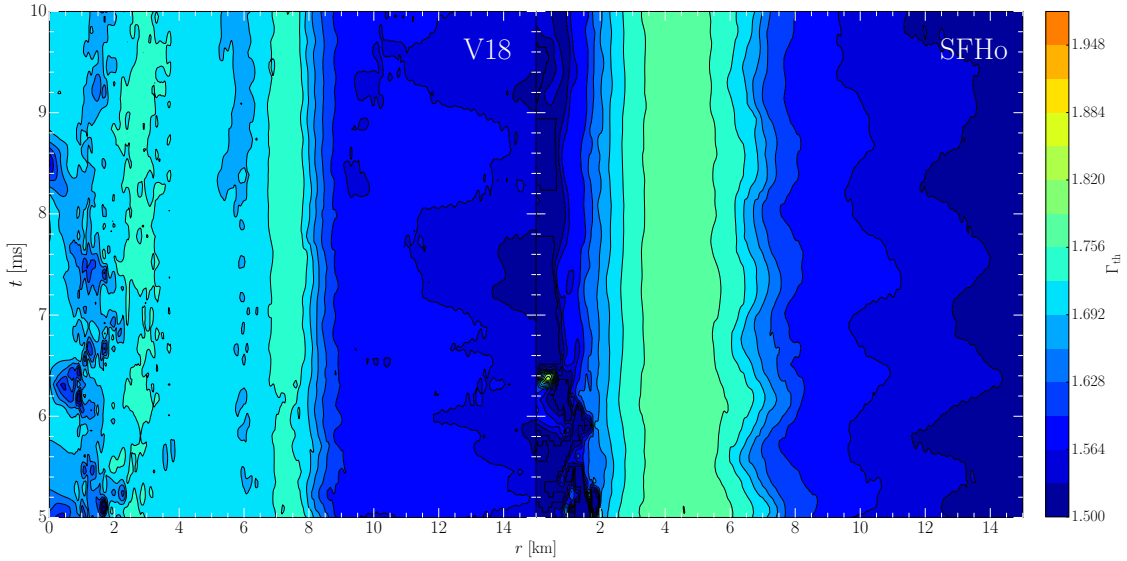

Figure 5.11 Iso-contours of $\Gamma_{\rm th}$ as a function of cylindrical radius r and time t for the V18 and SFHo FT simulations.

(light-colored curve segments). As a further confirmation of these results, the average of $\Gamma_{\rm th}$, calculated using the values of p and e evaluated employing x_β at $T = 0$ (as done, for example, in Fig. 5.2), is also calculated and reported in the same figure. Also in this case, good agreement with the value 1.7 if found for both EOSs.

Figure 5.11 shows a selection of $\Gamma_{\rm th}$ iso-contours on the $z = 0$ plane for the time window between 5 and 10 ms after the merger takes place. Interestingly, the distribution shown in Fig. 5.9 remains robust for the time window considered; in particular, it is clearly visible that for both V18 and SFHo the $\Gamma_{\rm th}$ distribution peaks off-centre. In details, the V18 model is characterized by two stable and narrow peak-structures at about 3 and 7 km, while the SFHo one shows a broader peak-region, approximately comprised between 3 and 6 km. The high density regions also show important differences, being characterized by higher $\Gamma_{\rm th}$ for V18 and values even lower than 1.5 for SFHo. For the latter case, local strong oscillations, residuals of the stronger oscillations affecting the previous part of the simulation, are evident for the first ms of the time-window we show, in particular, in the region near the centre.

In summary, in the light of the considerations and the studies carried out in this chapter, the value $\Gamma_{\rm th} \approx 1.7$ is found to be representative of the thermal adiabatic index distribution

and is the suggested prescription for BNS merger simulations in the hybrid EOS approach; interestingly, the value here determined is similar to the standard one employed in numerical simulations so far (i.e., $\Gamma_{\rm th} = 1.75 \sim 1.80$), but it's also importantly lower.

CHAPTER 6

BINARY NEUTRON STAR MERGERS WITH HOT MICROSCOPIC EOSS

6.1 Introduction

The finite temperature EOSs derived and discussed in Chapter 4 have been recently shown to fulfill all current constraints imposed by observational data from nuclear structure, heavy-ion collisions, NS global properties, and recently NS merger events [235]. The aim of this Chapter is therefore the systematic study and discussion of the results obtained in the context of BNS simulations carried out with the aforementioned EOSs, focusing in particular on the gravitational wave signal and matter distribution properties.

While the properties of static NSs modeled with the V18, BOB, N93 and UIX EOSs have already been presented in Ch. 4, and the application of these EOSs to numerical codes is instead discussed in Appendix B, it is interesting to first investigate the features of rotating stars modeled using the four EOSs, so to make it possible to carry out comparisons with the rotating simulated post-merger objects. Indeed, finite temperature and differential rotation represent two crucial factors that greatly affect the matter distribution and the

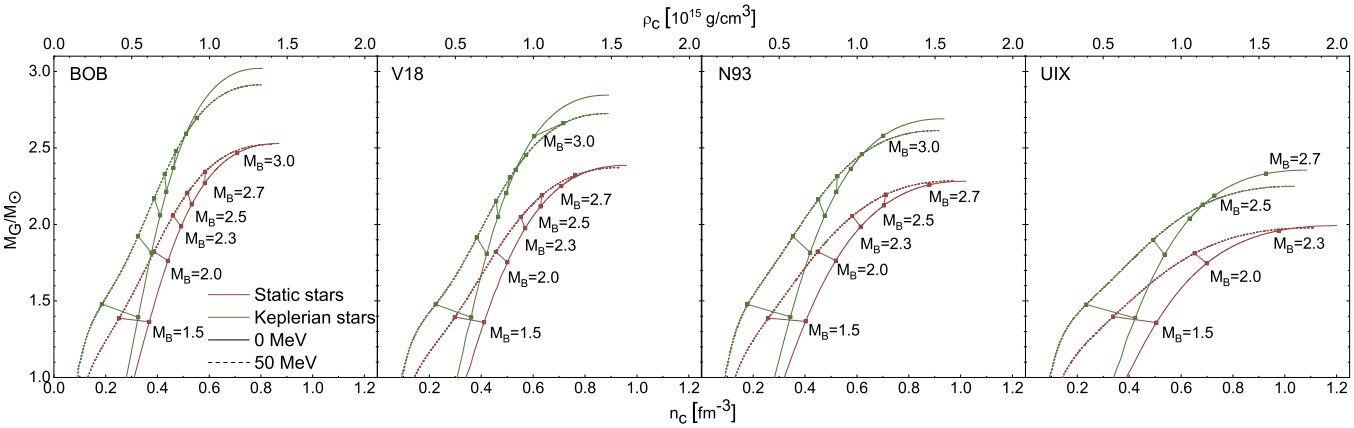

Figure 6.1 Maximum mass configurations of static (upper panels) and maximally rotating stars with Kepler frequency (lower panels) at T = 0 and 50 MeV; both gravitational and baryonic masses M and M_B, radius R, and central density n_c are reported. The threshold mass $M_{\rm th}$, Eq. (5.6), and the baryonic mass of a 2.7 $M_\odot$ rotating object, Eq. (6.6), are also included for comparison.

stellar stability of the post-merger remnant and their impact can be investigated even before carrying out BNS merger simulations.

In this context, Fig. 6.1 shows the gravitational mass $M_{\rm G}$ vs. central density n_c diagrams comparing both static and rotating (at mass-shedding velocity) models at the two temperatures $T = 0, 50$ MeV for the different EOSs.

The figure clearly shows that all the EOSs but UIX have a maximum mass exceeding the current observational limit, $M_{\rm TOV} > 2.14^{+0.10}_{-0.09} M_\odot$ [32]; furthermore, the investigations on the radii carried out in [23] have shown that the values related to a 1.4-solar-mass NS, $R_{1.4} = 12.97, 12.47, 12.91, 11.96$ km for BOB,V18,N93 and UIX respectively, fulfill the constraint derived from the tidal deformability in the GW170817 merger event, $R = 11.9 \pm 1.4$ km [236]. Such values are also in agreement with estimates of the mass and radius of the isolated pulsar PSR J0030+0451, recently observed by NICER, $M = 1.44^{+0.15}_{-0.14} M_\odot$ and $R = 13.02^{+1.24}_{-1.06}$ km [237], or $M = 1.34^{+0.15}_{-0.16} M_\odot$ and $R = 12.71^{+1.14}_{-1.19}$ km [238].

Table 6.1 summarizes the information shown in Fig. 6.1, also including the threshold mass for prompt collapse, determined according to Eq. (5.6), and the total baryonic mass related to a remnant of an equal mass BNS merger with $M = 1.35 M_\odot$. Interestingly, the

Table 6.1 Properties of the maximum mass configurations of static (first rows) and maximally rotating stars (at mass-shedding frequency, second rows) for each EOS at $T = 0$ and 50 MeV (values in brackets): gravitational and baryonic masses M and M_B, radius R, central density n_c, threshold mass $M_{\rm th}$, tidal deformability $\Lambda_{1.35}$ and radius of the $M = 1.6M_\odot$ configuration. The total baryonic mass $M_B^{\rm sim}$ of a remnant originating from a BNS merger with equal masses of components $M = 1.35M_\odot$ is also included for comparison for each EOS, as well as the total baryonic mass of the GW170817 remnant.

EOS	f (kHz)	$M/M_\odot$	$M_{\rm th}/M_\odot$	$M_B/M_\odot$	$M_B^{\rm sim}/M_\odot$	$M_B^{\rm GW170817}/M_\odot$	R (km)	n_c (fm^{-3})	$\Lambda_{1.35}$	$R_{1.6}$ (km)
BOB	0	2.53 (2.52)	3.17	3.10 (2.99)	2.95	3.00	11.38 (11.93)	0.87 (0.84)	755	12.98
	1.70 (1.55)	3.02 (2.91)		3.61 (3.33)			14.86 (15.56)	0.80 (0.79)		
V18	0	2.39 (2.37)	3.03	2.91 (2.79)	2.97	3.01	10.86 (11.40)	0.96 (0.93)	597	12.45
	1.77 (1.61)	2.85 (2.73)		3.38 (3.10)			14.20 (14.86)	0.88 (0.89)		
N93	0	2.28 (2.28)	2.99	2.73 (2.64)	2.94	3.00	10.72 (11.38)	1.02 (0.97)	701	12.80
	1.73 (1.54)	2.69 (2.61)		3.15 (2.94)			14.15 (15.15)	0.93 (0.90)		
UIX	0	1.99 (1.98)	2.80	2.35 (2.24)	2.95	3.02	10.16 (11.08)	1.20 (1.11)	434	11.76
	1.72 (1.46)	2.36 (2.25)		2.73 (2.49)			13.61 (15.01)	1.08 (1.03)		

dependence of the maximum mass of static NSs on temperature is very weak for all the EOSs; however, finite temperature notably decreases the stability (both maximum frequencies and masses) of rotating models for all EOSs. The above considerations will be important when investigating the results of the merger simulations, since, as already investigated in Chapter 5, both high temperature (> 50 MeV) and very fast rotation (> 1 kHz) represent essential features of the merger remnant.

The total baryonic mass of the system represents an important quantity, and in the specific case of the GW170817 event the latter is determined according to

$$M_B^{\rm GW170817} \equiv 2M_B(M_G = 1.365M_\odot)\,, \tag{6.1}$$

which is also listed in the table together with the relevant value for the simulations presented in this chapter,

$$M_B^{\rm sim} \equiv 2M_B(M_G = 1.35M_\odot)\,. \tag{6.2}$$

This quantity depends only very weakly on the EOS, and by comparing the values of M_B, $M_B^{\rm sim}$, and $M_B^{\rm GW170817}$, some important qualitative conclusions can be already drawn: the BOB, V18, and (marginally) N93 EOSs would be able to sustain even a rigidly rotating hot remnant, whereas the softest UIX EOS would permit only a metastable differentially rotating one. Eventually, the cooling-down remnant would gain stability (not enough for UIX though), but in the long-term spindown, only the BOB EOS would be able to sustain a stable cold and static NS with a total baryonic mass of $M_B^{\rm sim}$ or $M_B^{\rm GW170817}$ (with the consideration that no mass is ejected). These are very simplistic considerations that will be contrasted now with the results of the merger simulations.

The simulations presented in this chapter are carried out using the setup described in Sec. 2.5.3 and also adopted in Chapter 5, the only notable difference with respect to the latter being the use of the HLLE Riemann solver, instead of LLF. In particular, 4 simulations of equal-mass BNS mergers, with $M = 1.35M_\odot$ for each component, performed using the fully tabulated versions of each EOS, are considered and studied in detail in the next paragraphs.

6.2 Numerical results

6.2.1 Stellar matter

All the simulations discussed here follow the remnant evolution for a period of at least 15 ms; as already done in Ch. 5, the time coordinate is set such that $t = t_{\rm merg} = 0$, where $t_{\rm merg}$ is the time of the merger and corresponds to the maximum of the GW amplitude. Noticeably, for all EOSs the merger simulations produce a metastable hypermassive NS which doesn't collapse during the considered time window, when the remnant is still stabilized by

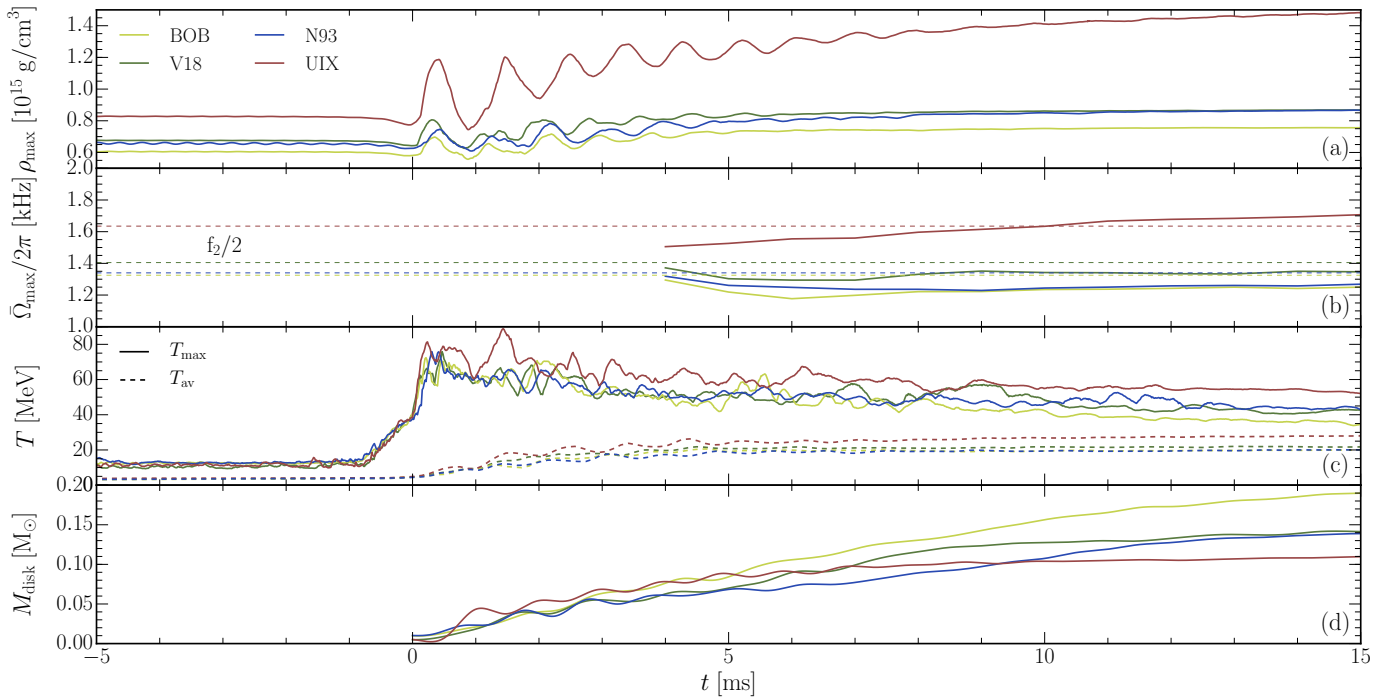

Figure 6.2 Profiles of the maximum values of rest-mass density (a) and azimuthally-averaged differential rotational frequency (b), maximum $T_{\rm max}$ and average $T_{\rm av}$ temperature (c), and disk mass (d) as a function of time for the four different simulated models.

differential rotation and finite temperature. This feature seems to be compatible with the multimessenger analysis of the GW170817 event.

As a first representative illustration, Fig. 6.2 shows the evolution of the maximum rest-mass density $\rho_{\rm max}$ (a), the maximum azimuthally-averaged differential rotation frequency $\bar{\Omega}_{\rm max}/2\pi$ (b), the maximum and averaged temperatures $T_{\rm max}$ and $T_{\rm av}$ (c), with the latter quantities evaluated in the $z = 0$ plane, and the disk mass (d). Interestingly, the simulations performed with the V18 and N93 EOSs lead to a remnant with $\rho_{\rm max}$ of about 0.9×10^{15} g/cm^{-3} and also similar maximum and average temperatures. The post-merger remnant modeled with the BOB EOS, the stiffest EOS in this sample, reaches the smallest maximum density and temperature, whereas the UIX case exhibits the typical increasing central density signature of a model reaching collapse a few tens of ms after the merger, in agreement with this EOS being the softest of the sample. The maximum mass of the mass-shedding

configuration shown in Table 6.1 is well below the actual mass in this case (as also better shown later); nevertheless this would require first a slowdown of differential rotation, and therefore a collapse hasn't be detected up to the maximum simulated time of about 15 ms.

Panel (b) of Fig. 6.2 shows the time development of the maximum of the azimuthally-averaged differential rotation frequency [210] on the equatorial plane (see Fig. 6.5),

$$\bar{\Omega}(r,t) \equiv \int_{t-\Delta t}^{t+\Delta t} dt' \int_{-\pi}^{\pi} d\phi \; \Omega(z=0,r,\phi,t') \tag{6.3}$$

with $\Delta t = 0.5$ ms. Values are sampled at each ms starting from 4 ms after the merger, as for earlier times the system is still too asymmetric.

While the BOB, V18, and N93 EOSs exhibit common features, UIX displays again a different trend. Indeed, while the profile for the UIX EOS shows an increasing instable behavior in the time window analyzed here, which is compatible with the increase of $\rho_{\rm max}$ discussed before, the other EOSs show stable profiles, thus indicating no slowdown of rotation within the milliseconds time interval simulated here. Therefore an eventual collapse with these EOSs, related to loss of stabilizing rotation, could occur only much later. Dashed horizontal lines shown in the same panel represent for each EOS the quadrupole peak frequency $f_2/2$, calculated as outlined in Appendix A, and determined via the PSDs shown in the next section. It is evident that the maximum differential rotation frequencies are systematically slightly lower than the f_2-related frequencies; this is not surprising, since the latter values are determined through PSDs considering also the first 4 ms, when the remnant is rotating faster.

All the simulations feature maximum temperatures remaining in general lower than 70 MeV; as already investigated in Chapter 5, however, maximum temperatures are reached only in local hot spots and do not represent the average status of stellar matter. In this regard, the density-weighted average temperature is calculated choosing again a density threshold of $\rho = 10^{13}$ g/cm^{-3}; the latter, comprised between 20 and 30 MeV for the entire EOS sample, is definitely lower than the corresponding maximum for each EOS.

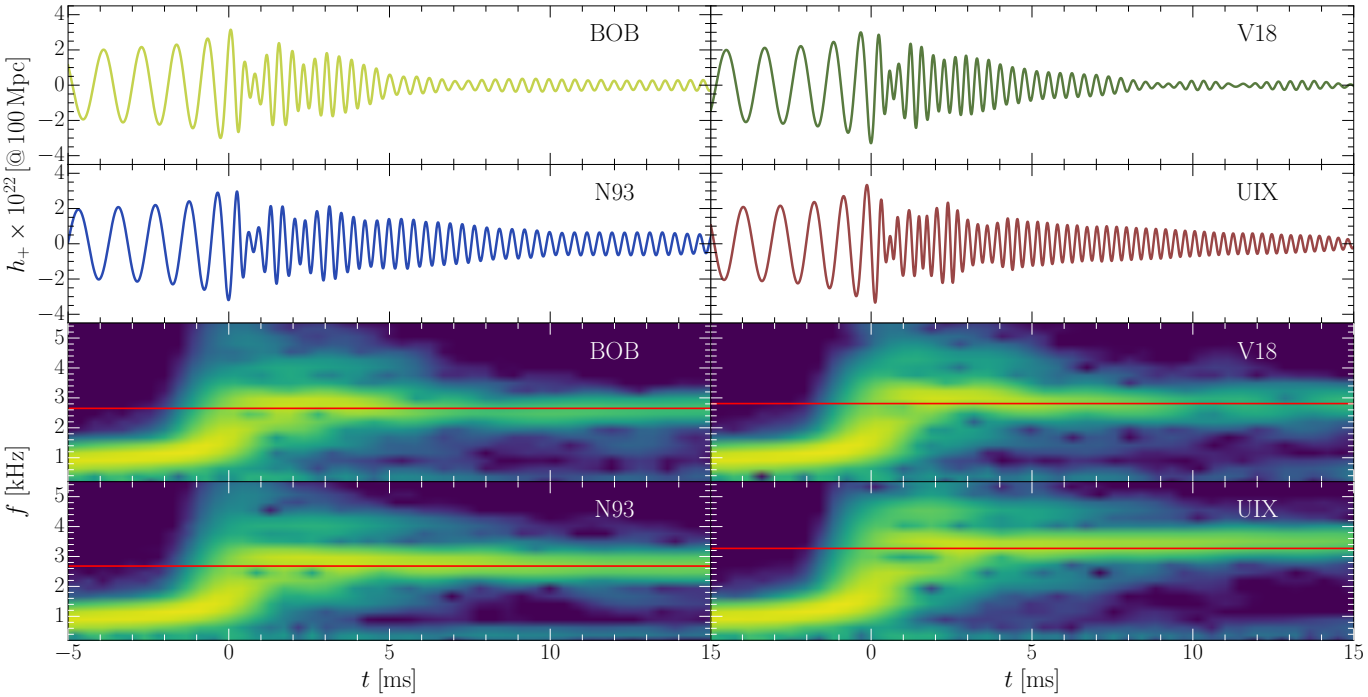

Figure 6.3 Upper panels: Plus polarization of the gravitational-wave strain for the four different models obtained for gravitational masses $2 \times 1.35 M_\odot$. Lower panels: spectrograms of the four analyzed cases. Red horizontal lines are representatives of the f_2 peak values for each case.

The disk mass $M_{\rm disk}$ is also monitored as function of time, shown in Fig. 6.2(d). In particular one can notice that during the short timespan of the simulations, the disk masses are still increasing, but tend to become stable at the end of the time evolution here reported, where they span a range comprised between 0.1 and 0.2 $M_\odot$, as also reported in Tab. 6.2. The softest UIX EOS attracts most material into the dense core and produces the lightest disk, contrary to the stiffest BOB model, which is instead responsible of a large $M_{\rm disk} \approx 0.2 M_\odot$.

6.2.2 Gravitational-wave properties

Fig. 6.3 shows the h_+ component of the gravitational wave strain for the four simulated models, up to the maximum simulated time after merger of 15 ms. Interestingly, the gravitational wave profile of the post-merger phase for V18 is different with respect to the one shown in Chapter 5, with differences likely being consequences of the use of the HLLE solver

instead of LLF. All models feature a maximum of the amplitude at approx. 15 ms from the beginning of the simulation, corresponding to 4 orbits ca. during the inspiral phase.

In order to better show the characteristic frequencies for the cases we have considered, Fig. 6.3 (lower panels) also includes the spectrograms of the four models. In order to compute the latters, the h_+ signals are first segmented in parts of $\approx$ 5 ms each and the spectra are calculated; a Blackman window is also applied to the segments, which are then overlapped by 90%, similarly to what done in Ref. [231]. It is evident that while after the merger different significative frequencies are present, including the f_1 and f_3 peaks (whose investigation is not reported here), the frequency related to the $l = m = 2$ mode (denoted in the plots with a red dashed line for each case) and its related f_2 peak is the only robust feature which remains present from the time of the merger to the end of the considered time window for all our models. In order to better investigate the typical frequencies for each model, once again, the PSD of the four models is computed and results are shown in Fig. 6.4; once again, for this study, the f_2 peak, calculated as reported in Appendix A, associated to the dominant $l = m = 2$ frequency is chosen as a tracker of the different behaviors.

The PSD confirms that the most compact and fastest rotating object is the one corresponding to the UIX EOS. The latter, characterized by the narrowest and most easy distinguishable peak of the sample, features indeed a f_2 frequency being more than 400 Hz higher than the other cases, which are localized in the range $2.6 - 2.8$ kHz.

The f_2 frequencies are reported, together with other relevant GW properties for each simulation, in Table 6.2; in particular, the maximum frequency $f_{\rm max}$, and the emitted GW energy $E_{\rm GW}$ for the $l = m = 2$ mode, both measured as outlined in Appendix A, are reported. For comparison, the values of f_2 according to universal relations between f_2 and the radius $R_{1.6}$ of a $1.6 M_\odot$ NS [232] or the tidal deformability parameter Λ [231], both given

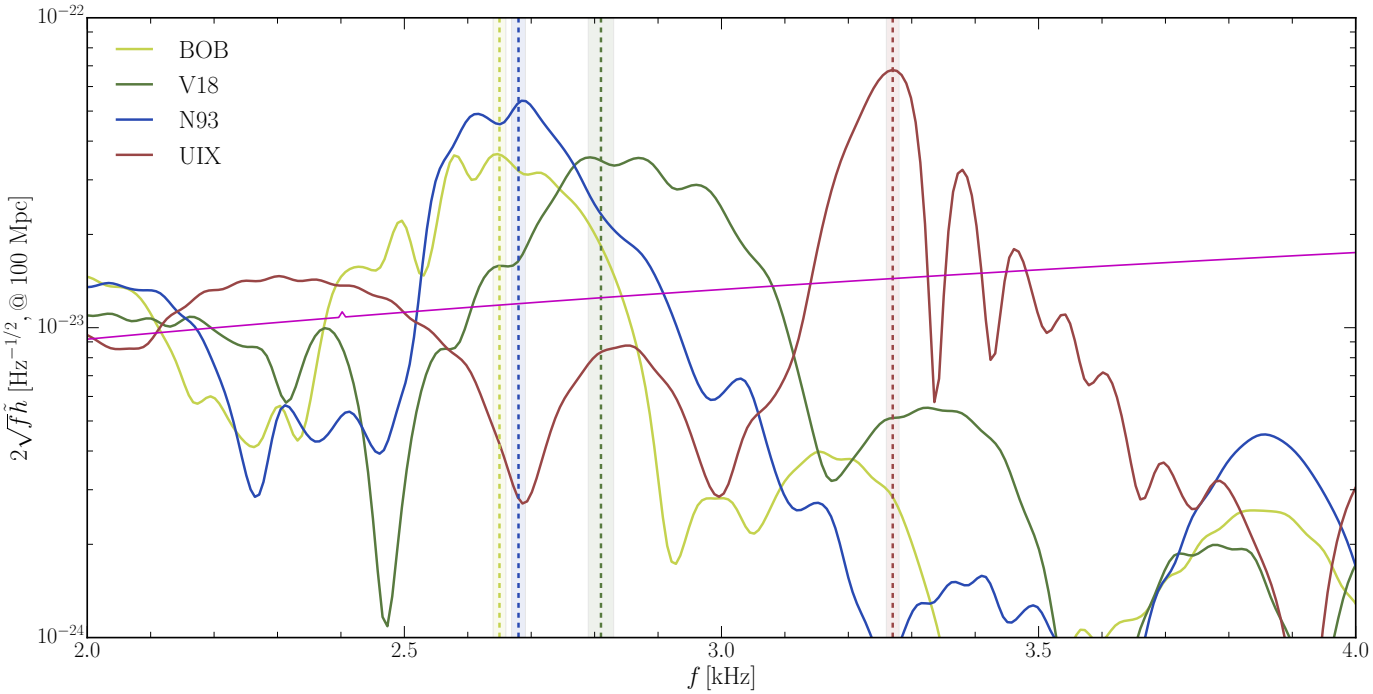

Figure 6.4 PSDs of the simulations with the different EOSs evaluated at a distance of 100 Mpc. Vertical dashed lines of different colors indicate the frequency of the main postmerger peak f2, with a shaded area of the same color representative of the estimated error. The sensitivity curve (magenta color) of Advanced LIGO is displayed for reference.

in Table 3.1, are also included in the table,

$$f_2[\mathrm{kHz}] \approx \begin{cases} 6.284 - 0.2823\, R_{1.6} & (f_2 < 2.8\ \mathrm{kHz}) \\ 8.713 - 0.4667\, R_{1.6} & (f_2 > 2.8\ \mathrm{kHz}) \end{cases} , \tag{6.4}$$

$$f_2[\mathrm{kHz}] \approx 5.832 - 0.8\, \Lambda^{1/5} . \tag{6.5}$$

A reasonable agreement (within 3%) is found, in particular for the first correlation with the radius, whereas the one with Λ is less pronounced with about 7% possible deviations, as in Ref. [231].

6.2.3 Masses and ejecta

Table 6.2 includes, for the instant $t = 15$ ms, the evaluated baryonic masses of the remnant M_{obj} and its disk M_{disk}, obtained by integrating the conserved rest-mass density over the 3D

Table 6.2 Properties of the simulated models: frequency of the f_2 peak, frequency at maximum amplitude $f_{\rm max}$, baryonic masses of the object $M_{\rm obj}$, the disk $M_{\rm disk}$, the ejected matter $M_{\rm ej}$ at $t = 15\,$ms, and the total emitted GW energy $E_{\rm GW}$. The f_2 values in brackets are obtained using the universal relations Eqs. (6.4, 6.5). The $M_{\rm disk}$ values in brackets are obtained using the universal relation Eq. (25) of [128].

EOS	f_2	$f_{\rm max}$	$E_{\rm GW}$	$M_{\rm obj}$	$M_{\rm disk}$	$M_{\rm ej}$
	[kHz]	[kHz]	[10^{52} erg]	[$M_\odot$]	[$M_\odot$]	[10^{-3} $M_\odot$]
BOB	2.65±0.01 (2.62,2.82)	1.68	4.10	2.76	0.189 (0.139)	3.7
V18	2.81±0.02 (2.90,2.96)	1.77	4.88	2.82	0.141 (0.093)	4.2
N93	2.68±0.01 (2.67,2.87)	1.68	5.99	2.81	0.138 (0.124)	4.5
UIX	3.27±0.01 (3.23,3.14)	1.91	7.69	2.85	0.109 (0.044)	7.4

domain,

$$M_B = \int d^3r \sqrt{\gamma}\, W \rho\,, \tag{6.6}$$

where γ represents the 3-metric determinant, W is the Lorentz factor and $\rho = 10^{13}$ g/cm^3 has been chosen as the boundary density between object and disk; such a prescription represents a common choice in literature (see, e.g., Ref. [239]).

Interestingly, lower limits on the disk mass of GW170817 derived from its electromagnetic counterpart are about $M_{\rm disk} \gtrsim 0.04 M_\odot$ [128, 216], with which all our EOSs would comply. An approximate universal relation between $M_{\rm disk}$ and Λ has been proposed in Ref. [128], and the related values are also included in Table 6.2. However, it can be seen that the deviations are very large, a feature which has also been pointed out in [216].

On the other hand, in order to measure the properties of the dynamical ejecta, multiple spherical detectors are considered at different radii around the origin; in particular, the detector at $200 M_\odot \approx 300$ km is chosen for the measurements reported here. In order to determine which of the material crossing this surface is effectively unbound, a threshold is set according to the geodesic criterion, as done, for example, in Refs. [240, 241]. In detail,

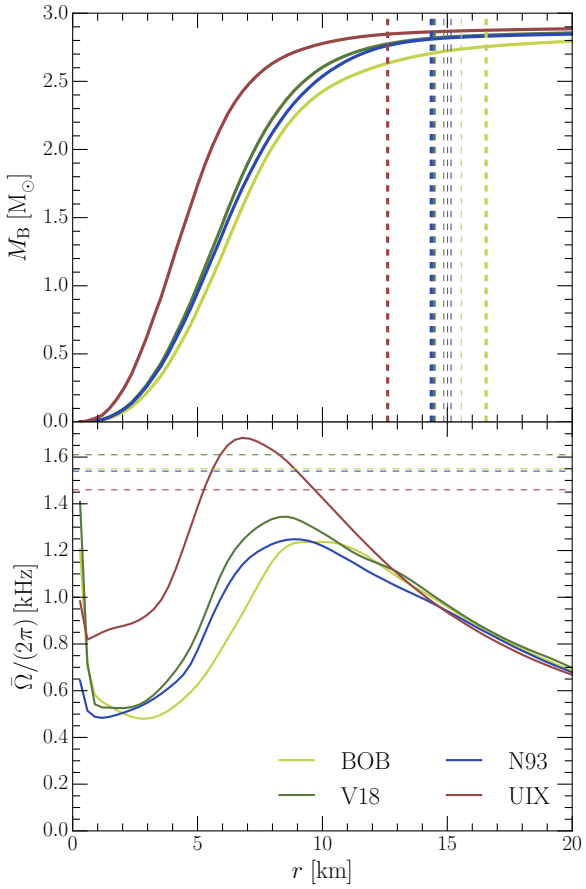

Figure 6.5 Enclosed baryonic mass M_B as a function of spherical radius r at $t = 15\,\mathrm{ms}$ for the different EOSs (upper panel); thick dashed lines denote radii corresponding to M_{obj} in Table 6.2. Thin dashed lines are the radii of $T = 50$ MeV M_{max} Kepler configurations in Table 6.1.
The average angular velocity is also represented as a function of the radial cylindrical coordinate r (at $z = 0$) at $t = 15\,\mathrm{ms}$ (lower panel).

a particle on geodesics is considered to be unbound if the covariant time component of the fluid four-velocity u satisfies $u_t \leq -1$ (see, e.g., Ref. [242] for a discussion on the method).

Before analyzing in details the properties of the ejected component, it is interesting to focus on the post-merger remnant and investigate its features. Fig. 6.5 shows the profiles of the enclosed baryonic mass M_B as a function of the spherical radius r at $t = 15\,\mathrm{ms}$ after the merger (upper panel); such a calculation is carried out for the four models discussed here by computing volume integrals of the conserved rest-mass density D up to each different radius r. A thick dashed vertical line denotes the M_{obj} position for every investigated case,

according to Table 6.2 (although due to the density-cutoff procedure $M_{\rm obj}$ is not the mass of a spherical object). Again, the V18 and N93 EOSs lead to very similar profiles, as also for other global properties in Table 6.1. Thin dashed vertical lines indicate the radii of the $T = 50$ MeV Kepler configurations (Table 6.1) for a qualitative comparison. One can note that the UIX remnant radius at $t = 15$ ms is significantly smaller than the one of stable Kepler rotation, which points again to the commencing collapse of this object.

In Fig. 6.5 (lower panel), the angular velocity profiles for the four remnants are shown; in particular, these profiles are obtained with the standard technique already outlined in Chapter 5 (averages are performed in the azimuthal direction on the equatorial plane ($z = 0$) and then also over a time window of 1 ms at $t = 15$ ms so as to obtain functions that depend only on the cylindrical radius r from the center of the grid). Maximal values are reached for all the EOSs at approximately $r = 8$ km, roughly overlapping with the position where the two hot spots appear [210]; unsurprisingly, the maximum reached value is highest for the UIX EOS, whose profile is also generally larger with respect to the other EOSs, compatibly with what shown before in the PSD distributions. This last feature is compatible with the profiles shown in Fig. 6.2 and with this remnant being on the verge of collapse. It also interesting to point out that the profiles obtained for these EOSs are in agreement with results reported in literature related to other EOSs (see, e.g., [210, 217]). Also in this panel, horizontal dashed lines denote the Kepler frequencies of the $T = 50$ MeV $M_{\rm max}$ configurations for a qualitative comparison.

As previously mentioned, a detailed study is carried out with respect to the properties of the dynamical ejecta in Fig. 6.6; in particular, the mass ejection dependence on the polar angle is represented in panel (a); here, $0^{\rm o}$ refers to the z axis, while $90^{\rm o}$ is representative of the equatiorial plane. The dependence on the velocity ratio v/c, the electron fraction Y_e and the specific entropy s are instead reported in panels (b), (c) and (d) respectively. In particular, the specific entropy (which is directly related to the temperature of the ejected matter), the velocity and the electron fraction represent the most important quantities in

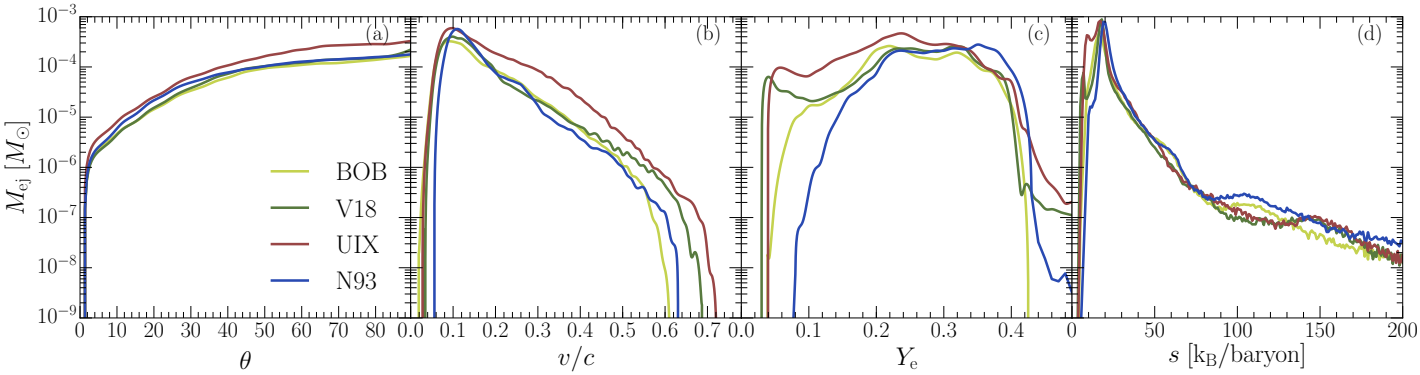

Figure 6.6 Distribution of the ejected mass as function of the polar angle θ (first panel), velocity ratio v/c (second panel), electron fraction Y_e (third panel), and specific entropy s (fourth panel).

order to characterize the r-process nucleosynthesis in the outflows.

It is evident that the emission increases almost monotonically with the polar angle for all the cases considered here, and this behavior is particularly evident up to about 50°, while the curves remain approximately constant for angles above this threshold. Fig. 6.6, panel (a), shows in particular that the tidal disruption of matter generates ejecta which are mostly distributed close to the equatorial plane (the latters are also labeled as equatorial ejecta, as in [243]). The velocity distribution (or, correspondingly, the kinetic energy distribution) shows common features for all the cases we analyze: in particular, a clear peak at $v/c \approx 0.1$ is present, after which the distribution decreases up to values between 0.6 and 0.75, a feature which is compatible with the cases analyzed in Ref. [239], where different EOSs were considered. The electron fraction represents a crucial parameter in order to determine which elements can be created by the r-process; indeed, heavy elements ($A \gtrsim 120$) are created via neutron-rich ejecta ($Y_e \lesssim 0.25$) [243, 244], whereas neutron-poor ejecta produce elements with lower masses. Different Y_e distributions also have an impact on the kilonova signal, since neutron-rich ejecta favor the so-called "red" kilonovae, peaking in the infrared, while neutron-poor ejecta produce "blue" kilonovae [245]. For our set of EOSs, the ejecta distributions start at about $Y_e = 0.04$ (with the only notable exception of N93, whose distribution arises starting from $Y_e = 0.08$) with the UIX and V18 models characterized a

local maximum at the same point; for all our cases, the distributions cover a wide range of Y_e, a feature which is related to the presence of neutrino treatment in our simulations (see, e.g., Ref. [127] for further details) which redistributes the electron number due to weak interactions. The study of the specific entropy, which, as pointed out in Ref. [240] has a close connection with the shock heated matter in the ejecta, shows that for all our EOSs, a major fraction of the ejecta is characterized by low temperatures. Interestingly, all our cases show a prominent peak corresponding to $s \sim 20\ k_{\rm B}$/baryon followed by a drop to $M_{ej} \approx 10^{-6}$ at about $s \sim 50\ k_{\rm B}$/baryon. In summary, the results presented here are consistent with what reported in literature for simulations carried out using different finite-temperature EOSs; further systematic studies, incorporating the sample investigated here into a larger one, represent an important step forward and may outline quasi-universal behaviors.

CHAPTER 7

THE FCCZ4 FORMULATION OF THE EINSTEIN FIELD EQUATIONS

The merger simulations presented in this thesis work are performed, as discussed in Sec. 2.5.3 and as a common approach in numerical relativity, adopting the CCZ4 formulation of the Einstein field equations and employing an AMR approach in cartesian coordinates. Of course, the use of such coordinates comes with many advantages, one of which being the great simplification of the equations. The use of these coordinates, however, doesn't allow to exploit the symmetries which the simulated objects have; the use of spherical and spherical-like coordinates, for example, is better suited in order to simulate the post-merger object, and exploit its symmetries. In this context, the creation of an optimized code which solves the Einstein equations in arbitrary coordinates represents an important step forward; the use of a formulation which also includes constraint damping capabilities adds a further advantage to such a method. Indeed, such a formulation has already been developed and is known in literature as the fCCZ4 formulation [11]. This chapter will focus on the creation of a code which solves the spacetime equations using this formulation, and the presentation of the results and tests carried out. The implementation presented here is heavily inspired

by the work carried out by Baumgarte et al. [246, 247].

7.1 Numerical methods

7.1.1 Rescaling procedure and reference metric approach

The employment of curvilinear coordinates inevitably introduces a number of numerical problems, absent in cartesian coordinates, which have to be dealt with. In this regard, coordinate singularities represent a first example of such problems. Let $\mathbf{V}$ be a vector whose cartesian components V^i are smooth everywhere; its components in a curvilinear coordinate system, let it be spherical for simplicity, V^a, are easily obtained according to

$$V^a = \Lambda^a_i V^i \,, \tag{7.1}$$

where Λ^a_i is the Jacobian matrix of the coordinate transformation.

Since the coordinate transformation to spherical coordinates introduces factors $\sim 1/r$ and $\sim 1/rsin\theta$, the new components are not regular everywhere anymore. Indeed, these terms lead to divergences when evaluated in correspondence of the origin or the polar axis. Such a problem can be easily solved by shifting the numerical grid, in order to not evaluate tensor components on the origin or the polar axis; when solving the Einstein field equations, however, since first and second derivatives of the variables have to be evaluated, the usual strategies for numerical approximation of these derivatives (e.g., finite difference methods) will still be impacted by the divergences and this generally leads to errors which will grow in time, spoiling the evolution. This interesting problem has been noticed and solved by the authors of the SENR/NRPy+ code [247]; in their implementation, indeed, they use a different approach for computing the derivatives of the problematic factors. The strategy exploits the fact that these factors, also called *scale factors*, only depend on the chosen coordinate system, so their exact derivatives are known a priori. It can be easily shown that

a generic vector component can be written as

$$\beta^i = s^i \odot \underline{\beta}^i \,, \tag{7.2}$$

where s^i represents the i-th component of the scale factor vector $\mathbf{s}$, which, as an example, can be written in spherical coordinates as

$$\boldsymbol{s} = \begin{pmatrix} 1 \\ \frac{1}{r} \\ \frac{1}{r sin\theta} \end{pmatrix} \,, \tag{7.3}$$

the $\odot$ symbol represents the Hadamard product between matrices and the underlined vector of regular components $\underline{\beta}^i$ is the rescaled form of the starting vector. With this approach, one can derive a generic vector by applying the Leibniz rule of the product between the scale factor vector and the rescaled vector, where the derivatives of the scale factors are computed exactly and the derivatives of the smooth, rescaled vector components can still be computed by using, e.g., finite differences. It is also easy to show that this rescaling approach can be extended to generic one-vectors and rank-2 tensors.

A second important ingredient of this formalism is related to the introduction of a *reference metric approach*. After having introduced a conformally related metric, as done in the usual BSSN and CCZ4 approaches, one can write it as a sum of the dynamic spacetime metric and the background, flat one (the *reference metric*), in order to decouple the two contributions:

$$\tilde{\gamma}_{ij} = \hat{\gamma}_{ij} + \epsilon_{ij} \,, \tag{7.4}$$

where $\hat{\gamma}_{ij}$ represents the reference metric and ϵ_{ij} is instead the unrescaled, dynamic part of the metric, which can be also interpreted as a perturbative contribution (which does not need to be small) to the flat background[1]. Again, the main advantage of this method is seen when evaluating the first and second derivatives of the metric, since the latters can be

[1]The notation used here is the same introduced in Ref. [12].

evaluated exactly for the flat metric and the usual rescaling approach can be adopted for the perturbation metric tensor, so that $\epsilon_{ij} = s_{ij} \odot h_{ij}$ where s_{ij} represents the generic component of the scale factor tensor with lower indices, and h_{ij} is the rescaled perturbation tensor. As an example, the derivative $\tilde{\gamma}_{ij,k}$ is calculated as follows:

$$\tilde{\gamma}_{ij,k} = \hat{\gamma}_{ij,k} + s_{ij,k} \odot h_{ij} + s_{ij} \odot h_{ij,k} \,, \tag{7.5}$$

where the derivatives $\hat{\gamma}_{ij,k}$ and $s_{ij,k}$ are calculated exactly and $h_{ij,k}$ is evaluated with finite differences. Interestingly, a generalization of the Hadamard product appears here, involving tensors with different ranks ($s_{ij,k}$ and h_{ij}); the product is still well defined, and results in a new tensor $a_{ij,k}$ whose ij component, at every fixed k, is given by the usual Hadamard product between the two initial tensors. The code presented here adopts, in particular, fourth-order central finite differences for all the spatial derivatives, with the exception of shift-multiplying derivatives, for which second-order upwind finite differences are chosen.

In this implementation, Brown's lagrangian choice [248] is assumed, i.e.

$$\partial_t \tilde{\gamma} = 0 \,, \tag{7.6}$$

where $\tilde{\gamma}$ represents the conformal metric determinant. In the case of conformally flat initial data, this assumption corresponds to constraining $\tilde{\gamma} = \hat{\gamma}$ throughout the time evolution of the system.

7.1.2 Inner ghost zones

Curvilinear coordinates introduce a further complication with respect to cartesian coordinates, due to the introduction of *inner boundaries*. In the representative case of spherical coordinates, indeed, one can generally use common extrapolation techniques in order to fill the outer ghost zone, which collects here all the points whose radial coordinate $r > R$, where R is the maximum extent of the grid on the radial direction; since radial derivatives are to be evaluated also for the points located in the immediate proximities of the origin, however,

finite differences require the values of variables on points virtually located at negative r (a similar situation happens for derivatives in the polar direction evaluated near the polar axis). This gives rise to the necessity of an inner ghost zone. Interestingly, such a ghost zone can be populated starting from the values the variables assume in certain points of the actual numerical domain [246]. In particular, Ref. [12] has shown in details that the correspondences are given (in the usual representative case of spherical coordinates) by

$$\alpha(-r,\theta,\phi) = \alpha(r,\pi-\theta,\phi+\pi)\,, \tag{7.7}$$

$$\alpha(r,-\theta,\phi) = \alpha(r,\theta,\phi+\pi)\,, \tag{7.8}$$

$$\alpha(r,\pi+\theta,\phi) = \alpha(r,\pi-\theta,\phi+\pi)\,, \tag{7.9}$$

$$\alpha(r,\theta,\phi+2\pi) = \alpha(r,\theta,\phi)\,, \tag{7.10}$$

where α represents a generic scalar field and Eq. (7.10) is simply a result of the periodicity on the azimuthal direction. The procedure illustrated here is used to fill the inner ghost zones for every scalar field appearing in the set of differential equations; however, for components of vectors and tensors, this copy can't be performed as for scalars. Indeed, one should take into account that the unit vectors of a ghost zone point may point to the opposite direction with respect to the interior point corresponding to the ghost zone point considered. The solution here implemented in order to solve this problem consists in implementing the *parity conditions* presented in Ref. [246]; in details, when copied, vector components are multiplied by the corresponding sign according to Table 7.1, whereas the sign of rank-2 tensor components is obtained by multiplying the sign corresponding to the interested components.

7.1.3 Time-step considerations

A further important remark regards the time evolution procedure. The code presented here adopts the Method of Lines (MoL): spatial derivatives are discretized while the time variable is left continuous. An explicit fourth order Runge-Kutta method (RK4) is then employed in

Table 7.1 Parity conditions for vector and tensor components for spherical-like and cylindrical-like coordinates; adapted from Ref. [247]. The label "radial" refers to the parity across the origin ($r = 0$) in spherical coordinates, whereas "axial" describes the parity across the polar axis ($sin\theta = 0$) in spherical coordinates and the origin ($\rho = 0$) in cylindrical coordinates.

Coordinates	Component	Radial	Axial
Spherical-like	r	$-$	$+$
	θ	$+$	$-$
	ϕ	$-$	$-$
Cylindrical-like	ρ		$-$
	ϕ		$-$
	z		$+$

order to integrate the evolution equations. In this procedure, the actual timestep is calculated according to the Courant-Friedrichs-Lewy (CFL) condition. In cartesian coordinates, the latter is rather immediate to implement: in particular, assuming that for the minimum spatial displacement $\Delta x = \Delta y = \Delta z$, then $\Delta t = C\Delta x$ where C is the Courant factor. For curvilinear coordinates, however, identifying Δt is less straightforward: considering the usual example of a spherical coordinates unigrid, the timestep due to the CFL condition is given by:

$$\Delta t = C\mathrm{min}[\Delta \mathrm{r}, \mathrm{r}\Delta\theta, \mathrm{rsin}\theta\Delta\phi]\,. \tag{7.11}$$

Interestingly, while in cartesian coordinates Δt was proportional to a length (Δx), here the timestep is proportional to a volume, since the minimum of the indicated bracket has the form $\approx \Delta r\Delta\theta\Delta\phi$. The overall consequence manifests when using a high number of azimuthal cells, since the CFL restriction can determine a very small Δt thus making the time evolution unfeasible. A number of solutions do exist in order to circumvent the problem (see, e.g., Ref. [13] for a discussion), but no particular solution has been adopted yet for the implementation discussed here, since all the tests are performed in the assumption of

appropriate symmetries.

7.1.4 General notes

The solver presented here implements the previously discussed techniques in order to solve the Einstein field equations in generic coordinate systems. The code can be used standalone: it implements the grid structure, appropriately fills inner and outer ghost zones and solves the Einstein field equations in their fCCZ4 (or also simply BSSN) formulation, presented in the next chapters, at every timestep. A fundamental characteristic of the solver is its flexibility for working with different curvilinear coordinates: it is very simple to both switch between different implemented coordinate systems and also implement new systems. Indeed, the entirety of the information related to each coordinate system is reduced to the specification of the metric tensor (which consequently determines the scale factor tensors) and the ghost zone prescriptions (which are currently implemented for cartesian, spherical and cylindrical coordinates).

In its current form, the solver already includes cartesian, cylindrical, spherical and sinhspherical coordinates. The latter choice, also implemented in the NRPy+/SENR code, consists in a distribution of the grid points in the radial direction according to $f(r) = A\text{sinh}(r/w)$, where A and w are both constants, thus leaving the polar and azimuthal distributions unchanged with respect to the usual spherical coordinates. Such a choice of coordinates represents a step forward with respect to simple spherical coordinates, since it introduces a unigrid with logarithmically distributed radial coordinate, thus providing an increased resolution in the proximities of the origin which decreases when moving away from it.

The code heavily relies on the `TensorTemplates` library [249], which implements tensor class templates with various operations on them defined. The library is particularly suitable for the implementation of the fCCZ4 formulation of the Einstein equations, making it possible

to simply calculate, e.g., multiple indices contractions, reorderings, sums and the Hadamard products between tensors.

7.2 The fCCZ4 equations

Before discussing the fCCZ4 equations in detail, it is useful to report first the BSSN formulation in the same reference metric approach, so to easily make comparisons and understand how the constraint damping feature impacts the set of equations. Using the same notation as in Sec. 2.5.1, the equations read:

$$\partial_t \tilde{\gamma}_{ij} = [\beta^k \partial_k \tilde{\gamma}_{ij} + \partial_i \beta^k \tilde{\gamma}_{kj} + \partial_j \beta^k \tilde{\gamma}_{ik}] + \frac{2}{3}\tilde{\gamma}_{ij}(\alpha \tilde{A}^k_k - \tilde{D}_k \beta^k) - 2\alpha \tilde{A}_{ij} \,, \tag{7.12}$$

$$\partial_t \phi = [\beta^k \partial_k \phi] + \frac{1}{6}(\tilde{D}_k \beta^k - \alpha K) \,, \tag{7.13}$$

$$\begin{aligned} \partial_t \tilde{A}_{ij} = {} & [\beta^k \partial_k \tilde{A}_{ij} + \partial_i \beta^k \tilde{A}_{kj} + \partial_j \beta^k \tilde{A}_{ik}] - \frac{2}{3}\tilde{A}_{ij}\tilde{D}_k \beta^k - 2\alpha \tilde{A}_{ik}\tilde{A}^k_j + \alpha \tilde{A}_{ij} K \\ & + e^{-4\phi}[-2\alpha \tilde{D}_i \tilde{D}_j \phi + 4\alpha \tilde{D}_i \phi \tilde{D}_j \phi + 4\tilde{D}_{(i}\alpha \tilde{D}_{j)}\phi - \tilde{D}_i \tilde{D}_j \alpha + \alpha \tilde{R}_{ij}]^{TF} \,, \end{aligned} \tag{7.14}$$

$$\partial_t K = \left[\beta^k \partial_k K\right] + \frac{1}{3}\alpha K^2 + \alpha \tilde{A}_{ij}\tilde{A}^{ij} - e^{-4\phi}\left(\tilde{D}_i \tilde{D}^i \alpha + 2\tilde{D}^i \alpha \tilde{D}_i \phi\right) \,, \tag{7.15}$$

$$\begin{aligned} \partial_t \tilde{\Lambda}^i = {} & \left[\beta^k \partial_k \tilde{\Lambda}^i - \partial_k \beta^i \tilde{\Lambda}^k\right] + \tilde{\gamma}^{jk}\hat{D}_j \hat{D}_k \beta^i + \frac{2}{3}\Delta^i \tilde{D}_j \beta^j + \frac{1}{3}\tilde{D}^i \tilde{D}_j \beta^j \\ & - 2\tilde{A}^{ij}\left(\partial_j \alpha - 6\alpha \partial_j \phi\right) + 2\alpha \tilde{A}^{jk}\Delta^i_{jk} - \frac{4}{3}\alpha \tilde{\gamma}^{ij}\partial_j K \,, \end{aligned} \tag{7.16}$$

$$\partial_t \alpha = \left[\beta^i \partial_i \alpha\right] - 2\alpha K \,, \tag{7.17}$$

$$\partial_t \beta^i = \left[\beta^j \partial_j \beta^i\right] + B^i \,, \tag{7.18}$$

$$\partial_t B^i = \left[\beta^j \partial_j B^i\right] + \frac{3}{4}\partial_0 \tilde{\Lambda}^i - \eta B^i \,, \tag{7.19}$$

where the gauge equations for the lapse function α (the "1+log" condition [98],) and the shift vector (the Gamma-driving condition [250]) are also included; in this context, B^i represents an auxiliary vector, and η is a damping parameter [251]. The set of equations included here shows differences with respect to the BSSN set discussed in Sec. 2.5.1, which referred to cartesian coordinates only. Indeed, since the Christoffel symbols aren't identically

zero in this approach, they can't be neglected and appear in the equations via covariant derivatives replacing former partial ones. Interestingly, the conformal connection functions are also affected; indeed, the new functions $\tilde{\Lambda}^i$ substitute $\tilde{\Gamma}^i$ as independent variables evolved in this formulation. Such functions are set at $t = 0$ to be

$$\tilde{\Lambda}^i = \Delta^i = \tilde{\gamma}^{jk}\Delta^i_{jk} = \tilde{\gamma}^{jk}(\tilde{\Gamma}^i_{jk} - \hat{\Gamma}^i_{jk})\,, \tag{7.20}$$

where $\tilde{\Gamma}^i_{jk}$ and $\hat{\Gamma}^i_{jk}$ respectively represent the Christoffel symbols related to the conformal and the reference metric.

This formulation features the dynamical enforcement of the trace-free condition $\tilde{\gamma}^{ij}\tilde{A}_{ij} = 0$ since the latter can be violated numerically throughout the time evolution. This operation is carried out by adding the term proportional to $\tilde{A}^k_k$ in the evolution equation for $\tilde{\gamma}_{ij}$ [248]. The equations also do not show matter terms, as the system is solved for vacuum spacetimes.

It is important to remark that, although the set of BSSN variables appearing in the equations is represented by $\{\tilde{\gamma}_{ij}, \phi, \tilde{A}_{ij}, K, \tilde{\Lambda}^i, \alpha, \beta^i, B^i\}$, the set of evolved variables is, according to the rescaling procedure described in Sec. 7.1.1, $\{h_{ij}, \phi, a_{ij}, K, \lambda^i, \alpha, \underline{\beta}^i, \underline{B}^i\}$, where the new tensors and vectors are defined according to:

$$\tilde{\gamma}_{ij} = \hat{\gamma}_{ij} + s_{ij} \odot h_{ij}\,, \tag{7.21}$$

$$\tilde{A}_{ij} = s_{ij} \odot a_{ij}\,, \tag{7.22}$$

$$\tilde{\Lambda}^i = s^i \odot \lambda^i\,, \tag{7.23}$$

$$\beta^i = s^i \odot \underline{\beta}^i\,, \tag{7.24}$$

$$B^i = s^i \odot \underline{B}^i\,. \tag{7.25}$$

After each timestep, the unrescaled variables are again determined via the usual Hadamard product.

The Z4 constraint damped system modifies the Einstein equations according to Eq. (2.55), and leads to the following set of equations [11]

$$\partial_t \tilde{\gamma}_{ij} = [\beta^k \partial_k \tilde{\gamma}_{ij} + \partial_i \beta^k \tilde{\gamma}_{kj} + \partial_j \beta^k \tilde{\gamma}_{ik}] + \frac{2}{3}\tilde{\gamma}_{ij}(\alpha \tilde{A}^k_k - \tilde{D}_k \beta^k) - 2\alpha \tilde{A}_{ij}\,, \tag{7.26}$$

$$\partial_t \phi = [\beta^k \partial_k \phi] + \frac{1}{6}(\tilde{D}_k \beta^k - \alpha K)\,, \tag{7.27}$$

$$\begin{aligned}\partial_t \tilde{A}_{ij} = {} & [\beta^k \partial_k \tilde{A}_{ij} + \partial_i \beta^k \tilde{A}_{kj} + \partial_j \beta^k \tilde{A}_{ik}] - \frac{2}{3}\tilde{A}_{ij}\tilde{D}_k \beta^k - 2\alpha \tilde{A}_{ik}\tilde{A}^k_j + \alpha \tilde{A}_{ij}(K - 2\Theta) \\ & + e^{-4\phi}[-2\alpha \tilde{D}_i \tilde{D}_j \phi + 4\alpha \tilde{D}_i \phi \tilde{D}_j \phi + 4\tilde{D}_{(i}\alpha \tilde{D}_{j)}\phi - \tilde{D}_i \tilde{D}_j \alpha + \alpha(\tilde{R}_{ij} + D_i Z_j + D_j Z_i)]^{TF}\,,\end{aligned} \tag{7.28}$$

$$\begin{aligned}\partial_t K = {} & \left[\beta^k \partial_k K\right] + e^{-4\phi}[\alpha(\tilde{R} - 8\tilde{D}^i \phi \tilde{D}_i \phi - 8\tilde{D}^2 \phi) - (2\tilde{D}^i \alpha \tilde{D}_i \phi + \tilde{D}^2 \alpha)] \\ & + \alpha(K^2 - 2\Theta K) + 2\alpha D_i Z^i - 3\alpha k_1(1 + k_2)\Theta\,,\end{aligned} \tag{7.29}$$

$$\begin{aligned}\partial_t \Theta = {} & \left[\beta^k \partial_k \Theta\right] + \frac{1}{2}\alpha[e^{-4\phi}(\tilde{R} - 8\tilde{D}^i \phi \tilde{D}_i \phi - 8\tilde{D}^2 \phi) - \tilde{A}^{ij}\tilde{A}_{ij} + \frac{2}{3}K^2 \\ & - 2\Theta K + 2D_i Z^i] - Z^i \partial_i \alpha - \alpha k_1(2 + k_2)\Theta\,,\end{aligned} \tag{7.30}$$

$$\begin{aligned}\partial_t \tilde{\Lambda}^i = {} & \left[\beta^k \partial_k \tilde{\Lambda}^i - \partial_k \beta^i \tilde{\Lambda}^k\right] + \tilde{\gamma}^{jk}\hat{D}_j \hat{D}_k \beta^i + \frac{2}{3}\Delta^i \tilde{D}_j \beta^j + \frac{1}{3}\tilde{D}^i \tilde{D}_j \beta^j \\ & - 2\tilde{A}^{ij}\left(\partial_j \alpha - 6\alpha \partial_j \phi\right) + 2\alpha \tilde{A}^{jk}\Delta^i_{jk} - \frac{4}{3}\alpha \tilde{\gamma}^{ij}\partial_j K \\ & + 2\tilde{\gamma}^{ij}(\alpha \partial_j \Theta - \Theta \partial_j \alpha - \frac{2}{3}\alpha K Z_j) - 2\alpha k_1 \tilde{\gamma}^{ij} Z_j\,,\end{aligned} \tag{7.31}$$

$$\partial_t \alpha = \left[\beta^i \partial_i \alpha\right] - 2\alpha(K - 2\Theta)\,, \tag{7.32}$$

$$\partial_t \beta^i = \left[\beta^j \partial_j \beta^i\right] + B^i\,, \tag{7.33}$$

$$\partial_t B^i = \left[\beta^j \partial_j B^i\right] + \frac{3}{4}\partial_0 \tilde{\Lambda}^i - \eta B^i\,, \tag{7.34}$$

Differently from BSSN, the new conformal connection functions are defined according to

$$\tilde{\Lambda}^i \equiv \Delta^i + 2\tilde{\gamma}^{ij} Z_j\,. \tag{7.35}$$

While this new definition does not change the initial prescription for $\tilde{\Lambda}^i$, which is still set according to Eq. (7.20), it is useful to determine the $\boldsymbol{Z}$ vector; the latter is not an evolved

variable but is recovered after each step according to

$$Z^i = \frac{1}{2} e^{-4\phi} (\tilde{\Lambda}^i - \Delta^i) \,. \tag{7.36}$$

In this formulation, the conformal Ricci tensor can be explicitly written as follows:

$$\begin{aligned} \tilde{R}_{ij} = & -\frac{1}{2} \tilde{\gamma}^{kl} \hat{D}_k \hat{D}_l \tilde{\gamma}_{ij} + \tilde{\gamma}_{k(i} \hat{D}_{j)} \Delta^k + \Delta^k \Delta_{(ij)k} \\ & + \tilde{\gamma}^{kl} \left(2\Delta^m_{k(i} \Delta_{j)ml} + \Delta^m_{ik} \Delta_{mjl} \right) \,, \end{aligned} \tag{7.37}$$

where the first term of the right hand side effectively reduces to $-\frac{1}{2}\tilde{\gamma}^{kl}\hat{D}_k\hat{D}_l\epsilon_{ij}$ since the covariant derivative with respect to the reference metric applied to the reference metric itself is zero.

Finally, in the case of a constraint-fulfilling solution of the Einstein equations, i.e. when $\theta = Z^i = 0$, the Hamiltonian and Momentum constraints assume the following form:

$$H = \frac{2}{3} K^2 - \tilde{A}_{ij} \tilde{A}^{ij} + e^{-4\phi} (\tilde{R} - 8\tilde{D}^i \phi \tilde{D}_i \phi - 8\tilde{D}^2 \phi) = 0 \,, \tag{7.38}$$

$$M^i = e^{-4\phi} \left[\frac{1}{\sqrt{\tilde{\gamma}}} \hat{D}_j (\sqrt{\tilde{\gamma}} \tilde{A}^{ij}) + 6\tilde{A}^{ij} \partial_j \phi - \frac{2}{3} \tilde{\gamma}^{ij} \partial_j K + \tilde{A}^{jk} \Delta^i_{jk} \right] = 0 \,, \tag{7.39}$$

The evaluation of the ∞-norm or the L2-norm of the constraints at each timestep represents a possible way to check whether the code is stable or not, and it will be used in order to investigate the cases and tests presented here. Furthermore, when indicated, comparisons are also performed with respect to the public NRPy+ code.

7.3 Tests and results

7.3.1 Gauge wave testbed

As a first test, a standard sinusoidal gauge wave is evolved in cartesian coordinates (see Ref. [252] and references therein) in such a way that the wave propagates only along the x-direction. The problem consists in evolving a spacetime whose 4-metric is represented by

$$ds^2 = -H dt^2 + H dx^2 + dy^2 + dz^2 \,, \tag{7.40}$$

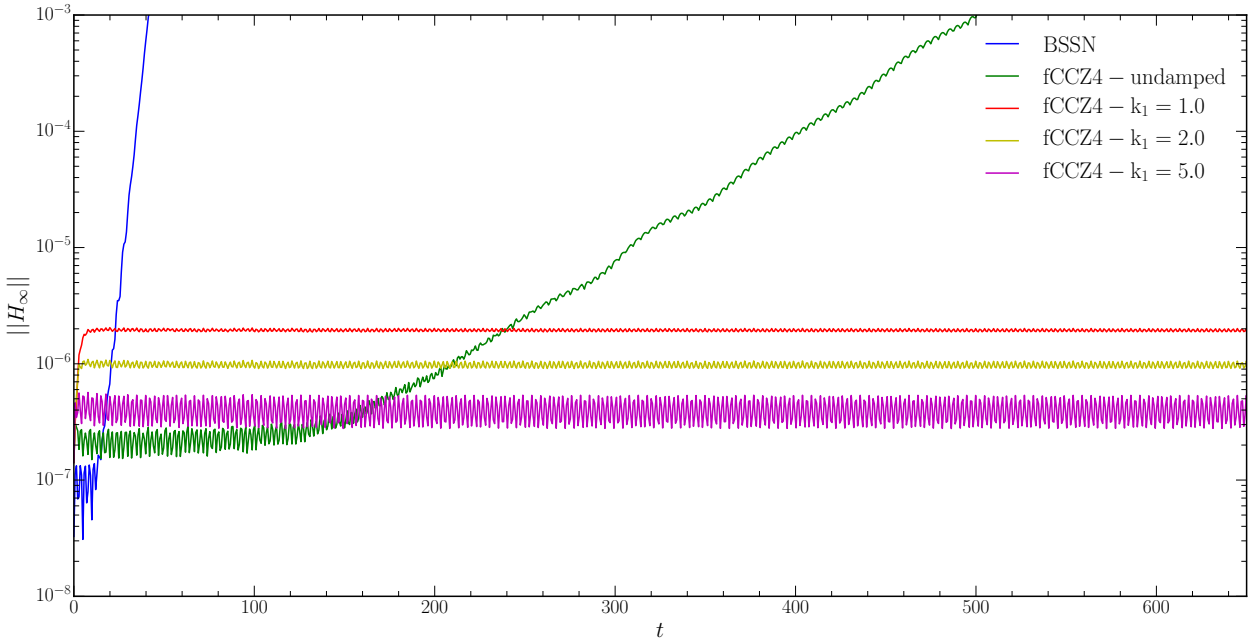

Figure 7.1 L∞-norm of the Hamiltonian constraint violation with respect to time for the sinusoidal gauge wave test evolved in the BSSN and fCCZ4 formulations. For the latter, different choices of the damping parameter k_1 are shown.

where, at $t = 0$, H is given by:

$$H = 1 + Asin\left(\frac{2\pi x}{d}\right) . \tag{7.41}$$

The initial data, with respect to the formalism used here, lead to the following prescriptions:

$$\alpha = \sqrt{H} , \tag{7.42}$$

$$h_{xx} = H - 1 , \tag{7.43}$$

$$K_{xx} = \frac{H'}{2\sqrt{H}} , \tag{7.44}$$

which, in addition to the reference metric in cartesian coordinates ($\hat{\gamma}_{xx} = \hat{\gamma}_{yy} = \hat{\gamma}_{zz} = 1$), represent the only non-zero quantities at $t = 0$. The system is then evolved choosing the "harmonic" gauge [97], where the lapse function is evolved according to:

$$\partial_t \alpha = -\alpha^2 K , \tag{7.45}$$

while the shift is not evolved in time, i.e. $\partial_t \beta^i = 0$.

Results of the test are shown in Fig. 7.1; the numerical setup consists of a unigrid employing 100 points on each direction, with boundaries [-0.5,0.5], where a displacement dx = 0.01 is used and a CFL factor of 0.45 is employed. The parameters of the wave are set to be $A = 0.01$ and $d = 1.0$. The BSSN version of the test is compared with the fCCZ4 one, for which, in turn, 4 cases are investigated: the undamped formulation and the damped one with the damping parameter $k_1 = 1.0, 2.0$ and 5.0 (k_2 is set to zero in every case).

The results illustrated here are in agreement with literature (see, e.g., Ref. [104]); the BSSN formulation does not allow for any long term evolution of the system, leading instead to early divergences, which are overcome with the fCCZ4 formulation. In this case, while the undamped formulation still leads to an overall divergence of the system, the employment of a damping coefficient $k_1 = 1.0$ leads to a stable evolution; increasing the damping coefficients leads to larger and larger oscillations which result in overdamping when $k_1 > 5.0$, resulting again in an early divergence of the system.

7.3.2 Robust stability testbed

The Robust Stability testbed [253] consists in the evolution of initial data consisting in turn of random numbers with a very small amplitude ($\epsilon \in [-10^{-10}, 10^{-10}]$) , which are applied as a perturbation at each grid point to every code variable requiring initialization. Such a test is very important, since it can reveal exponentially growing modes which whould otherwise be masked by a strong initial signal for a considerable amount of time. The numerical setup consists of a cartesian unigrid with 50 points for all directions, boundaries [-0.5,0.5], a displacement dx = 0.02 and a CFL factor equal to 0.45. The test is again carried out using both the BSSN and the fCCZ4 formulations, with 1+log and Gamma-driving conditions for the lapse factor and the shift vector; for fCCZ4, in particular, the two damping parameters k_1 and k_2 are set to zero, as done, e.g., in Ref. [254].

Fig. 7.2 shows the results of this test: both formulations lead to a stable evolution for the

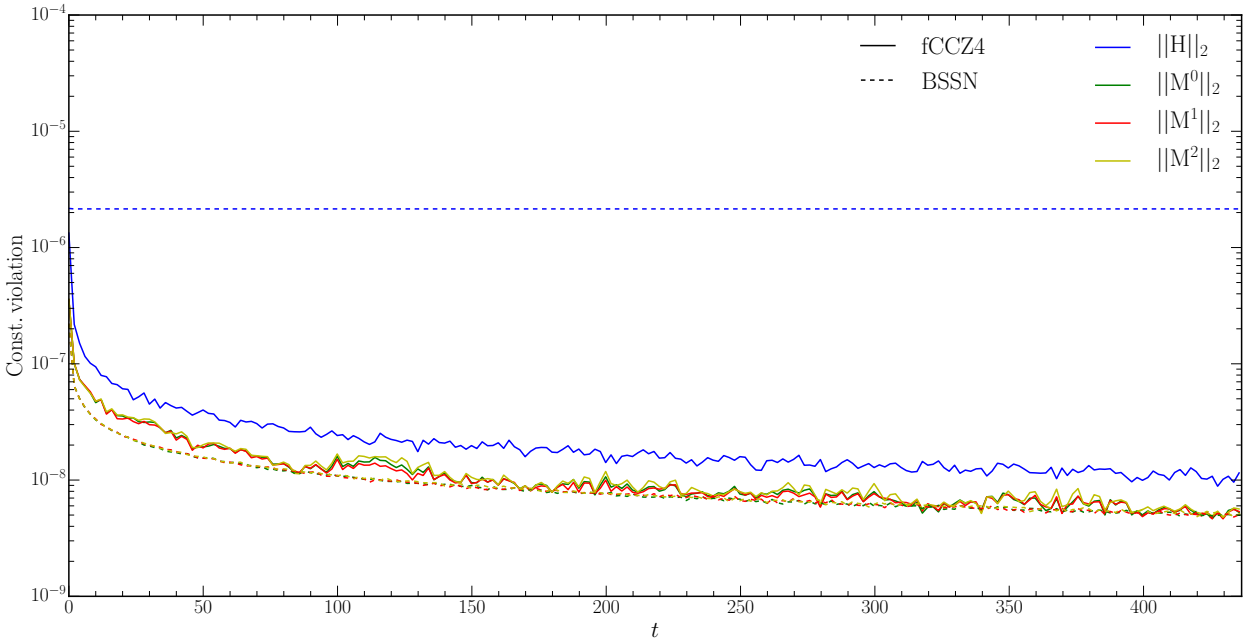

Figure 7.2 L2-norm of the constraint violations with respect to time for the robust stability test evolved in the BSSN (dashed curves) and undamped fCCZ4 (solid curves) formulations.

time interval investigated here. Interestingly, the momentum constraint violations decrease below 10^{-8} in both cases, with fCCZ4 showing a stronger oscillatory behavior. The same behavior is seen for the Hamiltonian constraint violation; however, for this variable, BSSN leads to a constraint violation which, at the end of the illustrated time window, is two orders of magnitude higher than fCCZ4.

7.3.3 Head-On black hole collision

The final study presented here consists in the evolution of two black hole punctures set up according to the Brill-Lindquist prescription [255, 256]. The initial data are conformally flat, hence $h_{ij} = 0$ and $\tilde{\Lambda}^i$ for every coordinate system; also, since, $K_{ij} = 0$, the only non-gauge variable which is not identically zero everywhere is the conformal factor. For the Brill-Lindquist initial data, the latter is given by

$$\psi = e^{\phi} = 1 + \sum_{i=1}^{N} \frac{m_i}{2|\boldsymbol{r}_i - \boldsymbol{r}|}\,, \tag{7.46}$$

where m_i and $\boldsymbol{r}_i$ respectively represent the mass and the location of the i-th puncture. Finally, the initial lapse and shift are set to $\alpha = \psi^{-2}$ and $\beta^i = B^i = 0$, as done in the public NRPy+ code tutorial [257].

The test aims to evolve the initial data in the fCCZ4 formulation up to the merger of the two black holes, comparing with both the BSSN formulation implemented in the same code, and the NRPy+ code (which also adopts BSSN). The black holes studied here have $m_1 = m_2 = 0.5$ and are initially placed at $x_1 = y_1 = x_2 = y_2 = 0$ and $z_1 = 0.5$, $z_2 = -0.5$; in this way, the head-on collision happens along the z-axis and the azimuthal simmetry of the system can thus be exploited. The numerical setup consists of a sinhspherical unigrid with $n_r = 50, n_\theta = 20$ and $n_\phi = 6$, which, together with a CFL factor of 0.45, implies a $dt = 0.000187$; various choices for the damping parameter k_1, namely 1.0 and 3.0, are implemented, with k_2 being fixed to 0. While inner ghost zones are set according to the prescriptions detailed in Sec. 7.1.2, outer ghost zones are filled, following Ref. [247] by using a quadratic extrapolation:

$$\psi(r) \approx 3\psi(r - \delta r) - 3\psi(r - 2\delta r) + 3\psi(r - 3\delta r)\,. \tag{7.47}$$

Performance of the test is monitored by evaluating the L2-norm of the Hamiltonian constraint in time and carrying out comparisons of different variables with respect to the same ones evaluated by NRPy+ (in this regard, the instant of merging $t = t_{mer}$ is considered). The evolution is carried out for 38700 iterations ca. (up to the time of the merger), corresponding to a final time $t \approx 7.23$.

Fig. 7.3 shows the evolution of the L2-norm of the Hamiltonian constraint violation over time for both BSSN and fCCZ4 (with $k_1 = 1.0, 3.0$). In both cases, during the entire evolution, the violation is dominated by the high (generally greater than one) values in correspondence of the two punctures; the damping effect however is evident for the fCCZ4 formulation. Indeed, while BSSN leads to increasingly high violations starting from $t = 5$, fCCZ4 does not feature such effect; the damping effect, easily recognizable from the

oscillations of the L2-norm, leads to a merger with a lower constraint violation, which is also not evidently increasing at the end of the simulation. Interestingly, no effect can be seen here when selecting different values of k_1.

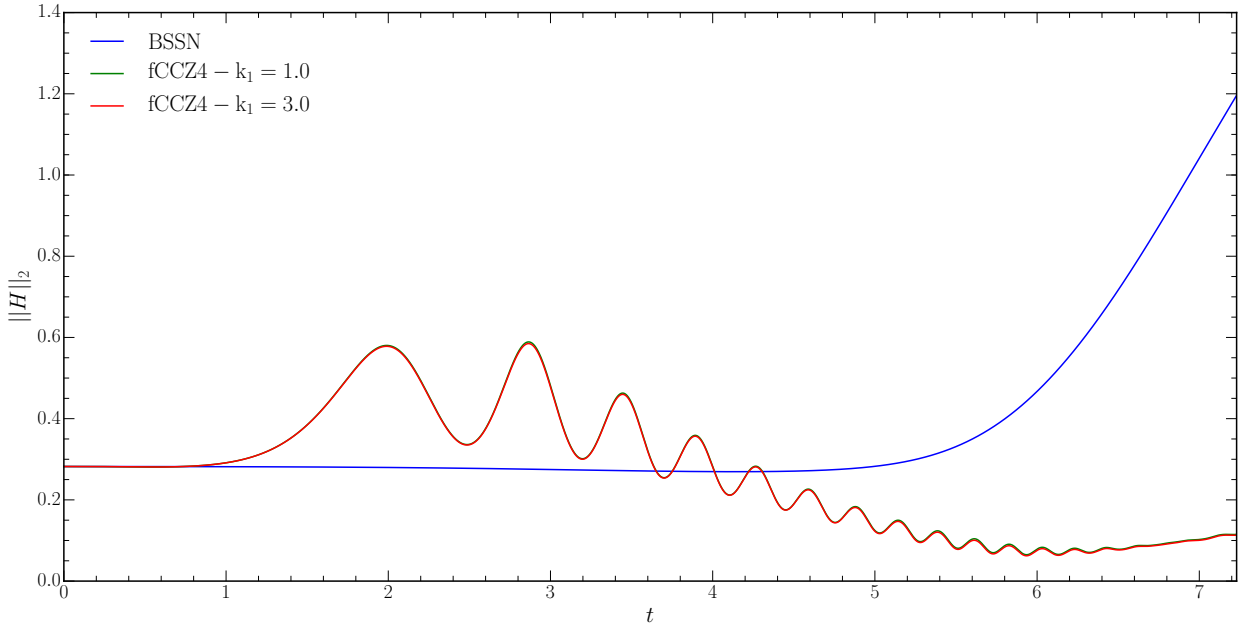

Figure 7.3 L2-norm of the Hamiltonian constraint violation with respect to time for the Brill-Lindquist initial data evolved in the BSSN and damped fCCZ4 (with different values of the damping parameter k_1) formulations.

The investigation of the instant of the merger deserves more attention, since it can be used as a tracker for different behaviors for the variables when using different formulations. As a first comparison, the Hamiltonian constraint violation as a function of r is compared in Fig. 7.4 for BSSN and fCCZ4; also, the same initial data are evolved with the BSSN formulation implemented in the NRPy+ code, and results are included in the same figure.

As expected, and as evident by looking at the BSSN and NRPy+ curves, the maximum violation is reached, when no constraint damping is applied, in correspondence of the merged object at $r = 0$; the two curves do not show the exact same profile since it was not possible to set the exact same grid used in the solver also in NRPy+. As expected, fCCZ4 allows for the constraint violation to propagate in the numerical grid, and this leads to the absence of the peak at $r = 0$, which is now spread in the region nearby, with consequences which will

be illustrated later. In general, however, the constraint violation is few orders of magnitude lower than BSSN and the reduction is even more evident when comparing with NRPy+; no visible differences are found when using different values k_1 values.

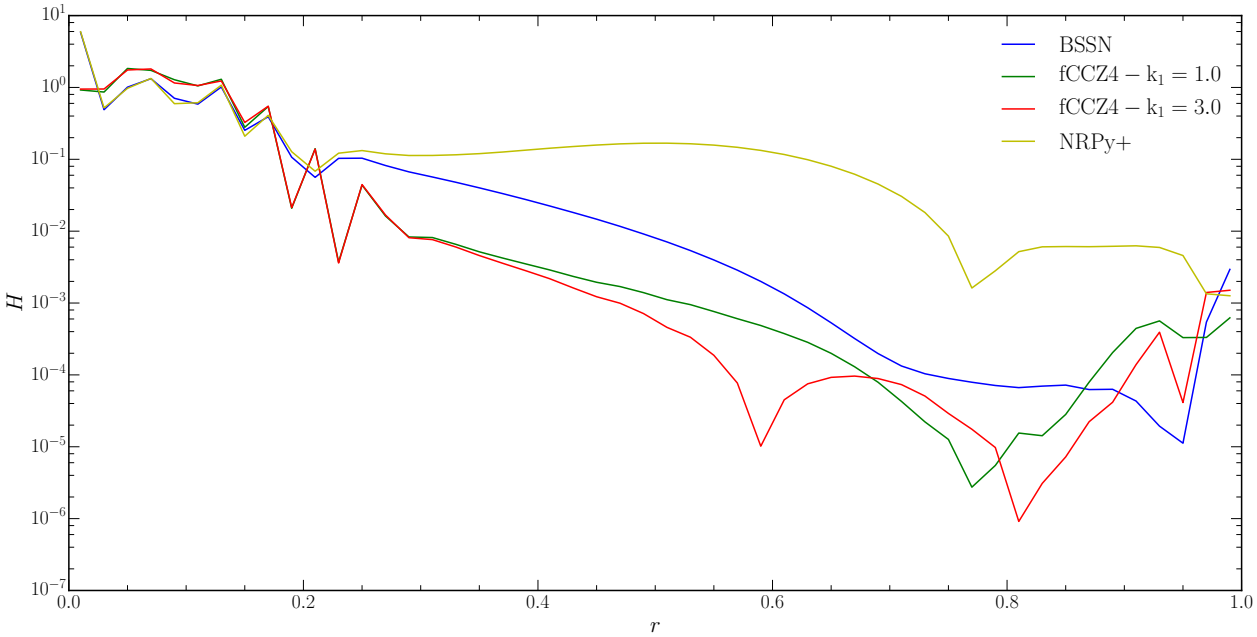

Figure 7.4 Hamiltonian constraint violation as a function of radius for the Brill-Lindquist initial data evolved in the BSSN and damped fCCZ4 formulations. Results obtained with the NRPy+ code are also included for comparison.

Fig. 7.5 shows the profiles, evaluated at $t = t_{mer}$, of the conformal factor and the lapse function vs. the spherical radius r for all the runs also considered in Fig. 7.4; fractional differences with respect to the profiles determined using NRPY+ are illustrated in the lower panels of the same figure. The profiles almost overlap at every r, with maximal differences (of about 10% reached in the region $r < 0.2$, where the constraint violations are higher. Interestingly, the adoption of a $k_1 = 3.0$ alters the profile of the conformal factor at $r \approx 1.0$, while the use of different k_1 doesn't lead to significant differences in the same area for the lapse function. Not only good agreement is therefore found with respect to results obtained with NRPy+, but the capability of the code to simulate binary black hole collisions has also been tested.

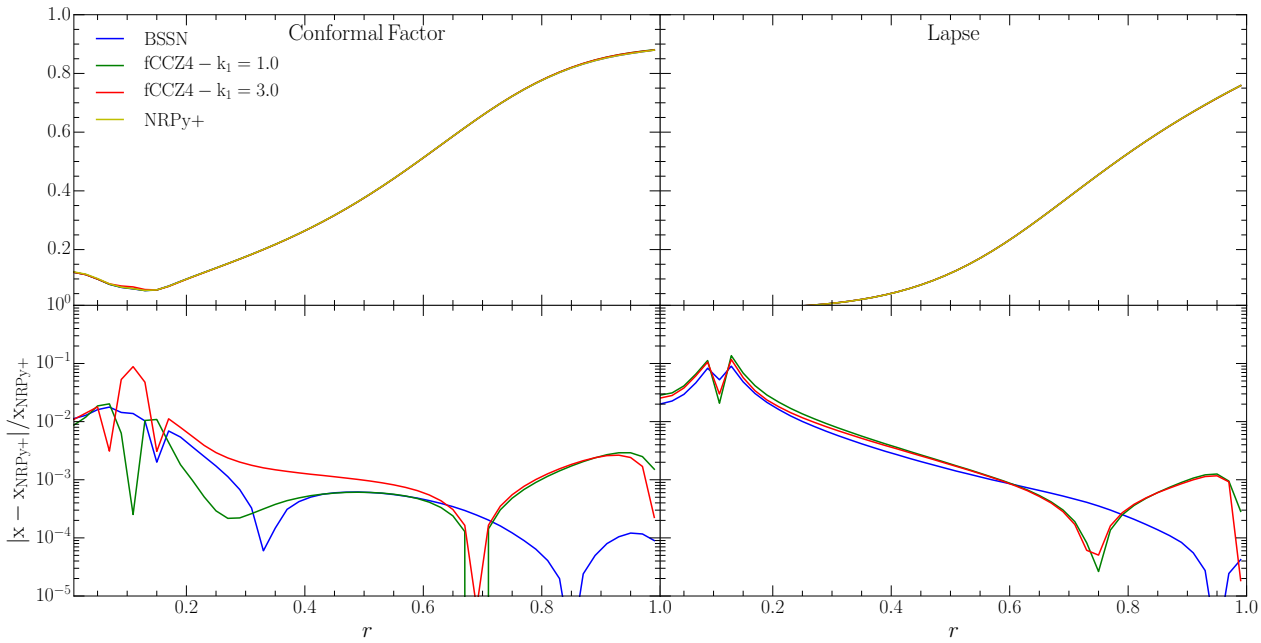

Figure 7.5 Profiles of the conformal factor (left panel) and lapse (right panel) as a function of radius, evaluated at $t = t_{mer}$, for the simulations carried out with the BSSN and fCCZ4 formulations; plots also include the profiles obtained using the NRPy+ code. Fractional differences of the variables with respect to results obtained with NRPy+ are also included in the lower panels.

CHAPTER 8

CONCLUSIONS

The results presented in this thesis work have principally focused on the study and characterization of a new set of microscopic EOSs, whose properties have been mainly investigated in the context of simulations of binary neutron star mergers. The latter set has been first derived within the Brueckner-Hartree-Fock framework in the assumption of zero-temperature and it has been shown to fulfill a number of constraints imposed by both nuclear physics and astrophysics. In the first study presented in this thesis work, neutron star related (global) properties have been investigated for these microscopic EOSs and comparisons have been carried out with respect to widely used phenomenological EOSs; in particular, a number of universal relations has been confirmed and extended for these EOSs, with a particular focus on the so-called "I-Love-Q" relations.

The study, which also included versions of the EOSs accounting for the presence of hyperons and quarks, not only confirmed the validity of several universal relations, but also demonstrated that the microscopic EOSs are fully compatible with the constraints imposed by interpretation of the first observed neutron-star merger event GW170817, respecting in particular the lower $2M_{\odot}$ limit of the NS maximum mass and featuring typical radii between 12 and 13 km, constrained by the related values of the tidal deformability Λ. As a side

result, this study has allowed the determination of both tabulated and piecewise polytropic versions of the EOSs compatible with Numerical Relativity codes.

The zero-temperature versions of the EOSs have been implemented in the `WhiskyTHC` code in order to perform BNS merger simulations in the hybrid EOS approach. These first simulations, although using an approximate, but widely used, description of finite temperature effects, have led to a first study of both the hydrodynamic and gravitational wave signal properties. At the same time, the aforementioned EOSs have been extended to finite temperature, using the BHF approach for asymmetric nuclear matter at finite temperature. The study, whose results have been presented in this thesis work, has led to the production of four publicly available finite-temperature microscopic EOSs released in a format compatible with numerical codes. These new EOSs are characterized by important features which differentiate them with respect to other widely used finite-temperature EOSs, such as the non systematic increase of the gravitational mass with temperature and the generally lower values of the thermal adiabatic index for beta-stable matter for a wide range of temperatures. Of course, it is also important to remark the importance of this new sample of EOSs, since publicly available and constraint-fulfilling EOSs are very few and, as a consequence, systematic studies of NS properties for a wide range of finite temperature EOSs are still not feasible.

This study not only has allowed to accurately perform merger simulations using a realistic treatment for temperature, but has also allowed to make precise comparisons between simulations carried out with the hybrid EOS and the finite temperature approaches. Indeed, the hybrid EOS approach forces matter to unrealistically mantain beta-equilibrium even during and after the merger event, and also doesn't allow to implement neutrino treatments; comparisons with simulations with a complete temperature treatment made it possible to both understand the impact and quantify the deviation from beta-stability and neutrino effects. The study, which also featured the comparison with a widely employed EOS, the phenomenological SFHo, has led to an important result: the direct measurement of the $\Gamma_{\rm th}$

parameter from simulations. It has been indeed possible to evaluate $\Gamma_{\rm th}(\rho, x_p, T)$ directly on the numerical grid and considering different methods and, for the first time, the evolution in time of the variable distribution has been discussed.

Simulations with the complete sample of finite temperature EOSs have also been carried out, and a systematic investigation of the merger properties has been performed, focusing in particular on the remnant properties and the dynamical ejecta. It will be interesting, as future extensions of this work, to both increase the sample of simulations discussed here by comparing with phenomenological EOSs and investigating, e.g., the stability of the remnant on the initial masses or the phenomena related to long-lived remnants.

On the other hand, this thesis work has presented a new standalone Numerical Relativity code, which has successfully passed a number of standard tests and has also proven capable to handle basic simulations of binary black hole mergers. The code, characterized by a C++ infrastructure, employs state of the art libraries for tensorial equations and is able to solve both the BSSN and the fCCZ4 formulations of the spacetime equations in arbitrary curvilinear coordinates, in vacuum. While extending the current Einstein equations with source terms is straightforward, in order to perform simulations where also a non-zero stress-energy tensor is present, the solution of the relativistic hydrodynamics equations is a more difficult task. A realistic possibility, which also represents a future development of this work, is related to linking the code presented here to an already existing framework for the relativistic hydrodynamics able to handle different coordinate systems, such as the BHAC code [258, 259].

Appendix A

Results postprocessing

Simulations carried out with `WhiskyTHC` (and, in general, with the Einstein Toolkit framework [260]) feature the production of output while running; such output includes (but it's not limited to) the evaluation of maxima, minima, L2-norms and entire 2D or 3D snapshots of the hydrodynamic and relativistic variables. In some cases, however, the request output (such as variable integrals or time-derivatives) isn't or can't be produced *online* and a further procedure of postprocessing has to be carried out.

As far as the results presented in this thesis work are concerned, the public `PostCactus` framework has been employed; the latter uses a Python infrastructure in order to access 1D, 2D and 3D cuts of the data and allows to both visualize and perform operations with the same cuts.

The extraction of the gravitational-wave signal represents a central point in the context of postprocessing. Indeed, the standard output of a numerical relativity simulation is not the strain itself, but the Newman-Penrose scalar ψ_4, defined according to the standard Newman-Penrose formalism [261]. In particular, ψ_4 is sampled during the simulation at different times and at different surfaces of constant coordinate radius r using the Einstein Toolkit module WeylScal4. One then uses that ψ_4 is related to the second time derivatives of the gravitational-wave polarization amplitudes h_+ and $h_\times$ by

$$\psi_4 = \ddot{h}_+ - i\ddot{h}_\times = \sum_{l=2}^{\infty} \sum_{m=-l}^{l} \psi_4^{lm}(t,r)\, {}_{-2}Y_{lm}(\theta,\phi)\,, \tag{A.1}$$

where the second time derivative is represented by the double dot notation and the multipole expansion of ψ_4 in spin-weighted spherical harmonics [262] of spin weight $s = -2$ (such

decomposition is performed by the module MULTIPOLE) is introduced. As the dominant mode is $l = m = 2$, a common approach restricts the analysis only to the latter; i.e., one assumes

$$h_{+,\times} = \sum_{l=2}^{\infty} \sum_{m=-l}^{l} h^{lm}_{+,\times}(t, r)\, {}_{-2}Y_{lm}(\theta, \phi) \approx h^{22}_{+,\times}\, {}_{-2}Y_{22}(\theta, \phi)\,, \tag{A.2}$$

where, in order to double integrate ψ_4 in time, the fixed-frequency integration described in [263] is carried out. In Ch. 5 and Ch. 6, the waveforms are also aligned, as in [231], according to the "time of the merger", which is set as $t = 0$ and defined as the time when the GW amplitude

$$|h| \equiv \sqrt{h_+^2 + h_\times^2} \tag{A.3}$$

is maximal. Once the GW strain is computed, a number of other related quantities can be also calculated; in this thesis work, in particular, the phase of the complex waveform, labeled as $\chi = \arctan(h_\times/h_+)$, and the instantaneous frequency of the gravitational waves, defined as in [264],

$$f_{\rm GW} \equiv \frac{1}{2\pi} \frac{\mathrm{d}\chi}{\mathrm{d}t}\,. \tag{A.4}$$

is considered and studied; furthermore, as in [231], $f_{\rm max} \equiv f_{\rm GW}(t = 0)$ is identified as the instantaneous frequency at amplitude maximum.

The total emitted energy for the $l = m = 2$ mode can be computed according to

$$E_{\rm GW} = \frac{R^2}{16\pi} \int dt \int d\Omega \left|\dot{h}(t, \theta, \phi)\right|^2, \tag{A.5}$$

where Ω and R respectively represent the solid angle and the source-detector distance.

The power spectral density (PSD) of the effective amplitude is also extensively considered in this work and is defined as

$$\tilde{h}(f) \equiv \sqrt{\frac{\left|\tilde{h}_+(f)\right|^2 + \left|\tilde{h}_\times(f)\right|^2}{2}}\,, \tag{A.6}$$

where $\tilde{h}_{+,\times}(f)$ are the Fourier transforms of $h_{+,\times}$,

$$\tilde{h}_{+,\times}(f) \equiv \int dt e^{-i2\pi f t} h_{+,\times}(t)\,, \tag{A.7}$$

for $f \geq 0$, and $\tilde{h}_{+,\times}(f) \equiv 0$ for $f < 0$.

We determine the position of the f_2 peak of the PSD, after applying a symmetric time-domain Tukey filter with parameter $\alpha = 0.25$ to the waveforms, in order to compute PSDs without the artificial noise due to the truncation of the waveform. We then fit our data with the analytic function [265]

$$S_2(f) = A_{2G} e^{-(f-F_{2G})^2/W_{2G}^2} + A(f)\gamma(f)\,, \tag{A.8}$$

where

$$A(f) \equiv \frac{1}{2W_2}[(A_{2b} - A_{2a})(f - F_2) + W_2(A_{2b} + A_{2a})]\,, \tag{A.9}$$

$$\gamma(f) \equiv \left(1 + e^{-(f-F_2+W_2)/s}\right)^{-1}\left(1 + e^{(f-F_2-W_2)/s}\right)^{-1}. \tag{A.10}$$

The peak frequency is then determined by

$$f_2 \equiv \frac{\int df\, S_2(f)\, f}{\int df\, S_2(f)}\,. \tag{A.11}$$

This fitting procedure manifests an intrinsic uncertainty due to both the choice of the fitting functions and parameters, and the integration interval, which we estimate as $\pm 10\,\mathrm{Hz}$.

Such indetermination is later added in quadrature to a systematic deviation of the value we find for f_2 from the nearest (local) maximum of the PSD curve. In Chapter 5, the latter estimate coincides with the deviation with respect to the global maximum of the PSD for all the cases considered apart from the $\Gamma_{\mathrm{th}} = 1.75$ case, where the presence of a second narrower peak located at lower frequencies determines a higher indetermination. The case $\Gamma_{\mathrm{th}} = 1.7$ also shows the same feature, with the two peaks being indistinguishable with respect to each other.

Appendix B

The microscopic EOS set: methods and formats

The zero-temperature, beta-equilibrated EOSs presented in this thesis work can be employed in numerical codes in their tabulated format, i.e. a simple ASCII file containing columns representing the physical variables (energy density, pressure etc.) sampled in such a way to cover the density range effectively used in the code. In particular, in order for a simulation in the Hybrid EOS approach to be carried out with the `WhiskyTHC` code, the EOS table is first employed in the `LORENE` code, so that the appropriate initial data are generated and later imported in `WhiskyTHC`. The same table is then converted in a format compatible with the `PIZZA` module [266, 267] included in `WhiskyTHC`; the latter, in particular, is devoted to handling the EOS during the simulation itself.

The Einstein Toolkit code doesn't adopt tabulated EOSs for the time evolution; therefore, while the initial data procedure remains the same, a different approach has to be used for the simulation itself. In particular, tests with the latter code have been carried out by obtaining a piecewise polytropic representation of the investigated EOSs. The latter operation is carried out by following the method outlined in Ref. [268]: a Mathematica notebook has been created which solves Eq. (12) of the same Ref. using the `FindMinimum` routine.

The EOS, in the tabulated or piecewise polytropic format, is then complemented by choosing a $\Gamma_{\rm th}$, which is kept constant during the simulation; this is done by carrying out the appropriate selection in the `WhiskyTHC` simulation Parfile.

A different procedure is followed for BNS simulations with finite temperature EOSs; while initial data are still consisting of zero-temperature stars and the `LORENE` procedure is the same as before, a table where the temperature dependence of the parameters is present has to be used for the simulation itself. Moreover, since the simulated model is free to drive-away from beta-equilibrium (as shown, e.g., in Sec. 5.3), the finite-temperature table should also include the electron fraction dependence for all the physical parameters.

The finite-temperature EOSs developed and discussed in this thesis work are first cast in an ASCII format similar to the one used by Shen et al. for the updated version of their EOS [223]; tables in such a format are downloadable from an online repository [219][1]. These tables, however, only account for the baryonic contribution of the NS matter, and leptons have to be added appropriately.

It is possible to cast the EOSs in a format compatible with the `PIZZA` module by first using the public `EOSmaker` code [220]; the latter contains routines that convert EOSs from a Shen-like format to tables in the HDF5 format (which is still not compatible with `PIZZA`). Notably, the procedure also complements the baryonic EOS with a leptonic one; in this regard, the EOS of Timmes et al. [221, 222] is used. Such a so-constructed EOS is finally converted again in a format usable for simulations by using an appropriate set of routines included in `WhiskyTHC`.

[1] Downloadable versions not only include the core part of the EOS, but, for each model, the H. Shen EOS crust [223] is attached for every temperature and electron fraction.

REFERENCES

[1] The LIGO Scientific Collaboration and The Virgo Collaboration (LIGO Scientific Collaboration and Virgo Collaboration), Phys. Rev. Lett. **119**, 161101 (2017).

[2] LIGO Scientific Collaboration, Virgo Collaboration, Gamma-Ray Burst Monitor, INTEGRAL, B. P. Abbott, R. Abbott, T. D. Abbott, F. Acernese, K. Ackley, C. Adams, T. Adams, P. Addesso, R. X. Adhikari, V. B. Adya, and et al. (LIGO Scientific Collaboration and Virgo Collaboration), Astrophys. J. Lett. **848**, L13 (2017).

[3] S. Roy, A. S. Sengupta, and P. Ajith, arXiv e-prints , arXiv:1711.08743 (2017).

[4] A. Buonanno and T. Damour, Phys. Rev. D **59**, 084006 (1999).

[5] D. Alic, W. Kastaun, and L. Rezzolla, Phys. Rev. D **88**, 064049 (2013).

[6] T. Dietrich, S. Bernuzzi, B. Bruegmann, and W. Tichy, ArXiv e-prints (2018).

[7] V. Dexheimer, R. Negreiros, and S. Schramm, Phys. Rev. C **92**, 012801 (2015).

[8] C. A. Raithel, European Physical Journal A **55**, 80 (2019).

[9] A. Endrizzi, R. Ciolfi, B. Giacomazzo, W. Kastaun, and T. Kawamura, Classical and Quantum Gravity **33**, 164001 (2016).

[10] K. Dionysopoulou, D. Alic, and L. Rezzolla, Phys. Rev. D **92**, 084064 (2015).

[11] N. Sanchis-Gual, P. J. Montero, J. A. Font, E. Müller, and T. W. Baumgarte, Phys. Rev. D **89**, 104033 (2014).

[12] V. Mewes, Y. Zlochower, M. Campanelli, I. Ruchlin, Z. B. Etienne, and T. W. Baumgarte, Phys. Rev. D **97**, 084059 (2018).

[13] V. Mewes, Y. Zlochower, M. Campanelli, T. W. Baumgarte, Z. B. Etienne, F. G. L. Armengol, and F. Cipolletta, Phys. Rev. D **101**, 104007 (2020).

[14] P. Tsatsin and P. Marronetti, Phys. Rev. D **88**, 064060 (2013).

[15] T. Dietrich, N. Moldenhauer, N. K. Johnson-McDaniel, S. Bernuzzi, C. M. Markakis, B. Brügmann, and W. Tichy, Phys. Rev. D **92**, 124007 (2015).

[16] S. Banik, M. Hempel, and D. Bandyopadhyay, Astrohys. J. Suppl. **214**, 22 (2014).

[17] S. Typel, G. Röpke, T. Klähn, D. Blaschke, and H. H. Wolter, Phys. Rev. C **81**, 015803 (2010).

[18] A. W. Steiner, M. Hempel, and T. Fischer, Astrophys. J. **774**, 17 (2013).

[19] M. Hempel, T. Fischer, J. Schaffner-Bielich, and M. Liebendörfer, Astrophys. J. **748**, 70 (2012).

[20] H. Togashi, E. Hiyama, Y. Yamamoto, and M. Takano, Phys. Rev. **C93**, 035808 (2016).

[21] J.-J. Lu, Z.-H. Li, G. F. Burgio, A. Figura, and H. J. Schulze, Physical Review C **100**, 054335 (2019).

[22] Most, Elias R., Jens Papenfort, L., Dexheimer, Veronica, Hanauske, Matthias, Stoecker, Horst, and Rezzolla, Luciano, Eur. Phys. J. A **56**, 59 (2020).

[23] J.-B. Wei, A. Figura, G. F. Burgio, H. Chen, and H.-J. Schulze, Journal of Physics G Nuclear Physics **46**, 034001 (2019).

[24] A. Figura, J.-J. Lu, G. F. Burgio, Z.-H. Li, and H.-J. Schulze, Phys. Rev. D **102**, 043006 (2020).

[25] W. Baade and F. Zwicky, Proceedings of the National Academy of Sciences **20**, 259 (1934).

[26] N. Chamel and P. Haensel, Living Reviews in Relativity **11**, 10 (2008).

[27] S. Woosley and T. Janka, Nature Physics **1**, 147 (2005).

[28] J. M. Lattimer and M. Prakash, Science **304**, 536 (2004).

[29] F. Özel and P. Freire, Annual Review of Astronomy and Astrophysics **54**, 401 (2016).

[30] P. B. Demorest, T. Pennucci, S. M. Ransom, M. S. E. Roberts, and J. W. T. Hessels, Nature **467**, 1081 (2010).

[31] J. Antoniadis, P. C. C. Freire, N. Wex, T. M. Tauris, R. S. Lynch, and et al., Science **340**, 448 (2013).

[32] H. T. Cromartie, E. Fonseca, S. M. Ransom, P. B. Demorest, Z. Arzoumanian, H. Blumer, P. R. Brook, M. E. DeCesar, T. Dolch, J. A. Ellis, R. D. Ferdman, E. C. Ferrara, N. Garver-Daniels, P. A. Gentile, M. L. Jones, M. T. Lam, D. R. Lorimer, R. S. Lynch, M. A. McLaughlin, C. Ng, D. J. Nice, T. T. Pennucci, R. Spiewak, I. H. Stairs, K. Stovall, J. K. Swiggum, and W. W. Zhu, Nature Astronomy **4**, 72 (2020).

[33] R. C. Duncan and C. Thompson, Astrophys. J. **392**, L9 (1992).

[34] A. Hewish, S. J. Bell, J. D. H. Pilkington, P. F. Scott, and R. A. Collins, Nature **217**, 709 (1968).

[35] R. Hulse and J. Taylor, Astrophys. J. **195**, L51 (1975).

[36] L. Baiotti and L. Rezzolla, Rept. Prog. Phys. **80**, 096901 (2017).

[37] B. Kiziltan, A. Kottas, M. De Yoreo, and S. E. Thorsett, Astrophys. J. **778**, 66 (2013).

[38] J. H. Taylor and J. M. Weisberg, Astrophys. J. **253**, 908 (1982).

[39] B. P. Abbott, R. Abbott, T. D. Abbott, S. Abraham, F. Acernese, K. Ackley, C. Adams, R. X. Adhikari, V. B. Adya, C. Affeldt, and et al., Astrophys. J. Lett. **892**, L3 (2020).

[40] B. P. Abbott *et al.* (LIGO Scientific Collaboration and Virgo Collaboration), Astrophys. J. Lett. **848**, L13 (2017).

[41] B. D. Metzger, Living Reviews in Relativity **23**, 1 (2019).

[42] G. Fiorella Burgio and A. F. Fantina, "Nuclear Equation of State for Compact Stars and Supernovae," in *Astrophysics and Space Science Library*, Astrophysics and Space Science Library, Vol. 457, edited by L. Rezzolla, P. Pizzochero, D. I. Jones, N. Rea, and I. Vidaña (2018) p. 255.

[43] M. Oertel, M. Hempel, T. Klähn, and S. Typel, Reviews of Modern Physics **89**, 015007 (2017).

[44] R. N. Wolf, D. Beck, K. Blaum, C. Böhm, C. Borgmann, M. Breitenfeldt, N. Chamel, S. Goriely, F. Herfurth, M. Kowalska, S. Kreim, D. Lunney, V. Manea, E. Minaya Ramirez, S. Naimi, D. Neidherr, M. Rosenbusch, L. Schweikhard, J. Stanja, F. Wienholtz, and K. Zuber, Phys. Rev. Lett. **110**, 041101 (2013).

[45] A. F. Fantina, N. Chamel, J. M. Pearson, and S. Goriely, Nuovo Cimento C Geophysics Space Physics C **39**, 400 (2017).

[46] D. Page and S. Reddy, arXiv e-prints , arXiv:1201.5602 (2012).

[47] N. Martin and M. Urban, Physical Review C **94**, 065801 (2016).

[48] N. Chamel, Nuclear Physics A **747**, 109 (2005).

[49] D. G. Ravenhall, C. J. Pethick, and J. R. Wilson, Phys. Rev. Lett. **50**, 2066 (1983).

[50] M. Hashimoto, H. Seki, and M. Yamada, Progress of Theoretical Physics **71**, 320 (1984).

[51] A. S. Schneider, M. E. Caplan, D. K. Berry, and C. J. Horowitz, Phys. Rev. C **98**, 055801 (2018).

[52] D. G. Yakovlev, Mon. Not. R. Astron. Soc. **453**, 581 (2015).

[53] P. F. Bedaque and S. Reddy, Physics Letters B **735**, 340 (2014).

[54] B. Haskell and A. Melatos, International Journal of Modern Physics D **24**, 1530008 (2015).

[55] N. Andersson and G. L. Comer, Mon. Not. R. Astron. Soc. **328**, 1129 (2001).

[56] D. N. Kobyakov and C. J. Pethick, Astrophys. J. **836**, 203 (2017).

[57] I. Vidaña, European Physical Journal Plus **133**, 445 (2018).

[58] L. Rezzolla, P. Pizzochero, I. D. Jones, N. Rea, and I. Vidaña, eds., *The Physics and Astrophysics of Neutron Stars*, Astrophysics and Space Science Library, Vol. 457 (2018).

[59] M. Baldo, G. F. Burgio, and H. Schulze, Phys. Rev. C **61**, 055801 (2000).

[60] J. L. Zdunik and P. Haensel, Astron. Astrophys. **551**, A61 (2013).

[61] M. Baldo, G. F. Burgio, and H.-J. Schulze, in *NATO Advanced Research Workshop on Superdense QCD Matter and Compact Stars* (2003) pp. 113–134, arXiv:astro-ph/0312446 .

[62] E. Annala, T. Gorda, A. Kurkela, J. Nättilä, and A. Vuorinen, Nature Physics **16** (2020), 10.1038/s41567-020-0914-9.

[63] A. Andronic, P. Braun-Munzinger, K. Redlich, and J. Stachel, Nature **561**, 321 (2018).

[64] N. Brambilla *et al.*, Eur. Phys. J. C **74**, 2981 (2014).

[65] K. C. Gendreau, Z. Arzoumanian, and T. Okajima, in *Space Telescopes and Instrumentation 2012: Ultraviolet to Gamma Ray*, Vol. 8443, edited by T. Takahashi, S. S. Murray, and J.-W. A. den Herder, International Society for Optics and Photonics (SPIE, 2012) pp. 322 – 329.

[66] M. Baldo, *Nuclear Methods and Nuclear Equation of State (International Review of Nuclear Physics)* (World Scientific Pub Co Inc (November 16, 1999), 1999).

[67] J. M. Lattimer and M. Prakash, Astrophys. J. **550**, 426 (2001).

[68] M. Baldo and G. F. Burgio, Reports on Progress in Physics **75**, 026301 (2012).

[69] J. R. Oppenheimer and G. M. Volkoff, Physical Review **55**, 374 (1939).

[70] P. Haensel, A. Y. Potekhin, and D. G. Yakovlev, *Neutron Stars 1*, 1st ed. (Springer-Verlag, New York, 2007).

[71] W. Greiner and H. Stocker, *The nuclear equation of state - edited by Walter Greiner and Horst Stocker* (Plenum Press New York).

[72] S. Boffi, A. Covello, M. Di Toro, A. Fabrocini, G. Pisent, and S. Rosati, eds., *Theoretical nuclear physics in Italy. Proceedings, 9th Conference on Problems in Theoretical Nuclear Physics, Cortona, Italy, 9 - 12 October 2002* (2003).

[73] A. Akmal, V. R. Pandharipande, and D. G. Ravenhall, Phys. Rev. C **58**, 1804 (1998).

[74] B. t. Haar and R. Malfliet, Physics Reports **149**, 207 (1987).

[75] R. B. Wiringa, Phys. Rev. C **43**, 1585 (1991).

[76] J. M. Lattimer and F. D. Swesty, Nucl. Phys. A **535**, 331 (1991).

[77] H. Shen, H. Toki, K. Oyamatsu, and K. Sumiyoshi, Nuclear Physics A **637**, 435 (1998).

[78] M. Hempel and J. Schaffner-Bielich, Nuclear Physics A **837**, 210 (2010).

[79] A. Emperador, E. Lipparini, and L. Serra, Phys. Rev. B **73**, 235341 (2006).

[80] G. Fiorella Burgio, "Physics and astrophysics of neutron stars," (2018), lectures given for the PhD course in Physics, Department of Physics and Astronomy, Catania.

[81] B. P. Abbott, R. Abbott, T. D. Abbott, M. R. Abernathy, F. Acernese, K. Ackley, C. Adams, T. Adams, P. Addesso, R. X. Adhikari, and et al., Phys. Rev. Lett. **116**, 061102 (2016).

[82] A. Einstein, Sitzungsberichte der Königlich Preussischen Akademie der Wissenschaften (Berlin) **1916**, 688 (1916).

[83] A. Einstein, Sitzungsberichte der Königlich Preussischen Akademie der Wissenschaften (Berlin) **1918**, 154 (1918).

[84] E. E. Flanagan and S. A. Hughes, New J. Phys. **7**, 204 (2005).

[85] B. F. Schutz, *A first course in general relativity* (Cambridge University Press, 1985).

[86] R. d'Inverno, *Introducing Einstein's Relativity* (Oxford University Press, Oxford, 1992).

[87] S. M. Carroll, *Spacetime and geometry / Sean Carroll. San Francisco, CA, USA: Addison Wesley, ISBN 0-8053-8732-3, 2004, XIV + 513 pp.* (2004).

[88] A. Buonanno and T. Damour, Phys. Rev. D **62**, 064015 (2000).

[89] T. Damour and A. Nagar, Phys. Rev. D **79**, 081503 (2009).

[90] S. Akcay, R. Gamba, and S. Bernuzzi, arXiv e-prints , arXiv:2005.05338 (2020).

[91] J. A. Faber and F. A. Rasio, Living Reviews in Relativity **15**, 8 (2012).

[92] L. Rezzolla and O. Zanotti, *Relativistic Hydrodynamics* (Oxford University Press, Oxford, UK, 2013).

[93] R. Arnowitt, S. Deser, and C. W. Misner, in *Gravitation: An introduction to current research*, edited by L. Witten (John Wiley, New York, 1962) pp. 227–265, gr-qc/0405109 .

[94] E. Gourgoulhon, *Lecture Notes in Physics, Berlin Springer Verlag*, Lecture Notes in Physics, Berlin Springer Verlag, Vol. 846 (Springer, 2012).

[95] M. Alcubierre, *Introduction to* $3+1$ *Numerical Relativity* (Oxford University Press, Oxford, UK, 2008).

[96] R. M. Wald, *General relativity* (The University of Chicago Press, Chicago, 1984).

[97] C. Bona, J. Massó, E. Seidel, and J. Stela, Phys. Rev. Lett. **75**, 600 (1995).

[98] M. Alcubierre, B. Brügmann, P. Diener, M. Koppitz, D. Pollney, E. Seidel, and R. Takahashi, Phys. Rev. D **67**, 084023 (2003).

[99] L. E. Kidder, M. A. Scheel, and S. A. Teukolsky, Phys. Rev. D **64**, 064017 (2001).

[100] T. W. Baumgarte and S. L. Shapiro, Phys. Rev. D **59**, 024007 (1999).

[101] M. Shibata and T. Nakamura, Phys. Rev. D **52**, 5428 (1995).

[102] S. Bernuzzi and D. Hilditch, Phys. Rev. D **81**, 084003 (2010).

[103] C. Gundlach, J. M. Martin-Garcia, G. Calabrese, and I. Hinder, Class. Quantum Grav. **22**, 3767 (2005).

[104] D. Alic, C. Bona-Casas, C. Bona, L. Rezzolla, and C. Palenzuela, Phys. Rev. D **85**, 064040 (2012).

[105] F. Banyuls, J. A. Font, J. M. Ibáñez, J. M. Martí, and J. A. Miralles, Astrophys. J. **476**, 221 (1997).

[106] LORENE, Langage Objet pour la RElativité Numérique, www.lorene.obspm.fr.

[107] E. Gourgoulhon, P. Grandclément, K. Taniguchi, J. A. Marck, and S. Bonazzola, Phys. Rev. D **63**, 064029 (2001).

[108] J. W. York, Phys. Rev. Lett. **82**, 1350 (1999).

[109] P. C. Peters, Physical Review **136**, 1224 (1964).

[110] K. Kyutoku, M. Shibata, and K. Taniguchi, Phys. Rev. D **90**, 064006 (2014).

[111] D. R. Lorimer, Living Rev. Relativ. **8** (2008).

[112] C. S. Kochanek, Astrophys. J. **398**, 234 (1992).

[113] L. Bildsten and C. Cutler, Astrophys. J. **400**, 175 (1992).

[114] D. Brown, P. Diener, O. Sarbach, E. Schnetter, and M. Tiglio, Phys. Rev. D **79**, 044023 (2009).

[115] F. Löffler, J. Faber, E. Bentivegna, T. Bode, P. Diener, R. Haas, I. Hinder, B. C. Mundim, C. D. Ott, E. Schnetter, G. Allen, M. Campanelli, and P. Laguna, Class. Quantum Grav. **29**, 115001 (2012).

[116] M. Bezares, C. Palenzuela, and C. Bona, Phys. Rev. D **95**, 124005 (2017).

[117] D. Pollney *et al.*, Phys. Rev. D **76**, 124002 (2007).

[118] D. Radice, L. Rezzolla, and F. Galeazzi, Mon. Not. R. Astron. Soc. L. **437**, L46 (2014).

[119] D. Radice, L. Rezzolla, and F. Galeazzi, Class. Quantum Grav. **31**, 075012 (2014).

[120] D. Radice, L. Rezzolla, and F. Galeazzi, in *Numerical Modeling of Space Plasma Flows ASTRONUM-2014*, Astronomical Society of the Pacific Conference Series, Vol. 498, edited by N. V. Pogorelov, E. Audit, and G. P. Zank (2015) p. 121, arXiv:1502.00551 [gr-qc] .

[121] V. V. Rusanov, J. Comput. Math. Phys. USSR **1**, 267 (1961).

[122] C.-W. Shu and S. Osher, Journal of Computational Physics **83**, 32 (1989).

[123] A. Harten, J. Comput. Phys. **49**, 357 (1983).

[124] B. Einfeldt, SIAM J. Numer. Anal. **25**, 294 (1988).

[125] D. Radice, L. Rezzolla, and T. Kellerman, Class. Quantum Grav. **27**, 235015 (2010).

[126] F. Galeazzi, W. Kastaun, L. Rezzolla, and J. A. Font, Phys. Rev. D **88**, 064009 (2013).

[127] D. Radice, F. Galeazzi, J. Lippuner, L. F. Roberts, C. D. Ott, and L. Rezzolla, Mon. Not. R. Astron. Soc. **460**, 3255 (2016).

[128] D. Radice, A. Perego, K. Hotokezaka, S. A. Fromm, S. Bernuzzi, and L. F. Roberts, Astrophys. J. **869**, 130 (2018).

[129] H. O. Kreiss and J. Oliger, *Methods for the approximate solution of time dependent problems* (GARP publication series No. 10, Geneva, 1973).

[130] E. Schnetter, S. H. Hawley, and I. Hawke, Class. Quantum Grav. **21**, 1465 (2004).

[131] J. P. Jeukenne, A. Lejeune, and C. Mahaux, Physics Reports **25**, 83 (1976).

[132] R. Wiringa, V. Stoks, and R. Schiavilla, Physical Review C **51**, 38 (1995).

[133] M. M. Nagels, T. A. Rijken, and J. J. de Swart, Phys. Rev. D **17**, 768 (1978).

[134] V. G. J. Stoks, R. A. M. Klomp, C. P. F. Terheggen, and J. J. de Swart, Physical Review C **49**, 2950 (1994).

[135] R. Machleidt, K. Holinde, and C. Elster, Physics Reports **149**, 1 (1987).

[136] R. Machleidt, Adv. Nucl. Phys. **19**, 189 (1989).

[137] P. Grangé, A. Lejeune, M. Martzolff, and J.-F. Mathiot, Phys. Rev. C **40**, 1040 (1989).

[138] W. Zuo, A. Lejeune, U. Lombardo, and J. F. Mathiot, Nuclear Physics A **706**, 418 (2002).

[139] B. S. Pudliner, V. R. Pandharipande, J. Carlson, S. C. Pieper, and R. B. Wiringa, Phys. Rev. C **56**, 1720 (1997).

[140] B. K. Sharma, M. Centelles, X. Viñas, M. Baldo, and G. F. Burgio, Astron. Astrophys. **584**, A103 (2015).

[141] H.-J. Schulze, A. Polls, A. Ramos, and I. Vidaña, Phys. Rev. C **73**, 058801 (2006).

[142] H.-J. Schulze and T. Rijken, Phys. Rev. C **84**, 035801 (2011).

[143] Rijken, Th. A. and Schulze, H. -J., Eur. Phys. J. A **52**, 21 (2016).

[144] A. Drago, A. Lavagno, G. Pagliara, and D. Pigato, European Physical Journal A **52**, 40 (2016).

[145] A. Drago and G. Pagliara, Astrophys. J. Lett. **852**, L32 (2018).

[146] G. F. Burgio, A. Drago, G. Pagliara, H.-J. Schulze, and J.-B. Wei, Astrophys. J. **860**, 139 (2018).

[147] M. Buballa, Physics Reports **407**, 205 (2005).

[148] T. Klähn, R. Łastowiecki, and D. Blaschke, Phys. Rev. D **88**, 085001 (2013).

[149] A. Chodos, R. L. Jaffe, K. Johnson, C. B. Thorn, and V. F. Weisskopf, Phys. Rev. D **9**, 3471 (1974).

[150] H. Chen, M. Baldo, G. F. Burgio, and H.-J. Schulze, Phys. Rev. D **84**, 105023 (2011).

[151] H. Chen, G. Burgio, H. J. Schulze, and N. Yasutake, Astron. Astrophys. **551**, A13 (2013).

[152] H. Chen, J.-B. Wei, M. Baldo, G. Burgio, and H.-J. Schulze, Phys. Rev. D **91**, 105002 (2015).

[153] Y. Chen, G. Tóth, and T. I. Gombosi, Journal of Computational Physics **305**, 604 (2016).

[154] J. Wei, H. Chen, and H. Schulze, Chinese Physics C **41** (2017), 10.1088/1674-1137/41/11/115101.

[155] J.-B. Wei, H. Chen, G. F. Burgio, and H.-J. Schulze, Phys. Rev. D **96**, 043008 (2017).

[156] R. Brockmann and R. Machleidt, Phys. Rev. C **42**, 1965 (1990).

[157] G. Q. Li, R. Machleidt, and R. Brockmann, Phys. Rev. C **45**, 2782 (1992).

[158] E. Annala, T. Gorda, A. Kurkela, and A. Vuorinen, Phys. Rev. Lett. **120**, 172703 (2018).

[159] E. R. Most, L. R. Weih, L. Rezzolla, and J. Schaffner-Bielich, Phys. Rev. Lett. **120**, 261103 (2018).

[160] N. Stergioulas and J. L. Friedman, Astrophys. J. **444**, 306 (1995).

[161] J. B. Hartle, Astrophys. J. **150**, 1005 (1967).

[162] É. É. Flanagan and T. Hinderer, Physical Review D **77**, 021502 (2008).

[163] B. P. Abbott, R. Abbott, T. D. Abbott, F. Acernese, K. Ackley, C. Adams, T. Adams, P. Addesso, R. X. Adhikari, V. B. Adya, and et al. (LIGO Scientific Collaboration and Virgo Collaboration), Phys. Rev. Lett. **119**, 161101 (2017).

[164] D. Radice, A. Perego, F. Zappa, and S. Bernuzzi, Astrophys. J. Lett. **852**, L29 (2018).

[165] S. Postnikov, M. Prakash, and J. M. Lattimer, Phys. Rev. D **82**, 024016 (2010).

[166] P. C. Peters and J. Mathews, Physical Review **131**, 435 (1963).

[167] The LIGO Scientific Collaboration, the Virgo Collaboration, B. P. Abbott, R. Abbott, T. D. Abbott, F. Acernese, K. Ackley, C. Adams, T. Adams, P. Addesso, R. X. Adhikari, V. B. Adya, and et al. (LIGO Scientific Collaboration and Virgo Collaboration), Physical Review X **9**, 011001 (2019).

[168] Z.-H. Li and H. J. Schulze, Physical Review C **78**, 028801 (2008).

[169] T. Gross-Boelting, C. Fuchs, and A. Faessler, Nuclear Physics A **648**, 105 (1999).

[170] Feynman, Metropolis, and Teller, Phys. Rev. D **75**, 1561 (1949).

[171] G. Baym, C. Pethick, and P. Sutherland, Astrophys. J. **170**, 299 (1971).

[172] J. W. Negele and D. Vautherin, Nuclear Physics A **207**, 298 (1973).

[173] J. M. Lattimer and B. F. Schutz, Astrophys. J. **629**, 979 (2005).

[174] A. Worley, P. G. Krastev, and B.-A. Li, Astrophys. J. **685**, 390 (2008).

[175] C. Breu and L. Rezzolla, Mon. Not. R. Astron. Soc. **459**, 646 (2016).

[176] J. Lattimer and M. Prakash, The Astrophysical Journal **550** (2000), 10.1086/319702.

[177] A. W. Steiner, J. M. Lattimer, and E. F. Brown, Astrophys. Journ. **722**, 33 (2010).

[178] K. Yagi and N. Yunes, Phys. Rep. **681**, 1 (2017).

[179] K. Yagi and N. Yunes, Phys. Rev. D **88**, 023009 (2013).

[180] S. Chakrabarti, T. Delsate, N. Gürlebeck, and J. Steinhoff, Phys. Rev. Lett. **112**, 201102 (2014).

[181] N. Stergioulas, Living Reviews in Relativity **6**, 3 (2003).

[182] G. Pappas and T. A. Apostolatos, Physical Review Letters **108**, 231104 (2012).

[183] F. Cipolletta, C. Cherubini, S. Filippi, J. A. Rueda, and R. Ruffini, Phys. Rev. D **92**, 023007 (2015).

[184] F. D. Ryan, Phys. Rev. D **52**, 5707 (1995).

[185] R. Geroch, Journal of Mathematical Physics **11**, 1955 (1970).

[186] R. O. Hansen, Journal of Mathematical Physics **15**, 46 (1974).

[187] A. Burrows and J. M. Lattimer, Astrophys. J. **307**, 178 (1986).

[188] H. A. Bethe, Reviews of Modern Physics **62**, 801 (1990).

[189] M. Baldo and L. S. Ferreira, Physical Review C **59**, 682 (1999).

[190] O. E. Nicotra, M. Baldo, G. F. Burgio, and H. J. Schulze, Astron. Astrophys. **451**, 213 (2006).

[191] O. E. Nicotra, M. Baldo, G. F. Burgio, and H. J. Schulze, Phys. Rev. D **74**, 123001 (2006).

[192] G. F. Burgio and H. J. Schulze, Astron. Astrophys. **518**, A17 (2010).

[193] A. Li, X. R. Zhou, G. F. Burgio, and H. J. Schulze, Physical Review C **81**, 025806 (2010).

[194] G. F. Burgio, H. J. Schulze, and A. Li, Physical Review C **83**, 025804 (2011).

[195] C. Bloch and C. De Dominicis, Nuclear Physics **7**, 459 (1958).

[196] A. Lejeune, P. Grangé, M. Martzolff, and J. Cugnon, Nuclear Physics A **453**, 189 (1986).

[197] W. Zuo, Z. H. Li, A. Li, and G. C. Lu, Physical Review C **69**, 064001 (2004).

[198] I. Bombaci and U. Lombardo, Physical Review C **44**, 1892 (1991).

[199] W. Zuo, I. Bombaci, and U. Lombardo, Phys. Rev. C **60**, 024605 (1999).

[200] J. D. Kaplan, C. D. Ott, E. P. O'Connor, K. Kiuchi, L. Roberts, and M. Duez, Astrophys. J. **790**, 19 (2014).

[201] A. Bauswein, H. Janka, and R. Oechslin, Phys. Rev. D **82**, 084043 (2010).

[202] A. Carbone and A. Schwenk, Physical Review C **100**, 025805 (2019).

[203] M. Hanauske, J. Steinheimer, A. Motornenko, V. Vovchenko, L. Bovard, E. R. Most, L. J. Papenfort, S. Schramm, and H. Stöcker, Particles **2**, 44 (2019).

[204] A. Perego, S. Bernuzzi, and D. Radice, Eur. Phys. J. **A55**, 124 (2019).

[205] H.-T. Janka, T. Zwerger, and R. Moenchmeyer, Astronomy and Astrophysics **268**, 360 (1993).

[206] L. Baiotti, B. Giacomazzo, and L. Rezzolla, Phys. Rev. D **78**, 084033 (2008).

[207] K. Hotokezaka, K. Kyutoku, H. Okawa, M. Shibata, and K. Kiuchi, Phys. Rev. D **83**, 124008 (2011).

[208] K. Kiuchi, K. Kyutoku, Y. Sekiguchi, M. Shibata, and T. Wada, Phys. Rev. D **90**, 041502 (2014).

[209] R. De Pietri, A. Feo, F. Maione, and F. Löffler, Phys. Rev. D **93**, 064047 (2016).

[210] M. Hanauske, K. Takami, L. Bovard, L. Rezzolla, J. A. Font, F. Galeazzi, and H. Stöcker, Phys. Rev. D **96**, 043004 (2017).

[211] R. Ciolfi, W. Kastaun, B. Giacomazzo, A. Endrizzi, D. M. Siegel, and R. Perna, Phys. Rev. D **95**, 063016 (2017).

[212] M. Shibata and K. Kiuchi, Phys. Rev. D **95**, 123003 (2017).

[213] D. Radice, A. Perego, S. Bernuzzi, and B. Zhang, Mon. Not. R. Astron. Soc. **481**, 3670 (2018).

[214] M. G. Alford, L. Bovard, M. Hanauske, L. Rezzolla, and K. Schwenzer, Phys. Rev. Lett. **120**, 041101 (2018).

[215] A. Endrizzi, D. Logoteta, B. Giacomazzo, I. Bombaci, W. Kastaun, and R. Ciolfi, Phys. Rev. D **98**, 043015 (2018).

[216] K. Kiuchi, K. Kyutoku, M. Shibata, and K. Taniguchi, Astrophys. J. **876**, L31 (2019).

[217] R. De Pietri, A. Feo, J. A. Font, F. Löffler, M. Pasquali, and N. Stergioulas, Phys. Rev. D **101**, 064052 (2020).

[218] M. Shibata, K. Taniguchi, and K. Uryū, Phys. Rev. D **71**, 084021 (2005).

[219] https://github.com/bhfeos/FTEOS.

[220] E. O'Connor and C. D. Ott, Class. Quantum Grav. **27**, 114103 (2010).

[221] F. Timmes and D. Arnett, Astrophysical Journal, Supplement Series **125**, 277 (1999).

[222] F. X. Timmes and F. D. Swesty, Astrophys. J., Supp. **126**, 501 (2000).

[223] H. Shen, H. Toki, K. Oyamatsu, and K. Sumiyoshi, The Astrophysical Journal Supplement Series **197**, 20 (2011).

[224] M. Hempel and J. Schaffner-Bielich, Nucl. Phys. **A837**, 210 (2010).

[225] G. Colò, N. van Giai, J. Meyer, K. Bennaceur, and P. Bonche, Physical Review C **70**, 024307 (2004).

[226] A. Carbone, Physical Review Research **2**, 023227 (2020).

[227] S. Köppel, L. Bovard, and L. Rezzolla, Astrophys. J. Lett. **872**, L16 (2019).

[228] R. Gill, A. Nathanail, and L. Rezzolla, Astrophys. J. **876**, 139 (2019).

[229] E. R. Most, L. J. Papenfort, V. Dexheimer, M. Hanauske, S. Schramm, H. Stöcker, and L. Rezzolla, Physical Review Letters **122**, 061101 (2019).

[230] E. R. Most, L. J. Papenfort, and L. Rezzolla, Mon. Not. R. Astron. Soc. **490**, 3588 (2019).

[231] L. Rezzolla and K. Takami, Phys. Rev. D **93**, 124051 (2016).

[232] A. Bauswein, H.-T. Janka, K. Hebeler, and A. Schwenk, Phys. Rev. D **86**, 063001 (2012).

[233] K. D. Kokkotas and B. G. Schmidt, Living Rev. Relativ. **2**, 2 (1999).

[234] W. Kastaun and F. Galeazzi, Phys. Rev. D **91**, 064027 (2015).

[235] J.-B. Wei, J.-J. Lu, G. Burgio, Z. Li, and H.-J. Schulze, Eur. Phys. J. A **56**, 63 (2020).

[236] B. P. Abbott, R. Abbott, T. D. Abbott, F. Acernese, K. Ackley, C. Adams, T. Adams, P. Addesso, R. X. Adhikari, V. B. Adya, and et al. (LIGO Scientific Collaboration and Virgo Collaboration), Physical Review Letters **121**, 161101 (2018).

[237] M. C. Miller, F. K. Lamb, A. J. Dittmann, S. Bogdanov, Z. Arzoumanian, K. C. Gendreau, S. Guillot, A. K. Harding, W. C. G. Ho, J. M. Lattimer, R. M. Ludlam, S. Mahmoodifar, S. M. Morsink, P. S. Ray, T. E. Strohmayer, K. S. Wood, T. Enoto,

R. Foster, T. Okajima, G. Prigozhin, and Y. Soong, The Astrophysical Journal **887**, L24 (2019).

[238] T. E. Riley, A. L. Watts, S. Bogdanov, P. S. Ray, R. M. Ludlam, S. Guillot, Z. Arzoumanian, C. L. Baker, A. V. Bilous, D. Chakrabarty, K. C. Gendreau, A. K. Harding, W. C. G. Ho, J. M. Lattimer, S. M. Morsink, and T. E. Strohmayer, Astrophysical Journal, Letters **887**, L21 (2019).

[239] S. Bernuzzi, arXiv e-prints , arXiv:2004.06419 (2020).

[240] L. J. Papenfort, R. Gold, and L. Rezzolla, Phys. Rev. D **98**, 104028 (2018).

[241] S. Bernuzzi, M. Breschi, B. Daszuta, A. Endrizzi, D. Logoteta, V. Nedora, A. Perego, D. Radice, F. Schianchi, F. Zappa, I. Bombaci, and N. Ortiz, Mon. Not. R. Astron. Soc. **497**, 1488 (2020).

[242] L. Bovard, D. Martin, F. Guercilena, A. Arcones, L. Rezzolla, and O. Korobkin, Phys. Rev. D **96**, 124005 (2017).

[243] T. Vincent, F. Foucart, M. D. Duez, R. Haas, L. E. Kidder, H. P. Pfeiffer, and M. A. Scheel, Phys. Rev. D **101**, 044053 (2020).

[244] J. Lippuner and L. F. Roberts, Astrophys. J. **815**, 82 (2015).

[245] B. D. Metzger, Living Reviews in Relativity **20**, 3 (2017).

[246] T. W. Baumgarte, P. J. Montero, I. Cordero-Carrión, and E. Müller, Phys. Rev. D **87**, 044026 (2013).

[247] I. Ruchlin, Z. B. Etienne, and T. W. Baumgarte, Phys. Rev. **D97**, 064036 (2018).

[248] D. J. Brown, Phys. Rev. D **79**, 104029 (2009).

[249] https://github.com/fil-grmhd/TensorTemplates.

[250] J. R. van Meter, J. G. Baker, M. Koppitz, and D.-I. Choi, Phys. Rev. D **73**, 124011 (2006).

[251] E. Schnetter, Class. Quantum Grav. **27**, 167001 (2010).

[252] applesweb, Apples With Apples: Numerical Relativity Comparisons and Tests: `http://www.ApplesWithApples.org`.

[253] B. Szilágyi, R. Gómez, N. T. Bishop, and J. Winicour, Phys. Rev. D **62**, 104006 (2000).

[254] M. Dumbser, F. Guercilena, S. Köppel, L. Rezzolla, and O. Zanotti, Phys. Rev. D **97**, 084053 (2018).

[255] D. R. Brill and R. W. Lindquist, Phys. Rev. **131**, 471 (1963).

[256] S. Brandt and B. Bruegmann, in *8th Marcel Grossmann Meeting on Recent Developments in Theoretical and Experimental General Relativity, Gravitation and Relativistic Field Theories (MG 8)* (1997) pp. 738–740, arXiv:gr-qc/9711015 .

[257] http://astro.phys.wvu.edu/bhathome/.

[258] O. Porth, H. Olivares, Y. Mizuno, Z. Younsi, L. Rezzolla, M. Moscibrodzka, H. Falcke, and M. Kramer, Computational Astrophysics and Cosmology **4**, 1 (2017).

[259] H. Olivares, O. Porth, J. Davelaar, E. R. Most, C. M. Fromm, Y. Mizuno, Z. Younsi, and L. Rezzolla, Astronomy and Astrophysics **629**, A61 (2019).

[260] F. Löffler, J. Faber, E. Bentivegna, T. Bode, P. Diener, R. Haas, I. Hinder, B. C. Mundim, C. D. Ott, E. Schnetter, G. Allen, M. Campanelli, and P. Laguna, Class. Quantum Grav. **29**, 115001 (2012).

[261] E. T. Newman and R. Penrose, J. Math. Phys. **3**, 566 (1962), erratum in J. Math. Phys. 4, 998 (1963).

[262] J. N. Goldberg, A. J. MacFarlane, E. T. Newman, F. Rohrlich, and E. C. G. Sudarshan, J. Math. Phys. **8**, 2155 (1967).

[263] C. Reisswig and D. Pollney, Classical and Quantum Gravity **28**, 195015 (2011).

[264] J. S. Read, L. Baiotti, J. D. E. Creighton, J. L. Friedman, B. Giacomazzo, K. Kyutoku, C. Markakis, L. Rezzolla, M. Shibata, and K. Taniguchi, Phys. Rev. D **88**, 044042 (2013).

[265] K. Takami, L. Rezzolla, and L. Baiotti, Phys. Rev. D **91**, 064001 (2015).

[266] W. Kastaun, Phys. Rev. D **74**, 124024 (2006).

[267] W. Kastaun, *Developing a code for general relativistic hydrodynamics with application to neutron star oscillations.*, Ph.D. thesis, University of Tübingen (2007).

[268] J. S. Read, B. D. Lackey, B. J. Owen, and J. L. Friedman, Phys. Rev. D **79**, 124032 (2009).